# Synthesis and Characterization of One - dimensional Oxide Nanotubes Encapsulated with Platinum Metal Nanoparticles

Von der Naturwissenschaftlichen Fakultät der Gottfried Wilhelm Leibniz Universität Hannover

Zur Erlangung des Grades einer

DOKTORIN DER NATURWISSENSCHAFTEN

Dr. rer. nat.

genehmigte Dissertation

Von

**M.Sc. Catherine Aresipathi**

Geboren am 06.04.1978, in Vijayawada, India

2008

Dem Promotionsausschuß vorgelegt im November 2008

| | |
|---|---|
| Tag des öffentlichen Kolloquiums : | 23. 01. 2009 |
| Gutachter : | Prof. Dr. Juergen Caro |
| | Prof. Dr. Josef - Christian Buhl |

# Synthesis and Characterization of One - dimensional Oxide Nanotubes Encapsulated with Platinum Metal Nanoparticles

A dissertation submitted to the

Institute of Physical Chemistry and Electrochemistry
Leibniz University of Hannover

For the degree of

**Doctor of Science**
(Dr. rer. nat.)

by

**Catherine Aresipathi**

Hannover, November 2008

*With love to my parents*

# Erklärung zur Dissertation

Hierdurch erkläre ich, dass die Dissertation ‚**Synthesis and Characterization of One - dimensional Oxide Nanotubes Encapsulated with Platinum Metal Nanoparticles'** selbstständig verfasst und alle benutzten Hilfsmittel sowie evtl. zur Hilfeleistung herangezogene Institutionen vollständig angegeben wurden.

Die Dissertation wurde nicht schon als Diplom- oder ähnliche Prüfungsarbeit verwendet.

Hannover

(Catherine Aresipathi)

# Acknowledgements

I would like to express my deepest gratitude to **Prof. Dr. Michael Wark** for his valuable guidance, thought provoking suggestions, inspiring reviews and constant encouragement to carry out the present work. I will remain highly indebted to him for his support and timely advice all throughout my work. The guidance and discussions with the head of the Physical Chemistry and Electrochemistry group and my co – supervisor, **Prof. Dr. Juergen Caro** has helped me enlighten myself about many facts in the field of Chemistry. His dynamic thoughts, broad and profound knowledge, patient instructions have given me a great aid in completing this project. I owe my gratitude also to **Prof. Dr. Josef – Christian Buhl** for his acceptance to be a reviewer of this work and for his immediate readiness to be part of the examination committee. His valuable suggestions are highly commendable.

I wish to thank Dr. Armin Feldhoff for his assistance on working with electron microscopy and for his help in various aspects of my research. My special thanks go to Mr. Frank Steinbach who performed measurements on Transmission Electron Microscopy and Dr. Thorsten M. Giesing for his help in Rietveld analysis measurements. I would also like to thank Mr. Marco Lange and Mr. Falk Heinroth for their collaboration in carrying out Thermogravimetric and Inductive coupled plasma spectroscopy analysis. I am thankful to all my colleagues at Institute of Physical Chemistry, University Hannover especially Ms. Inga Bannat, Ms. Katrin Wessels, Ms. Julia Martynczuk, Mr. Roland Marschall, Ms. Britta Seelandt, Ms. Kerstin Janze and Mrs. Yvonne – Uebe – Gabbey for their perpetual contributions that helped me a lot to achieve my goals. Financial help from Deutsche Forschungsgemeinschaft (DFG) and University of Hannover for this research are highly acknowledged.

I am also grateful to my present colleagues at RENA GmbH, Gütenbach, Germany exclusively for their motivation and support. I take this opportunity to thank my friends Mr. Santosh Rao Kanjarkar, Ms. Anna Glyk, Mrs. Jinu John, Mr. Gautam Sagar, Mr. Rejish nath, Mrs. Preeti Matthew Anil, Ms. Garima Jain and my friends in India for their moral support throughout my work.

Above all, I thank Almighty and my family for giving me strength and courage throughout my thesis and during my stay in Germany. My special gratitude to my brother for his encouragement and love.

# Abstract

The present work focuses on the synthesis and characterization of metal oxide nanotubes employing metal salt fibers as templating structures. Metal salt fibers when used as templating structures together with sol – gel technique to coat the fibers with suitable metal alkoxides can lead to the formation of template filled nanotubes which upon subsequent subjection to auto – reduction by heat treatment results in metal filled nanotubes. The objective of thesis lies in embedding platinum metal inside $SiO_2$, $TiO_2$ and $SnO_2$ nanotubes. Hence, templating fibers from two different platinum salts were investigated for synthesis namely $[Pt(NH_3)_4(HCO_3)_2]$ and $[Pt(NH_3)_4][PtCl_4]$, while the latter is popularly termed as Magnus green salt (MGS).

The samples were analyzed using electron microscopy, X - Ray diffractometry (XRD), thermogravimetric analysis technique, Dynamic light scattering spectroscopy, and Inductively coupled plasma emission – Mass spectrometry within the laboratory limitations.

Using fibers from $[Pt(NH_3)_4(HCO_3)_2]$ salt as template, $SiO_2$, $TiO_2$ and $SnO_2$ nanotubes were synthesized in presence of tetraethylorthosilicate (TEOS) as capping agent which gave rise to monodisperse nanotubes with approximately 38 - 40 wt.- % of Pt incorporated inside the tubes. While Pt doped $SiO_2$ nanotubes (Pt – $SiO_2$ NTs) exhibited considerable yield of tubes with diameter in range of 200 – 800 nm and lengths upto 20 µm long, Pt – $SnO_2$ NTs demonstrated short length tubes (2 – 5 µm) with diameter in broad range of 200 – 800 nm. On the other hand, synthesis of Pt – $TiO_2$ NTs under similar reaction conditions failed to produce tubular morphologies and resulted in particles with minute traces of titanium alkoxide that was utilized in the synthesis.

On contrary, templating fibers from $[Pt(NH_3)_4][PtCl_4]$ under optimized synthesis conditions could give rise to monodisperse and high aspect ratios of Pt - $SiO_2$ (600) and Pt - $TiO_2$ NTs (500) with higher incorporation of Pt (around 48 - 51 wt.- %) inside the tubes at lower temperatures (280°C). It is worthy to point out that synthesis of metal filled nanotubes using MGS as templating structures could be performed at lower molar ratios of salt thereby making the synthesis approach a cost effective technique comparatively. The experimental investigation indicates that nanotubes with a diameter range of 300 – 700 nm and lengths upto 60 µm long for Pt – $SiO_2$ NTs and an average diameter of 500 nm with lengths in the wide range of 4 - 15 µm for Pt – $TiO_2$ NTs can be realized from fibers of MGS.

**Keywords**: Oxide Nanotubes, Templating structures, Nanofibers, Magnus salt, Sol-gel Process

# Kurzfassung

Diese Arbeit konzentriert sich auf die Synthese und Charakterisierung von Metalloxid-Nanoröhren durch die Verwendung von Metallsalzfasern als Templatstrukturen. Metallsalzfasern können, wenn sie als Vorlagestrukturen verwendet werden und mittels der Sol - Gel - Technik mit geeigneten Metallalkoxiden beschichtet werden, zur Bildung gefüllter Nanoröhren dienen. Durch Autoreduktion entstehen dann während einer Wärmebehandlung mit Metall gefüllte Nanoröhren. Das Ziel dieser Arbeit ist Platin-Metall in Metalloxide wie $SiO_2$, $TiO_2$, und $SnO_2$ Nanoröhren einzubetten. Daher wurden Templatfasern aus zwei verschiedenen Platinsalzen für die Synthese untersucht, nämlich $[Pt(NH_3)_4(HCO_3)_2]$ und $[Pt(NH_3)_4][PtCl_4]$; letzteres wird auch als Magnus - Salz bezeichnet.

Die Proben wurden mit Elektronenmikroskopie, Röntgenbeugung (XRD), Thermogravimetrischer Analyse, Dynamischer Lichtstreuspektroskopie und Induktiv gekoppelter Plasmaemmisionen Massenspektroskopie untersucht.

Mit Fasern aus $[Pt(NH_3)_4(HCO_3)_2]$ als Vorlage und in Anwesenheit von Tetraethylorthosilicat (TEOS) als Additiv wurden $SiO_2$, $TiO_2$, und $SnO_2$ Nanoröhren hergestellt. Die erzielten monodispersive Nanoröhren enthielten ungefähr 38 - 40 Gewichtsprozent in den Röhren eingebautes Pt. Pt - $SiO_2$ Nanoröhren erreichten beachtliche Ausbeuten an Röhren mit Durchmessern im Bereich von 200 - 800 nm und Längen bis zu 20 µm, Pt - $SnO_2$ Nanoröhren zeigten kurze Rohrlängen (2 - 5 µm) mit Durchmessern im Bereich von 200 - 800 nm. Auf der anderen Seite konnten im Pt - $TiO_2$ - System unter ähnlichen Reaktionsbedingungen keine röhrenförmigen Morphologien erzeugt werden, man erhielt nur unstrukturierte Partikel mit geringen Spuren von Titanalkoxid welches bei der Synthese verwendet wurde.

Im Gegensatz dazu führten Templatfasern aus $[Pt(NH_3)_4][PtCl_4]$ unter optimierten Synthesebedingungen zu monodispersiven Röhren mit einem hohen Längenverhältnis von 600 bei Pt - $SiO_2$ und 500 bei Pt - $TiO_2$ und höherem Pt Einbau in die Röhren bei niedrigeren Temperaturen (280 °C). Es ist erwähnenswert, dass die Synthese mit Magnus Salz als Vorlage bei kleineren molaren Mengen des Salzes durchgeführt werden konnte und damit eine vergleichsweise kostengünstige Methode darstellt. Die experimentellen Untersuchungen zeigen, dass Nanoröhren mit Durchmessen von 300 - 700 nm und Längen von bis zu 60 µm für Pt - $SiO_2$ und ein mittlerer Durchmesser von 500 nm mit Längen im Bereich von 4 - 15 µm für Pt - $TiO_2$ aus Fasern aus Magnus Salz hergestellt werden können.

**Stichwörter**: Oxide-Nanoröhren, Templat, Nanofasern, Magnus salz, Sol – gel Prozess

# Table of Contents

# 1

# 1. Introduction

## 1.1 Introduction

Nanotechnology is a new wave of science that has gained paramount importance in the last few decades because of its enormous scope of application in diverse fields. The Greek word 'nano' means one billionth part ($10^{-9}$) of a whole. The underlying theme of nanotechnology deals with comprehending, fabricating and manipulating materials with structural features in between those of atoms and bulk materials at the nanometer length scale. In recent years, nanotechnology rendered remarkable innovations particularly in the fields of electronics [1], catalysis [2, 3], and biotechnology [4, 5].

The incorporation of metals into a germanium based nanotube led to the formation of metallic, semiconductor and *n* or *p* types of nanotubes which opened new possibilities in designing miniature devices for electronics industry [6]. Also, mass storage devices prefer nanoscale materials like nanotubes, nanowires and nanodots which could be used as components. A recent investigation shows that devices containing silicon nanocrystallites replaced the conventional flash memories in non – volatile memory devices which are used for data storage and data transfer [7]. Nanosize metal particles occupy a core place in heterogeneous catalysis. The immobilization of ruthenium nanoparticles in the framework of porous carbon led to the formation of high efficiency catalyst that displayed high catalytic activity and stability in the hydrogenation of benzene [8]. Furthermore, biological proteins and peptides which have the intrinsic ability to self – assemble into elongated solid nanofibrils also inspired applications from tissue engineering to nanoelectronics. The diphenylalanine peptide (motif of β - amyloid polypeptide) which exhibits significant thermal and chemical stability is presently progressing towards its application in conventional microelectronic processes and fabrication into functional nanotechnological devices [9].

The properties of materials at nanoscale differ to bulk materials basically for the following two principal reasons.

(i) Increased relative surface area: As the size of the particle decreases, a greater proportion of atoms constitute the surface rather than the inner radius. This makes nanomaterials possess relatively larger surface area per unit mass. As the growth and catalytic chemical reactions take place at the surface, materials in nanoparticulate form will be much more reactive than the same mass of material in larger scale.

(ii) Intrinsic size effects: In crystalline solids, grain boundaries impede the propagation of defects when the material is stressed, giving it strength. When the grains are of nanoscale in size, the interface area within the material extensively increases thereby enhancing its strength and consequently affecting the mechanical and electrical characteristic of the material.

Suitable control of properties of nanometer scale structures together with the concept of miniaturization is paving way to new science as well as novel devices and technologies. The development of nanoscale devices have started to emerge as a fundamental requirement to realize the objectives of nanotechnology. The nanoscale devices not only operate faster with more precision but also utilize energy more efficiently than devices made of bulk materials [10]. Apart from the semiconductor industries, the field of biotechnology is also emphasizing the nanoscale devices for a wide area of applications eminently in DNA sequencing and biosensing [11, 12].

Nanostructures or nanomaterials can be termed as single – phase or multiphase polycrystals with a typical crystal size less than 100 nm in atleast one dimension [13]. Based on their dimensions, nanomaterials can be categorized into nanoparticles, layered or lamellar structures, filamentary structures (nanotubes and nanowires) and bulk nanostructured materials [14].

### 1.2 Nanotubes

Nanotubes can be defined as hollow tube - like or cylindrical objects made of particles with diameter in the nanometer regime. These nanostructures of tubular morphology provoked great interest because of their large surface area and tube – like structure which may supply

sufficiently reactive points for the reaction. These one dimensional nanotubes have distinctive properties and wide variety of applications in catalysis [15, 16], sensors [17 - 19], gas storage materials [20] and in nanoscale electronic and optical devices such as transistors, light emitting devices [21] and lasers [22]. The dimension and the size distribution of the nanotubes play the key parameters in tailoring the properties for these applications.

Nanotubes can be classified into three classes based on their structure and composition [10].

(1) Carbon nanotubes
(2) Biological peptide based nanotubes
(3) Inorganic nanotubes

Extensive research has been invigorated on the synthesis, properties and applications of nanotubes eversince the discovery of carbon nanotubes by S. Iijima [23]. Regardless of the fact that carbon nanotubes are identical to a sheet of graphite, their properties alter from metallic to semiconductor depending on the direction in which the sheet is rolled to form the nanotube. Moreover, carbon nanotubes exhibit superior tensile strength and heat conductivity to that of a graphite sheet [24]. These distinct and advantageous properties of carbon nanotubes aroused enormous interest in investigating its applications and various synthesis methods. Carbon nanotubes find its useful applications in energy storage and energy conversion devices, sensors, field emission displays and radiation sources, hydrogen storage media and nanometer - sized semiconductor devices, probes, and interconnects [25].

Bio - molecules such as proteins, carbohydrates, and cyclic peptides have the ability to self-assemble to form nanotube – like structures. This characteristic feature has enabled researchers to obtain molecular level manipulation of nanomaterials for molecular electronics applications [26] and in selective binding for drug delivery applications [27]. In addition, peptide and protein based nanotubes are biologically harmonic and can be synthesized over simple lab scale equipment. However, their poor temperature stability and sensitivity of their structural integrity to solution conditions restrict them to limited applications.

Carbon nanotubes and Biological peptide based nanotubes are not the subject of this thesis, hence, only inorganic nanotubes are elucidated in detail.

### 1.2.1 Inorganic nanotubes

The stability of the cylindrical form of nanostructures is not limited to carbon nanotubes. Similar to graphite, solid materials such as metal dichalcogenides, $MX_2$ (M = Mo, W; X = S, Se) feature a layered structure wherein the atoms are covalently bonded to form two dimensional layers that are stacked together through van der Waals interactions [28]. The two dimensional sheets can be rolled up to form seamless nanotubes when treated under appropriate conditions. R. Tenne et al. [29] was the first to discover such inorganic nanotubes comprising $WS_2$ which led to the further discovery of diverse inorganic tubes such as boron nitride [30, 31], metal nitride [32] metal sulfide [33], metal oxides [34 - 36] and hydroxides, silicon [37], metals [38, 39] etc..

**(i) Metal oxide nanotubes**

Metal oxide nanotubes are receiving a great deal of technological attention because of their potential for newly emerging applications in drug - delivery systems [40], molecular separation [41], single - DNA sensing [42], pollutants decomposition [43], hydrogen fuel [44], gas sensors [45] and solar energy conversion devices [46 - 48]. The applications utilize the myriad size dependant properties of metal oxides such as electrical conductivity [49], ferroelectric effects [50], piezoelectric effects [51], electro – optic effects [52], chemical sensing [49, 53], and magnetoresistance [54]. For example, $In_2O_3$ has a band gap of 3.75 eV which makes it optically transparent thereby making it a significant material for its use in liquid crystal displays [55]. ZnO and $TiO_2$ nanotubes have band gaps of 3.4 eV and 3 eV (rutile) respectively making them applicable in piezoelectric, optoelectronic, photovoltaic, and photochemical applications [56] while $Fe_3O_4$ in ferromagnetic applications [57]. Moreover, the tubular morphology of the metal oxide nanostructures plays a significant role not only because of its higher surface area but also because of its internal nanotube cavity which is several nanometers in diameter that promotes a confinement effect on metal crystallization, melting, flow, capillarity etc. [58].

Metal oxides have been synthesized using different strategies [59]. Out of them, the simplest and the most powerful approach is the template based synthesis which employs existing nanostructures as templates to serve as scaffolds for the generation of desired or novel materials with tunable dimensions. Mostly polymers [60], carbon nanotubes [61], ionic or

neutral surfactant molecules [62, 63], nanorods [64], metal salt nanofibers [65] or D- and L-tartaric acid [66] are used as templating structures. In addition to the template types, several deposition methods to coat the templates can be used such as electrochemical deposition, sol – gel synthesis, oxidation, biomimetic mineralization, and gas - phase atomic layer deposition (ALD) [67].

### 1.3 Scope of thesis

Encapsulation of nanotubes with foreign materials in particularly with metals has become a fascinating aspect in the modern nanomaterials research. The metals when embedded in the confined intratube channel of a nanotube provide scope for their promising applications in fields such as catalysis, separation, and in the development of materials with improved physical and chemical properties. Couple of years back, Gao et al. [68], reported that a low melting point, wide - liquid range metal when encapsulated inside a carbon nanotube can behave as a nanoscale thermometer. Noble metal nanoparticles of metals such as Pt, Pd and Au incorporated inside carbon based materials such as carbon nanotubes, nanofibers, nanocoils, active carbon and other carbon nanomaterials have caught much attention in the past few years because of their proposed extensive applications in catalysis, fuel cells, etc. [69]. Metal filled nanotubes are in growing demand because of their potential applications in various types of nanodevices [70].

The present study focuses on the synthesis and characterization of $SiO_2$, $TiO_2$ and $SnO_2$ nanotubes using metal salt nanofibers as templating structures. The advantage of using metal salt nanofibers as templating structures underlines the formation of nanotubes together with filling up of the nanotubes with metal in a single step. As the objective of thesis lies in incorporating platinum metal inside metal oxide nanotubes, nanofibers from two different platinum salts as templates were investigated for synthesis namely $[Pt(NH_3)_4(HCO_3)_2]$and $[Pt(NH_3)_4][PtCl_4]$, while the latter is popularly termed as Magnus green salt, abbreviated as MGS.

The Pt embedded metal oxide nanotubes thus obtained have lot of applications to their credit. $SiO_2$ nanotubes find their applications as gas adsorbents, catalyst supports, direct heterogeneous catalysts, and in bioseperation media because of the presence of large amount of Pt particles inside the tubes making them easily accessible to the reactants. C. Hippe [71]

presented the adsorption of CO on the Pt particles doped in the $SiO_2$ nanotubes in her work while T. Miyao et al. [72] reported the synthesis of catalytically active $Al_2O_3$ and $SiO_2/Al_2O_3$ nanotubes impregnated with Pt metal particles wherein the latter exhibited characteristic acidic properties. Furthermore the optical properties of $SiO_2$, makes it also applicable in opto electronic devices [73].

C. Hippe et al. [74] synthesized titania nanotubes with Pt particles embodied in them which would enhance the conductivity of semiconductor titania thereby making them potential for applications in nanoelectronics. Also, Tanaka et al. [75] and Sato et al. [76] reported the adsorption of H and CO on the $Pt/TiO_2$ nanotubes. Apart from being used as a catalyst support [77], $TiO_2$ nanotubes in general have multiple potential applications. They have been used as semiconductor materials in the construction of electronics devices, in the manufacturing of pigments and coatings, in solar cells, in sensors, in cosmetics, as photocatalysts in the degradation of organic compounds in environmental protection process etc. [78].

$SnO_2$ nanostructures on the other hand exhibit outstanding applications in optoelectronic devices, such as flat - panel displays, thin – film solar energy conversion devices, sensing of gases such as CO, $N_2$, methyl alcohol vapour, energy storage (e.g. Lithium batteries) [79] etc.. Wang et al. [80] noticed that $SnO_2$ nanotubes showed significant improvement of the electrochemical performance over the unorganized $SnO_2$ nanoparticles. They observed a specific capacity of 525 mAh/g for $SnO_2$ nanotubes inserted with $Li^+$ ions after 80 cycles which was not only higher than the nanoparticles (67 mAh/g) but also substantially greater than the theoretical value (372 mAh/g) of commercial graphite anodes [81]. In addition, A. Dieguez et al. and others [82] reported that noble metals such as Pt/Pd when incorporated into the $SnO_2$ layer demonstrate higher sensitivity and faster response to different gases when compared to their pure counterparts. The above mentioned remarkable applications of these metal oxide nanotubes create the necessity to synthesize them in a most simple and effective way.

Fig.1 depicts the schematic representation of the synthesis approach availed for synthesizing $SiO_2$, $TiO_2$ and $SnO_2$ nanotubes embedded with Pt metal. In the first step, platinum amino complexes undergo recrystallization when solvent is added to the saturated aqueous solution of the complexes giving rise to fine fiber shaped nanocrystals or in other words, nanofibers. These nanofibers are coated with metal alkoxides (such as tetra ethyl orthosilicate (TEOS)) by

sol - gel process. Subsequently, calcination at 280°C reduces the metal ions into metal clusters which either diffuse into the porous walls or reside inside the tubes.

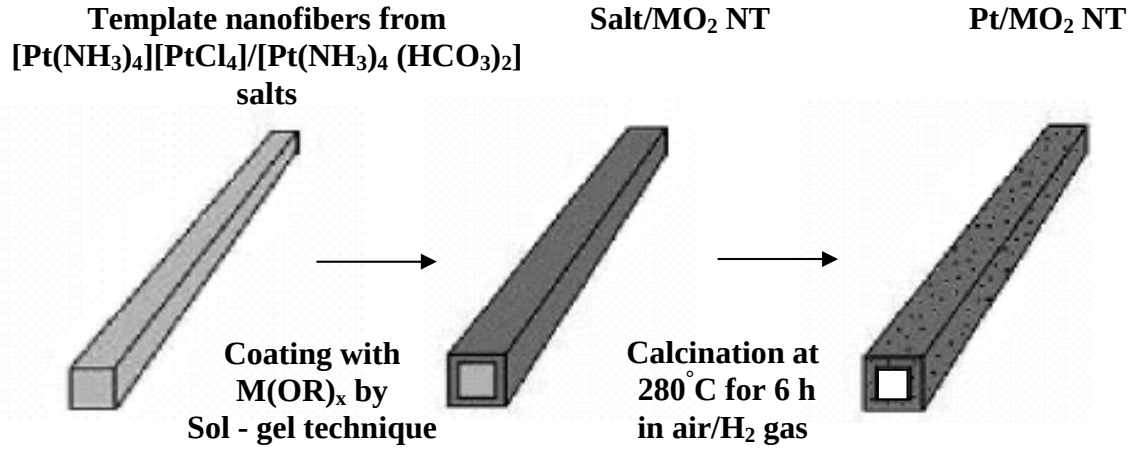


Fig. 1 Schematic representation of synthesis procedure of metal oxide nanotubes ($SiO_2$, $TiO_2$, $SnO_2$ nanotubes) embedded with Pt nanoparticles. In the present study, M = Si / Ti / Sn, x = 4, R = $-CH_2CH_3$ for Si, $-CH(CH_3)_2$ for Ti and Sn.

### 1.4 Organization of this work

**Chapter 1** deals with the brief overview of chemistry in nanometer regime, the different types of tubular nanostructures, importance of metal oxide nanotubes and their applications in various fields and finally focuses the scope and objective of the thesis concluding with a concise description of the synthesis approach of $SiO_2$, $TiO_2$ and $SnO_2$ nanotubes dealt in the study.

**Chapter 2** presents the general aspects involved in the template directed synthesis of metal oxide nanotubes. The synthetic approach presented in the thesis can be subdivided into two sections. The first part being the formation of template nanofibers from the metal salt while the second part to coat the formed template nanofibers by metal alkoxides using the sol - gel approach to incorporate metal nanofibers. Therefore this chapter discusses the crystallographic concepts that involve in the formation of crystals such as growth of crystals, crystallization chemistry and the mechanisms that explain the growth rate. In the latter part of this chapter, the sol - gel method is studied in detail. The processing steps of sol - gel method, the advantages and limitations of the sol - gel method were analyzed.

**Chapter 3** explains the different physico – chemical characterization techniques that were used in analyzing the nanotubes that evolved by synthesizing with different platinum salt nanofibers. In particularly, the size, structure, stability and solid state packing of the nanotubes were analyzed using electron microscopy, electron diffraction, X - ray diffraction, thermogravimetric analysis and dynamic light scattering spectroscopy. The solution fraction separated from the solid part of nanotubes was analyzed by the Inductive coupled plasma-mass spectroscopy to calculate the amount of reactants that were unused in the synthesis.

**Chapter 4** demonstrates the synthesis approach of metal oxide nanotubes such as $SiO_2$, $TiO_2$ and $SnO_2$ nanotubes that are synthesized using the nanofibers from $[Pt(NH_3)_4(HCO_3)_2]$ salt. L. Ren [83] in her Ph.D thesis presented the formation of monodisperse $SiO_2$ nanotubes and $TiO_2$ nanotubes with high aspect ratios using the fibers from this salt as the template. This chapter discusses also the formation of $SiO_2$ and $TiO_2$ nanotubes from $[Pt(NH_3)_4(HCO_3)_2]$ salt synthesized for comparison and the formation of template nanofibers from the salt. As a part of this thesis, $SnO_2$ nanotubes synthesized from this salt were discussed. The experimental procedures as well as the results were elucidated with the aid of characterization tools mentioned in chapter 3.

**Chapter 5** comes up with the concept of a novel salt namely $[Pt(NH_3)_4][PtCl_4]$, called as magnus salt (MGS). This chapter reports the formation of nanofibers from MGS which were used as templating structures in the synthesis of $SiO_2$ and $TiO_2$ nanotubes. The experimental procedure together with the analysis of nanotubes emerged from the synthesis were described. Nanotubes with very high aspect ratios were observed when MGS nanofibers were used as templating structures. The tubes obtained with these salt fibers had lengths upto 60 μm long and diameter in the range of 300 – 700 nm. Moreover, the tubes from this salt had higher amount of Pt incorporated (≈ 48 wt.- %) at very low temperatures thereby making it an advantageous, easier and a cost effective approach to synthesize Pt embedded metal oxide nanotubes.

Finally, **Chapter 6** gives an overview of the conclusions from the experimental approach presented in the thesis together with a brief future outlook.

**1.5 References**

[1] J. R. Heath, P. J. Kuekes, G. S. Snider, R.S Williams, *A defect-tolerant computer architecture: Opportunities for nanotechnology. Science*, **280** (1998) p. 1716.

[2] F. Rosei, *Journal of Physics Condensed Matter*, **16** (2004) 1373.

[3] A. Vinu, K. Z. Hossain, K. Ariga, *Journal of Nanoscience and Nanotechnology*, **5** (2005) 347.

[4] C. M. Niemeyer, *Angewandte Chemie - International Edition*, **40** (2001) 4128.

[5] G. M. Whitesides, B. Grzybowski, *Science*, **295** (2002) 2418.

[6] A. K. Singh, V. Kumar, Y. Kawazoe, *Physical Review B*, **71** (2005) 075312.

[7] J. S. Yang, S. Kim, Y. T. Kim, W. J. Cho, J. H. Park, *Microelectronics Journal*, (2008), in Press.

[8] F. Su , F. Y. Lee, L. Lu , J. Liu , X. N. Tian , X. S. Zhao, *Advanced Functional Materials,* **17** (2007) 1926.

[9] L. A. Abramovich, M. Reches, V. L. Sedman, S. Allen, S. J. B. Tendler. E. Gazit, *Langmuir,* **22** (2006) 1313.

[10] S. Mukherjee*, Ph.D Thesis*, Georgia Institute of Technology, USA, (2007) p.4.

[11] J. J. Nakane, M. Akeson, A. Marziali, *Journal of Physics - Condensed Matter*, **15** (2003) 1365.

[12] C. R. Martin, P. Kohli, *Nature,* **2** (2003) 29.

[13] M. Niederberger, *Ph.D Thesis*, ETH Zürich, (2007) p.5.

[14] C. Suryanarayana, C. C. Koch, *Non - equilibrium processing of materials* (1999)**,** Pergamon Materials Series.

[15] B. F. G. Johnson, *Topics of Catalysis,* **24** (2003) 147.

[16] S. Sun, K. Fujimoto, Y. Zhang, N. Tsubaki, *Catalysis Communications,* **4** (2003) 361.

[17] M. Law, H. Kind, F. Kim, B. Messer, P. Yang, *Angewandte Chemie - International Edition,* **41** (2002) 2405.

[18] G. J. Li, X. H. Zhang, S. Kawi, *Sensors and Actuators B,* **60** (1999) 64.

[19] G. Zhang, M. Liu, *Sensors and Actuators B,* **69** (2000) 144.

[20] C. Liu, Y. Y. Fan, M. Liu, H. T. Cong, H. M. Cheng, M. S. Dresselhaus, *Science,* **286** (1999) 1127.

[21] X. F. Duan, Y. Huang, R. Agarwal, C. M. Lieber, *Nature,* **421** (2003) 241.

[22] X. F. Duan, C. M. Niu, V. Sahi, J. Chen, J. W. Parce, S. Empedocles et al., *Nature,* **425** (2003) 274.

[23] S. Iijima, *Nature,* **354** (1991) 56.

[24] R. H. Baughman, A. A. Zakhidov, W. A. de Heer, *Science*, **297** (2002) 787.

[25] E. W. Wong, P.E. Sheehan, C .M. Lieber, *Science*, **277** (1997) 1971.

[26] I. A. Banerjee, L.T. Yu, H. Matsui, *Nano Letters*, **3** (2003) 283.

[27] G. A. Silva, C. Czeisler, K. L. Niece, E. Beniash, D. A. Harrington, S. I. Stupp, *Science*, **303** (2004)1352.

[28] R. Tenne, *Angewandte Chemie - International Edition,* **42** (2003) 5124.

[29] R. Tenne, L. Margulis, M. Genut, G. Hodes, *Nature,* **360** (1992) 444.

[30] N. G. Chopra, R. G. Ruyken, K. Cherry, V. H. Crespi, M. L. Cohen, S. G. Louie, A. Zettl, *Science,* **269** (1995) 966.

[31] E. J. M. Hamilton, S. E. Dolan, C. E. Mann, H. O. Colijin, C. A. McDonald, S. G. Shore *Science,* **260** (1993) 659.

[32] J. Goldberger, R. R. He, Y. F. Zhang, S. Lee, H. Q. Yan, H. J. Choi, P. D. Yang, *Nature,* **422** (2003) 599.

[33] J. Q. Hu, Y. Bando, J. H. Zhan, D. Goldberg, *Angewandte Chemie - International Edition,* **43** (2004) 4606.

[34] M. E. Spahr, P. Bitterli, R. Nesper, M. Müller, F. Krumeich, H. U. Nissen, *Angewandte Chemie,* **110** (1998) 1339 ; *Angewandte Chemie - International Edition,* **37** (1998) 1263.

[35] H. P. Lin, C. Y. Mou, S. B. Liu, *Advanced Materials,* **12** (2000) 103.

[36] M. Yada, M. Mihara, S. Mouri, M. Kuroki, T. Kijima, *Advanced Materials,* **14** (2002) 309.

[37] J. Q. Hu, Y. Bando, Z. W. Liu, J. H. Zhan, D. Goldberg, T. Sekiguchi, *Angewandte Chemie – International Edition,* **43** (2004) 63.

[38] Y. G. Sun, Y. N. Xia, *Advanced Materials,* **16** (2004) 264.

[39] T. Kijima, T. Yoshimura, M. Uota, T. Ikeda, D. Fujikawa, S. Mouri, S. Uoyama, *Angewandte Chemie - International Edition,* **43** (2004) 228.

[40] C. R. Martin, P. Kohli. *Nature Reviews Drug Discovery,* **2** (2003) 29.

[41] S. B. Lee, D. T. Mitchell, L. Trofin, T. K. Nevanen, H. Söderlund, C. R. Martin, *Science,* **296** (2002) 2198.

[42] R. Fan, R. Karnik, M. Yue, D. Li, A. Majumdar, P. Yang, *Nano Letters,* **5** (2005) 1633.

[43] X. Quan, S. Yang, X. Ruan, H. Zhao, *Environmental Science & Technology,* **39** (2005) 3770.

[44] J. Park, J, H. S. Kim, A. J. Bard, *Nano Letters,* **6** (2006) 24.

[45] (a) O. K. Varghese, D. Gong, M. Paulose, K. G. Ong, C. A. Grimes, *Journal of Sensors and Actuators B,* **93** (2003) 338 (b) O. K. Varghese, D. Gong, M. Paulose, K. G. Ong , E. C. Dickey, C. A. Grimes, *Advanced Materials,* **15** (2003) 624.

[46] S. Uchida, R. Chiba, M. Tomiha, N. Masaki, M. Shirai, *Electrochemistry,* **70** (2002) 8.

[47] (a) J. M. Macak, H. Tsuchiya, A. Ghicov, P. Schmuki, *Electrochemical Communications,* **7** (2005) 1133 (b) M. Paulose, K. Shankar, O. K. Varghese, G. K. Mor, B. Hardin, C. A. Grimes, *Nanotechnology,* **17** ( 2006) 1446 (c) G. K. Mor, K. Shankar, M.Paulose, O. K. Varghese, C. A. Grimes, *Nano Letters,* **6** (2006) 215 (d) K. Zhu, N. R. Neale, A . Miedaner, A. J. Frank, *Nano Letters*, **7** (2007**)** 69 (e) A. B. F. Martinson, J. W. Elam, J. T. Hupp, M. J. Pellin, *Nano Letters,* **7** (2007) 2183.

[48] (a) M. Adachi, Y.Murata, M. Harada, S. Yoshikawa, *Chemistry Letters,* **29** (2000) 942 (b) M. Adachi, I. Okada, S. Ngamsinlapasathian, Y. Murata, S. Yoshikawa, *Electrochemistry,* **70** (2002) 449 (c) M. Adachi, Y. Murata, I. Okada, S. Yoshikawa, *Journal of the Electrochemical Society,* **150** (2003) 488 (d) S. Ngamsinlapasathian, S. Sakulkhaemaruethai, S. Pavasupree, A. Kitiyanan, T. Sreethawong, Y. Suzuki, S. J. Yoshikawa, *Photochemistry and Photobiology A,* **164** (2004) 145.

[49] J. J. Shyue, R. E. cochran, N. P. Padture, *Journal of Materials Research,* **21** (2006) 2894.

[50] W. S. Yun, J. J. Urban, Q. Gu, H. Park, *Nano Letters,* **2** (2002) 447.

[51] Z. L. Wang, J. Song, *Science,* **312** (2006) 242.

[52] Y. Xia, P. Yang, Y.Sun, Y. Wu, B. Mayers, B. Gates et al., *Advanced Materials,* **5** (2003) 353.

[53] A. Kolmakov, M. Moskovits, *Annual Review of Materials Science,* **34** (2004) 151.

[54] C. Terrier, M. Abid, C. Arm, S. Serrano – Guisan, L. Gravier, J.-P, Ansermet, *Journal of Applied Physics,* **98** (2005) 086101.

[55] L. Dai, X. L. Chen, J. K. Jian, M. He, T. Zhou, B. Q. Hu, *Applied Physics Materials Science & Processing*, **75** (2002) 687.

[56] P. D Yang, H. Q. Yan, S. Mao, R. Russo, J. Johnson, R. Saykally, N. Morris, J. Pham, R. R. He, H.J. Choi, *Advanced Functional Materials*, **12** (2002) 323.

[57] W. T. Dong, C.S. Zhu, *Journal of Materials Chemistry*, **12** (2002) 1676.

[58] D. Golberg, Y. Bando, Y. B. Li, J. Q. Hu, Y. C. Zhu, Y. H. Gao, C. C. Tang, *AIP conference proceedings,* **723** (2004) 229.

[59] C. N. R. Rao, M. Nath, *Dalton Transactions,* **1** (2003) and the references therein.

[60] J. C. Kjeld, V. Bommel, A. Friggeri, S. Shinkai, *Angewandte Chemie - International Edition,* **42** (2002) 980.

[61] H. Q. Wu, X.W. Wei, M. W. Shao, J. S. Gu, *Journal of Crystal Growth,* **265** (2004) 184.

[62] H. P. Lin, C. Y. Mou, S. B. Liu, *Advanced Materials,* **12** (2000) 103.

[63] F. Krumeich, H. -J. Muhr, M. Niederberger, F. Bieri, R. Nesper, *Journal of American Chemical Society,* **121** (1999*)* 8324.

[64] Y. Sun, B. Mayers, Y. Xia, *Advanced Materials,* **15** ( 2003) 641.

[65] (a) C. Hippe, M. Wark, E. Lork, G. Schulz - Ekloff, *Microporous Mesoporous Materials,* **31** (1999) 235 (b) M. Wark, C. Hippe, G. Schulz - Ekloff, *Studies of Surface Science Catalysis,* **129** (2000) 475 (c) J. Zygmunt, F. Krumeich, H.-J, Muhr, R. Nesper, L.Ren, M. Wark, *Zeitschrift für Anorganische Allgemeine Chemie,* **628** (2002) 2189 (d) F. Krumeich, M. Wark H. -J, Muhr, R. Nesper, *Zeitschrift für Anorganische Allgemeine Chemie,* **630** (2004) 1054 (e) L. Ren, M. Wark, *Chemistry of Materials,* **17** (2005) 5928 (f) L. Ren, L. He, C. Chen, M. Wark, C. Li, P. Che, L. Guo, *Journal of Magnetism and Magnetic Materials,* **312** (2007) 405 (g) L. Ren, L. Guo, M. Wark, *Solid State Phenomena,* **121-123** (2007) 343 (h) C. H. Rüscher, I. Bannat, A. Feldhoff, L. Ren, M. Wark, *Microporous Mesoporous Materials*, **99** (2007) 30 (i) L.Ren, L. Guo, M. Wark, Y. Hou, *Applied Physics Letters,* **87** (2005) 212503.

[66] H. Nakamura, Y. Matsui, *Journal of American Chemical Society,* **117** (1995) 2651.

[67] C. Bae, H. Yoo, S. Kim, K. Lee, J. Kim, M. M. Sung, H. Shin, *Chemistry of Materials,* **20** (2008) 756.

[68] (a) Y. Gao, Y. Bando, *Nature,* **415** (2002) 599 (b) Y. Gao, Y. Bando, Z. Liu, D. Golberg, *Applied Physics Letters,* **83** (2003) 2913.

[69] H. S. Qian, M. Antonietti, S. H. Yu, *Advanced Functional Materials,* **17** (2007) 637.

[70] L. Shi, Y. M. Xu, Q. Li, *Nanotechnology,* **16** (2005) 2100.

[71] C. Hippe, *Ph.D Thesis*, University of Bremen, (2000) p. 58.

[72] T. Miyao, T. Saika, Y. Saito, S. Naito, *Journal of Material Science Letters,* **22** (2003) 543.

[73] H. Qian, S. –H. Yu, L. Ren, Y. Yang, W. Zhang, *Nanotechnology,* **17** (2006) 5995.

[74] C. Hippe, M. Wark, E. Lork, G. Schulz - Ekloff, *Microporous Mesoporous Materials,* **31** (1999) 235.

[75] K. Tanaka, J. M. White, *Journal of Catalysis,* **79** (1983) 81.

[76] Y. Sato, M. Koizumi, T. Miyao, S. Naito, *Catalysis Today,* **111** (2006) 164.

[77] U. Diebold, *Surface Science Reports,* **48** (2003) 53.

[78] M. A. C. Jacome, G. F. Torres, L. F. F. Ortiz, C. A. Chavez, E. L. Salinas, J. Escobar, M. L. Mosqueira, J. A. T. Antonio, *Catalysis Today,* **126** (2007) 248.

[79] J. H. He, T. H. Wu, C. L. Hsin, K. M. Li, L.J. Chen, Y. L. Chueh, L. J. Chou, Z. L. Wang, *Small*, **2** (2006) 116.

[80] Y. Wang, J. Y. Lee, H. C. Zeng, *Chemistry of Materials,* **17** (2005) 3899.

[81] (a) H. Li, Q. Wang, L. Shi, L. Chen, X. Huang, *Chemistry of Materials,* **14** (2002) 103 (b) P. Limthongkul, H. Wang, E. Jud, Y. M. Chiang, *Journal of the Electrochemical Society,* **149** (2002) A1237 (c) M. Yoshio, H. Wang, K. Fukuda, *Angewandte Chemie - International Edition,* **42** (2003) 4203.

[82] (a) A. Diéguez, A. Vilà, A. Cabot, A. Romano - Rodrıguez, J. R. Morante,J. Kappler, N. Barsan, U. Weimar, W. Göpel, *Sensors and Actuators B: Chemical,* **68** (2000) 94 (b) K.D. Schierbaum, J. Geiger, U.Weimar,W. Göpel, *Sensors and Actuators B: Chemical,* **13** (1993) 143.

[83] L.Ren, *Ph.D Thesis*, University of Hannover, 2004.

# 2

# 2. Scientific Background

The synthesis approach of platinum embedded metal oxide nanotubes portrays two important aspects namely the formation of template crystals and the coating of template nanofibers by sol - gel technique. Hence, this chapter deals with the crystallographic concepts that are essential to understand the notions of crystal growth and an elaborated study of sol - gel mechanism that allows dense and continuous oxide layers on the templating fibers for the improved production of nanotubes.

## 2.1 Crystallographic Concepts

This section explicates the crystal characteristics, structure and types of crystals, growth of crystals, defects and the mechanisms involved in the crystal growth. The formation mechanism of nanotube was also discussed with reference to literature.

### 2.1.1 Crystal and its Characterstics

Crystal can be defined as a solid built of atoms, ions or molecules that are packed in a regular repeated pattern extending in all three spatial dimensions. Unit cell is the basic building block of a crystal that pervades through the crystal lattice. The unit cells stacked in a three - dimensional space expounds the bulk arrangement of atoms in a crystal.

The structure of a crystal is determined by the arrangement of atoms in a crystal. The shape of a crystal depends on the type of molecular bonds that bind the atoms as well as the conditions under which it is formed. The formation of different shapes and sizes of the crystal can be ascribed to the internal symmetry of the crystal and relative growth rates along various directions. The growth rate of the faces of a crystal depends on the latent heat of crystallization. A face dissipates heat least effectively and therefore grows slower than edges

or corners. A more detailed explanation is given further in crystal growth in the next parts of this section.

Based on their shape, crystals can be classifed into seven crystal systems namely, triclinic, monoclinic, orthorhombic, trigonal, tetragonal, hexagonal and cubic systems while based on their physical or chemical properties, crystals are categorized into four types which include ionic crystals, covalent crystals, molecular crystals and metallic crystals. If a physical property varies in different directions then the phenomenon is named as anisotropy. Anisotropy is a characteristic feature of every crystal system while isotropic cubic crystals fall under exception.

### 2.1.2 Growth of Crystals

Though a lot of techniques are available to grow crystals, crystals are primarily grown by three methods namely,

(1) Growth from supersaturated solutions
(2) Growth from supercooled melts
(3) Growth from vapor

Crystal growth from melt and vapor are applicable for materials above melting point and sublimable compounds respectively. In view of present work, crystal growth from solution is considered. The most common method to grow crystals from solution is by crystallization process out of supersaturated solutions.

Crystallization by its basic definition means the process of arranging atoms or molecules that are in fluid or solution state into an ordered solid state. Crystallization takes place in three sequential steps namely achieving supersaturation, nucleation and crystal growth. Though the different steps of growth process are discussed as if crystallization is in the order of unconnected events, the crystallization process is inter - dependent as the system in which crystallization occurs is a continuous evolution. As nucleation and growth proceed, the overall supersaturation of the solution depletes, nucleation and growth kinetics decelerate and consequently the system tends to equilibrium where the thermodynamic factors take precedence over kinetic factors. Polymorphic modifications and phase transitions might occur

since crystals form at different times leading to different size for e.g. Ostwald ripening might take place where larger crystals grow at the expense of smaller crystals. Finally due to the change in supersaturation and impurities, a change in crystal habit usually occurs. All the different points in this process are discussed in brief that are close to our reaction system.

**(i) Achievement of Supersaturation**

The process of crystallization can take place only when a solution is supersaturated. Supersaturation refers to a state in which the solvent contains more dissolved solids (solute) than it can ordinarily accommodate at that temperature. It is a thermodynamically unstable state which can be achieved by numerous methods such as cooling or heating the solution (depending on its solubility), evaporation of solvent, addition of a non - solvent to the solution which decreases the solubility of the solid, altering the pH, dialyzing the solution [1].

The driving force for nucleation and growth is compared to the difference between the chemical potential of a molecule in supersaturated and saturated solution respectively. Mathematically, the driving force per molecule can be written as shown in Eq. (2.1).

$$\Delta\mu = k_B T \ln \frac{C}{C_s} \tag{2.1}$$

Where C is the actual concentration, $C_s$ is equilibrium constant, $k_B$ the Boltzmann constant while T is the absolute temperature. The measure of supersaturation is usually defined by $\frac{C}{C_s}$ or $\frac{C - C_s}{C_s}$ or just the difference C – Cs. The former two quantities are dimensionless as they are normalized with reference to solubility whereas C – Cs represents the amount of solute that precipitates which is dependant on the concentration units.

Hence, the variation in supersaturation can be calculated with variation in concentration of solution for e.g in our present study with the solution containing salts, the concentration can be varied by adjusting the pH with addition of ammonia. In other words, supersaturation was promoted by increase in pH as the basic aminometallic compounds are stable in alkaline medium (pH ≈ 10). The total ammonia concentration containing species $NH_3$ or $NH_4^+$ changes between the pH range 4.5 and 8. However the amount increases drastically if pH has to be increased to 10. Though ionic strength (I) varies significantly only in the pH range 6 and

8, above the latter value, there is no contribution of $NH_3$ to I as $NH_3$ is an uncharged species. However in case of $NH_4^+$, I is bound to increase resulting in the formation of soluble complexes with solute (Pt salt). Furthermore, the solubility of silica is higher at higher pH (> 7) which allows for Ostwald ripening where the particles grow in size and decrease in number at the expense of dissolution of smaller particles.

Ostwald ripening can be observed as a phenomenon in which the initially formed smaller crystals in a supersaturated solution slowly disappear with time except for a few, that grow larger at the expense of the small crystals [2]. The smaller crystals serve as nutrients for the bigger crystals. The growth of larger crystals makes the area around them depleted of smaller crystals.

Ostwald ripening process is a spontaneous occurrence as larger crystals are energetically more favoured than smaller crystals. Kinetically, formation of many small crystals is favoured while thermodynamically, large crystals are favoured. Thus, from the standpoint of kinetics smaller crystals nucleate easier. Small crystals have a larger surface area to volume ratio than larger crystals. Since, the molecules on the surface are energetically less stable than the ones already well ordered in the interior, smaller crystals exhibit lower stability. On the other hand, large crystals, with their greater volume to surface area ratio, represent a lower energy state. Thus, many small crystals would prefer to attain a lower energy state if transformed into large crystals. At times, the nucleation of smaller crystals reduces the amount of supersaturation which retards the appearance of thermodynamically favoured large crystals thereby hindering the formation of crystals by this mechanism.

Temperature also plays a prominent role in favouring the aggregation. At lower temperatures the dissolution of salt is lower and hence promotes supersaturation. In the present work, lowering the temperature proved essential to reduce the rates of hydrolysis and condensation in case of titanium alkoxides which in turn paved path for high anisotropic growth of Pt - $TiO_2$ NTs which is explained more elaborately in section 5.4.

**(ii) Nucleation**

Nucleation is the initial process in the formation of crystals wherein the assembly of atoms, ions or molecules form a three dimensional periodic array called nucleus. After attaining supersaturated solution, nuclei form according to two important mechanisms.

**(1) Primary nucleation**

Primary nucleation from a supersaturated solution can be either homogenous or heterogeneous. The latter is induced by impurities or foreign particles present in the solution while the former takes place spontaneously. Heterogeneous nucleation can be suppressed by the filtration of different solutes.

**(2) Secondary nucleation**

Secondary nucleation is induced by crystals which is pertinent to the technique of seeding. During the period preceding the formation of viable nuclei, different kinds of germ nuclei form by chemical aggregations of the precursor species and vanish again through depolymerization. As a result of such fluctuations, the germ nuclei will grow in time and form different kinds of nuclei with dimensions of critical size to become viable. The concentrations of these species are highest in the boundary layer encircling the amorphous solid particles. Presumably, nucleation occurs in these boundary regions. The rate of nucleation can be established from crystal size distribution measurements in the final crystallization product and size increase measurements of the largest crystals in the course of crystallization. As nucleation and crystal growth absorb the same precursor species, the nucleation rate is likely to go through a maximum and to decline again after a certain period of time when the consumption of precursor species by crystal growth limits their availability.

Hence in an aqueous solution where the concentration is near saturation, the crystals grow faster. As explained above, when there are more solute molecules in a given volume then the chances are likely that they come together to aggregate until they attain the critical size where the combined attractive forces between the solute molecules become stronger than the other forces in the solution which tend to disrupt the formation of these aggregates. This process can be explained as ‘in - situ aggregation’ where the aggregation takes place because of the coulomb forces existing between them. The solute molecules agglomerate to form a protocrystal which serves as a nucleation site and the other solute molecules in the solution adhere to this protocrystal thereby forming a crystal.

In our study, monodispersity was attained by following the theory proposed by Lamer and Dinegar [3]. The supersaturation of the solution was increased spontaneously by injecting the

solvent into the solution which increases the concentration of nucleation until it attains a critical concentration. With the rapid nucleation process, the precipitation of particles reduces the supersaturation below a critical point where nucleation is further not possible. Hence on the pre – formed nuclei, the growth continues until equilibrium in solubility is achieved. The theory postulates that a single particle can be formed if nucleation starts at a strike of nuclei (in contrast to the 'in – situ aggregation) and the crystal starts to grow during the growth period with the new nuclei sticking to the formed nuclei.

**(iii) Crystal Growth**

Crystal growth occurs at the crystal – solution interface by condensation of the dissolved species onto the crystal surface. Nuclei grow to crystals by multiple addition of precursor species. When a nucleus develops and grows into a crystal, it demonstrates different faces, growth mechanisms and growth rates which depend both on external factors such as supersaturation, impurities etc. and on internal factors like structure, bonds and defects.

According to the Periodic Bond Chain (PBC) theory, growth is the outcome of the consecutive formation of the strong bonds between growth units [4, 5]. In other words, PBC is an uninterrupted chain of strong bonds that repeat through the crystal in a periodic manner. According to this theory, three types of faces are observed in a crystal as shown in Fig. 2.1.

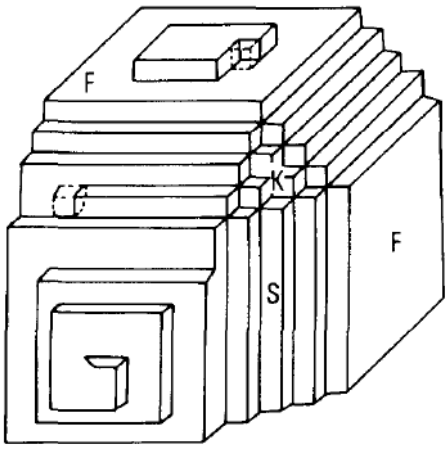


Fig. 2.1 Schematic representation of a crystal exhibiting Flat (F), stepped (S) and kinked (K) faces. Front face exhibits a polygonized growth spiral while top view exhibits a two – dimensional nucleus [1]

Flat faces have PBCs atleast in two different directions in a slice of thickness $d_{hkl}$ while stepped and kinked faces have one and no PBC in the slice $d_{hkl}$ respectively where $d_{hkl}$ represents the interreticular distance shown in dotted lines in Fig. 2.1. K faces contain only kinks where they grow by direct incorporation of atoms or molecules. Since F faces are flat, the number of kinks is very minute in contrast to K faces. Such F faces grow either by two – dimensional mechanism or spiral growth mechanism which will be discussed in brief in next parts of this section. Accordingly it can be predicted that the growth rates of F faces are smaller than the growth rate of K faces while S faces are intermediate between these two limiting cases.

As explained by Boistelle et al. [1], the growth rate of any face is supposed to be directly proportional to the attachment energy of a growth unit deposited on the top of the face under consideration. Hence, higher the attachment energy greater the time for desorption of growth unit and consequently the larger rate of growth of the face. Layer growth (F face) is alone considered over K and S faces as the latter tow faces disappear from the crystal growth morphology owing to its larger growth rates.

### 2.1.3 Crystal Defects

Perfect crystals are rare where all the unit cells consist of the ideal arrangement of atoms or molecules and all cells line up in a three dimensional space with no distortion. Ideal growth in case of perfect crystals takes place by two - dimensional nucleation [6, 7]. A two - dimensional nucleus is generated by diffusion of adsorbed molecules or growth units into the face and cluster. Once the nucleus attains critical size it gets stable and exhibits kink positions where the growth units are readily embedded as shown in Fig. 2.1 in the upper part. Further the nucleus spreads across the surface and a complete layer forms resulting in crystal growth by one monomolecular layer. Growth by this mechanism is rare and though it occurs, the controlling and adjusting the growth rates is difficult to control.

Some cells might have one or more atoms either less or more than the ideal unit cell. Such kind of misalignment of unit crystals is designated as crystal defects. Crystal defects occur as points, along lines, or in the form of a surface termed as point, line and plane defects respectively. The type of defect arising along the line is termed as line dislocation. One of such line defects is called screw dislocation which is elaborated in detail in the next part of

this section. Whiskers or ultra thin needles usually take straight needle form from the screw dislocation parallel to the needle axis [8]. In the present scenario the formation of needle shaped fibers from Pt salts seem to resemble the thin needle crystals issuing forth from screw dislocations.

**(i) Screw Dislocations**

A screw dislocation is one of the types of line defects. This dislocation results when the misalignment shifts a block of atoms gradually upwards or downwards resulting in the formation of a screw like deformation. Screw dislocations often emerge as spirals as sketched in Fig. 2.2. According to the theory of Burton et al. [9], a crystal which consists of dislocations can grow only when supersaturation is too low for two - dimensional nucleation. Where a screw dislocation terminates in a crystal face, an exposed edge is formed which, while growing, will persist and develop into spiral growth centred on the dislocation.

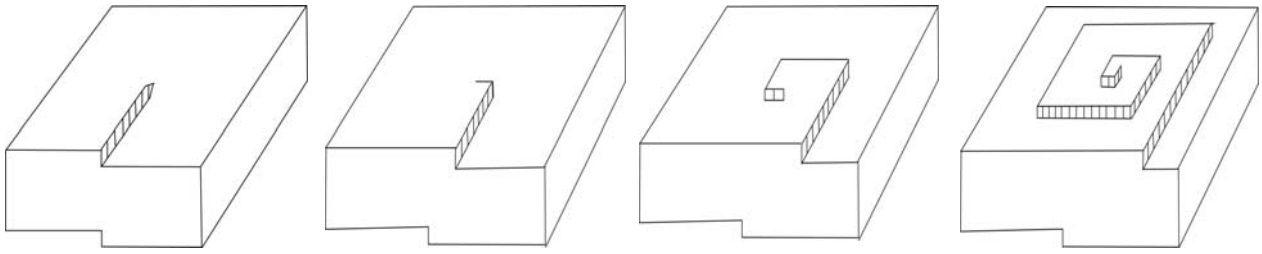

(a) (b) (c) (d)

Fig. 2.2 Schematic representation of growth of a screw dislocation from (a) – (d) [10]

When a screw dislocation protrudes from a crystal face, it provides a sequence of steps which can spread over the surface. Profile of the face growing from spiral mechanism is show in Fig. 2.3. Due to the presence of steps, the adsorbed solute molecules are trapped in more easily and growth is more regular. The steps eventually expand by rotating the emergence point of dislocation and when a step reaches the face edges, the crystal thickness is expected to increase by one monolayer.

The screw dislocations protruding on only one out of the three crystallographically equivalent faces behave as active growth centers whereas those on the other tow faces are inactive for reasons explained in section 2.1.4. while elongated whiskers form in one direction from those

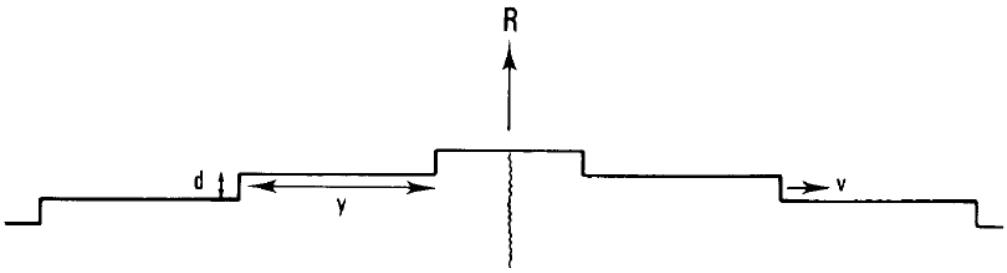


Fig. 2.3 Growth profile of a face by spiral growth mechanism [1]; d is the thickness of the monolayer, v is lateral velocity, y is the quantity from supersaturation and R is growth rate

active growth centers [11]. If screw dislocations on two faces are active as growth centers then a thin platy habit is observed. The formation of needles or whiskers is largely dependent on the growth conditions. However why certain screw dislocations are active growth centers while some inactive is still an unanswered question to the researchers. The growth of needle shaped crystals could have been either due to the minimum surface free energy of crystal faces from a thermodynamic point of view or due to the relative growth of different crystal faces from kinetics [10]. Owing to the growth of tubular templating structures into needle shaped crystals, the one - dimensional growth of templates in the present work can be attributed to the screw dislocations that arise from the imperfections of the crystal lattice. Kimura et al. [12] reported the formation of poly (azomethine) crystals through the spiral growth of oligomer lamellae are caused by screw dislocations. A similar observation was perceived by Iwata et al. [13] where the whiskers of AlN crystals seem to have originated from the screw dislocations.

### 2.1.4 Crystal habit

Crystal habit is the outcome of the relative growth rates of the faces. The smaller the growth rate, the more extensive development of the face is seen. By selectively decreasing the velocity, a face can be extended as shown in Fig. 2.4. Faces like K and S which are customarily not in the crystal morphology might develop provided their growth rates become smaller compared to the other faces. When supersaturation is higher the growth units integrate faster into the faces where the adsorption energy is largest. Needles grow longer while platelets grow wider with increase in supersaturation [1].

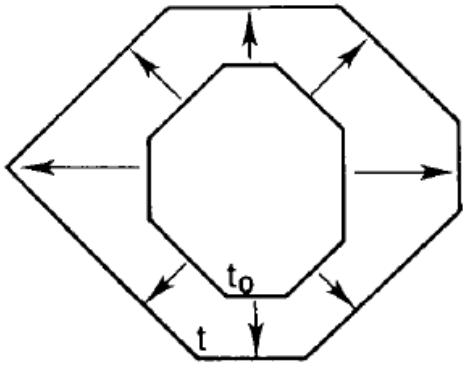


Fig. 2.4 Schematic representation of a habit change wherein faces of lowest growth rates develop at the expense of greatest growth rates [1].

### 2.1.5 Formation mechanism of nanotube

The formation of nanotubes from the templating fibers takes place merely by the coating of the salt fibers by alkoxide precursors. Although solution – based deposition processes offer a variety of oxide materials to be used in the synthesis of template - based oxide materials, they involve a difficult - to - control procedure with respect to the wall thickness especially in nanotubular structures. The surface sol – gel process allows the coating of dense and continuous oxide layers leading to improved production of template directed oxide nanotubes [14].

The present work employs the cost effective sol – gel technique to coat the template fibers with metal alkoxides which will be discussed elaborately in the next sections of this chapter. The possible mechanisms that involve in the synthesis of Pt filled metal oxide nanotubes are discussed in the respective sections.

## 2.2 Coating of Templates

As referred in the aforementioned chapter, templates can be coated by several deposition methods namely electrochemical deposition [15], sol – gel synthesis [16, 17], oxidation [18 - 20], biomimetic mineralization [21, 22], and gas - phase atomic layer deposition (ALD) [23 – 25]. Out of the available deposition methods, sol - gel method stands out as the advantageous

method for its unique characteristics. As stated above, sol - gel technique was adopted to coat the template nanofibers with metal alkoxides in the present work.

### 2.2.1 Sol – gel method

The sol – gel method is a wet - chemical synthesis technique employed for the preparation of oxide gels, glasses and ceramics at low temperature [26]. This technique attained interest eversince the group of West et al. synthesized inorganic ceramics and glass materials using silica gels [27]. In the mid of 1900, Roy et al. synthesized diversified novel ceramic oxide compositions with Si, Al, Zr having high levels of chemical homogeneity which is otherwise not feasible with customary ceramic powder methods [28, 29].

Sol - gel process, from its name, implicates transition from liquid 'sol' to 'gel' phase [30]. Fig. 2.6 illustrates the process steps involved in the sol - gel method. Typically, inorganic metal salts or metal organic compounds such as metal alkoxides or metal chlorides are used as

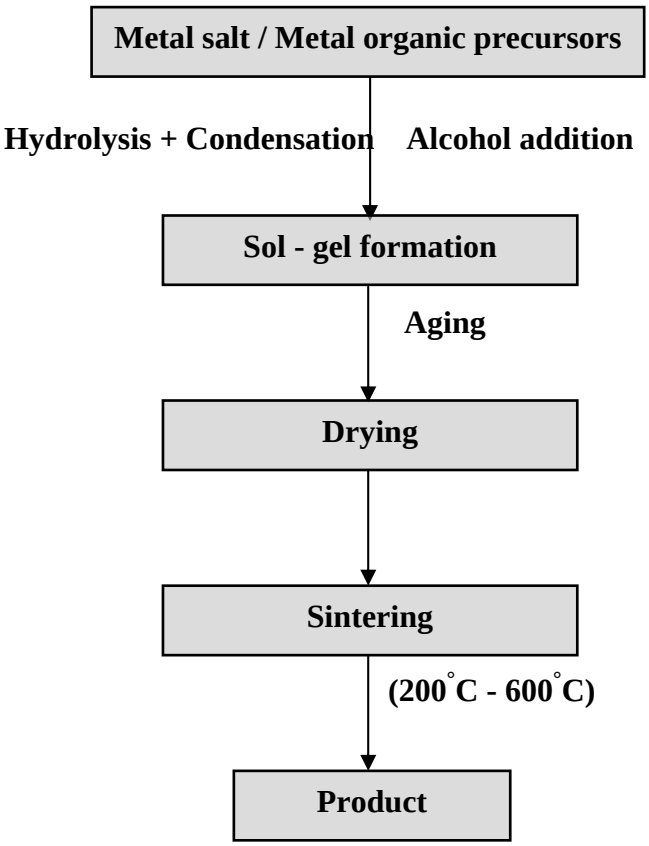


Fig 2.6 Illustration of Sol - gel Process Steps

precursors which are dispersed in a solvent to undergo a series of hydrolysis and condensation reactions to form a colloidal sol. Then the sol particles condense to form an inorganic continuous network in liquid phase (gel). Upon drying, the liquid from the gel is withdrawn to form a porous material which upon sintering favors the further condensation process and enhances the mechanical properties.

In the sol – gel process, metal alkoxide precursors are in vogue because of their ability to react with water readily. In the present study, tetraethyl orthosilicate (TEOS), tetra isopropoxy titanate, tetrabutyl orthotitanate, tin isopropoxide were used as sol - gel precursors during the synthesis of $SiO_2$, $TiO_2$ and $SnO_2$ nanotubes respectively. As water and alkoxides are immiscible, alcohols are generally used as solvents. The presence of a solvent acts as a homogenising agent which makes water mix well with the sol - gel precursor (metal alkoxide) and facilitates the hydrolysis reaction. As shown in Fig 2.6, the sol - gel method constitutes five steps.

**(i) Hydrolysis and condensation**

Although hydrolysis reaction can take place without the addition of an external catalyst, it was perceived that the presence of a catalyst can speed up the reaction. In addition, it was observed that the strength and concentration of the catalyst can influence the rate and extent of the hydrolysis reaction. In acid medium, the alkoxide group is protonated rapidly in the first step. Consequently, the electron density is withdrawn from the Si atom (in case of TEOS precursor) making it electrophilic with partial positive charges thus becoming susceptible to be attacked by the nucleophilic water molecule. Hence, a penta coordinated transition state is formed where there is simultaneous attack of nucleophile and the displacement of alcohol, R-OH. This results in decay of transition state by breaking of Si-OHR bond and ends up with the inversion of the silicon tetrahedron as shown in equation 2.1.

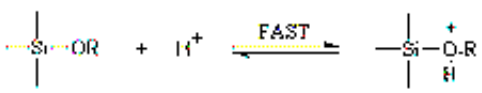


(Eq.2.1)

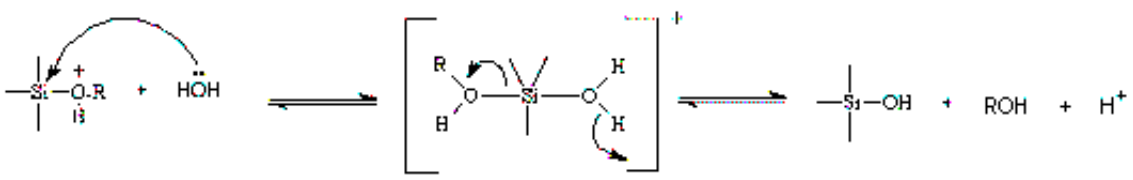

Base catalyzed hydrolysis reactions take place much more slowly than the acid catalyzed hydrolysis at an equivalent catalyst concentration. In basic medium, water dissociates to form hydroxyl anions. These hydroxyl anions act as a nucleophile and attack the Si atom. Therefore, OH displaces OR group with the inverse configuration of silicon tetrahedron. The mechanism of base catalyzed hydrolysis is explained in equation 2.2.

(Eq. 2.2)

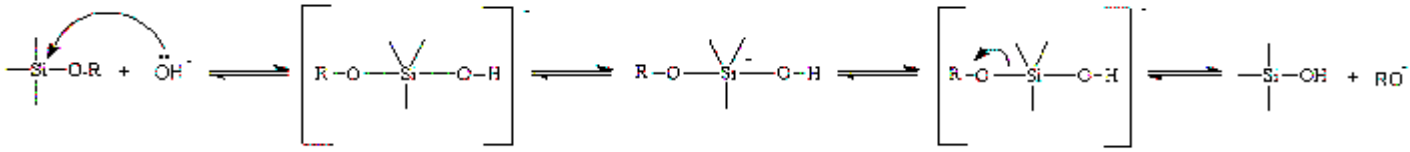

**(ii) Gel formation**

In this step, alkoxide gel precursor experiences polymerization reaction with water or alcohol molecules, i.e. the number of siloxane bonds increase when they react with water molecules and the individual molecules bridge thereby aggregating in the sol. When the sol particles interknit into a network, a gel is formed. Similar to hydrolysis reaction, the condensation step is also affected by acid/base catalyst. In presence of an acid catalyst, a weak cross linked polymer is formed which can aggregate with ease after drying yielding to a low porosity microporous structure. On the contrary when a base catalyst is used, highly branched clusters are formed leading to a mesoporous structure after gelation.

(Eq. 2.3)

(Eq. 2.4)

(Eq. 2.5)

In most of the conditions, the condensation step commences even before the hydrolysis is complete. However, the influence of parameters such as pH, $H_2O$/Si molar ratio (R) and catalyst can compel completion of hydrolysis before condensation begins. Engelhardt et al. [31] revealed that typically, condensation products are monomer, dimer, linear trimer, cyclic trimer, cyclic tetramer, and higher order rings. This sequence of condensation requires ring opening polymerizations and availability of monomers in solution. The rate of ring opening polymerizations and monomer addition reactions are dependant on the pH of the solution.

In polymerizations with pH < 2, the condensation rates are proportional to the $[H^+]$ concentration just as in case of acid catalyst. As the solubility of silica is quite low below pH 2, the formation and aggregation of primary silica particles occur together and ripening (gel network) contributes to a minute growth of particles. Thus, the gel network consists of exceedingly small primary particles.

In polymerizations with pH in the range of 2 and 6, condensation rates are proportional to the $[OH^-]$ concentration. The condensation takes place between the highly condensed species and less condensed or neutral species. This evidently implies that the rate of dimerization will be low. However, once dimers are formed, they react preferentially with monomers to form trimers, which in turn with monomers form tetramers. This cycle follows until the proximity of the chain ends and when a depletion of the monomer population occurs. The growth occurs further when lower molecular weight species are added to highly condensed species and aggregation of the condensed species form chains and networks. The solubility of silica in this pH range is also lower and therefore the growth of the particles discontinues when particles reach few nm diameter.

In the medium where pH > 7, polymerization takes place in a similar manner as that in the range of 2 > pH > 6 except that the condensed species become ionized and therefore mutually repulsive. In this case, growth occurs essentially through the addition of monomers to the highly condensed particles rather than by mere aggregation of particles. As the solubility of silica as well as the size dependence of solubility is higher in the medium with pH > 7, particles grow in size and decrease in number as highly soluble small particles dissolve and reprecipitate on larger and less soluble particles. The growth ceases when the difference in solubility between the smallest and largest particles becomes indiscernible. This process is

referred as Ostwald ripening. In this pH range, the growth rate depends largely upon the particle size distribution [32], while the particle size depends on the temperature.

**(iii) Aging**

During this process, polycondensation continues along with localized solution and reprecipitation of the gel network, which increases the thickness of interparticle necks and decreases the porosity. The gel shrinks as the non - bonded contacts are replaced by the covalent links. The formation of cross links depends on the degree of polymerization while the growth rate is controlled by the reaction conditions. The strength of the gel increases with aging. Aging plays a vital role in the sol - gel process. An aged gel must develop sufficiently so as to possess enough strength to resist cracking during drying. Moreover the tube walls become thicker with aging.

**(iv) Drying**

The gel thus obtained has a high degree of water and three dimensional interconnected pores in its structure. During the process of drying, the liquid is removed from the interconnected pore network. The removal of liquid from the pores can cause significant stress resulting from the inhomogeneous shrinkage. When the pore sizes are small (< 20 nm), the stress can be accommodated by the materials themselves while for particles with dimensions greater than 1 cm, drying stress developed in ambient atmosphere can cause gels to crack catastrophically. In the present part of work, capping agents seemed to have served as a protective coating thus inhibiting the stresses from drying.

**(v) Sintering**

The process in which the porous gel is heated to high temperatures causes densification to occur which is otherwise called sintering. Although there are reports that gel pores with functional organic or biological molecules were prepared and dried at near or room temperature, most applications demand heat treatment at high temperatures. With high temperature annealing, the pores are eliminated and the density ultimately becomes equivalent to fused quartz or fused silica. The sintering temperature depends considerably on the dimensions of the pore network, the connectivity of the pores, and surface area in the structures [33].

### 2.2.2 Advantages and limitations of sol - gel method

Sol - gel method is a flexible and cheapest technique to fabricate especially silicate materials under mild processing temperatures. The method is usually known for its following advantages:

(i) Since sol - gel method is a wet chemical process, the composition of the materials can be controlled at the molecular level. Hence, stoichiometric homogenous control of the incorporation can be achieved. Metals and metal alkoxides can be easily incorporated by this method.

(ii) As mostly liquid precursors are used, it becomes an easier approach to cast the materials in different forms without the aid of machining or melting techniques

(iii) The precursors like metal alkoxides utilized in the sol - gel method can be obtained commercially at highest purity which makes it easier to fabricate materials with high quality.

(iv) Sol - gel method is easier as the process requires lower temperatures or closer to room temperature.

In spite of its advantages, sol - gel method suffers from some limitations as well. Since the process includes water and alcohol, the method limits itself to fabricate materials which are sensitive to solvents. The stress induced cracks during the drying process cannot be healed after sintering and the process requires cautious attention in controlling the chemistry from the first step.

## 2.3 References

[1] R. Boistelle, J. P. Astier, *Journal of Crystal Growth,* **90** (1988) 14.

[2] J. D. Ng, B. Lorber, J. Witz, A. T. Dietrich, D. Kern, R. Giege, *Journal of Crystal Growth*, **168** (1996) 50.

[3] V. K. Lamer, R. H. Dinegar, *Journal of American Chemical Society,* **72** (1950) 4847.

[4] P. Hartman, *Crystal growth: An introduction, Ed. P. Hartman (North – Holland, Amsterdam),* (1973) p. 367.

[5] P. Hartman, P. Bennema, *Journal of Crystal Growth*, **49** (1980) 145.

[6] R. Kaischew, *Acta Physica Hungarica*, **8** (1957) 75.

[7] W. B. Hillig, *Acta Meterila*, **14** (1966) 1868.

[8] W. W. Webb, R. D. Dragsdorf, W. D. Forgeng, *Physical Review*, **108** (1957) 498.

[9] W. K. Burton, N. Cabrera, F. C. Frank, *Nature*, **163**, (1949) 398.

[10] L. Ren, 'Inorganic salt nanofibers as templates for the formation of oxide nanotubes' *Ph.D Thesis*, Leibniz University of Hannover, (2004) p.10, 11.

[11] I. Sunagawa, *Crystals: Growth, Morphology and Perfection*, Cambridge University Press, Science, (2005).

[12] K. Kimura, J. H. Zhuang, K. Shirabe, Y. Yamashita, *Polymer*, **44** (2003) 4761.

[13] T. Ishii, T. Sato, M. Iwata, *Mineralogical Journal,* **8** (1975) 1.

[14] N. I. Kovtyukhova, T. E. Mallouk, T. S. Mayer, *Advanced Materials*, **15** (2003) 780.

[15] (a) M. Nishizawa, V. P. Menon, C. R. Martin, *Science,* **268** (1995) 700 (b) K. B. Jirage, J. C. Hulteen, C. R. Martin, *Science,* **278** (1997) 655 (c) Y. Sun, B. T. Mayers, Y. Xia, *Nano Letters,* **2** (2002) 481 (d) Y. Sun, B. T. Mayers, Y. Xia, *Advanced Materials,* **15** (2003) 641 (e) M. Wirtz, C. R. Martin, *Advanced Materials,* **15** (2003) 455 (f) C. Mu, Y. –X. Yu, R, M. Wang, K. Wu, D. S. Xu, G. –L. Guo, *Advanced Materials,* **16** (2004) 1550 (g) T. Kijima, T. Yoshimura, M. Uota, T. Ikeda, D. Fujikawa, S. Mouri, S. Uoyama, *Angewandte Chemie - International Edition,* **43** (2004) 228 (h) W. Lee, R. Scholz, K. Nielsch, U. Gosele, *Angewandte Chemie - International Edition,* **44** (2004) 6050 (i) M. Lahav, E. A. Weiss, Q. Xu, G. M. Whitesides, *Nano Letters,* **6** (2006) 2166.

[16] P. Hoyer, *Langmuir,* **12** (1996) 1411.

[17] (a) S. O. Obare, N. R. Jana, C. J. Murphy, *Nano Letters,* **1** (2001) 601 (b) K. S. Mayya, D. I. Gittins, A. M. Dibaj, F. Caruso, *Nano Letters,* **1** (2001) 727 (c) J. Zygmunt, F. Krumeich, R. Nesper, *Advanced Materials,* **15** (2003) 1538 (d) J. –H. Lee, I. –C Leu, M- -C. Hsu, Y. –W. Chung, M. –H. Hon, *Journal of Physical Chemistry B,* **109** (2005) 13056.

[18] R. Fan, Y. Wu, D. Li, M. Yue, A. Majumdar, P. Yang, *Journal of the American Chemical Society,* **125** (2003) 5254.

[19] L. Li, Y. –W. Yang, Y. G. –H. Li, L. –D. Zhang, *Small,* **2** (2006) 548.

[20] P. X. Gao, C. S. Lao, Y. Ding, Z. L. Wang, *Advanced Functional Materials,* **16** (2006) 53.

[21] A. B. F. Martinson, J. W. Elam, J. T. Hupp, M. J. Pellin, *Nano Letters,* **7** (2007) 2183.

[22] (a) S. Baral, P. Schoen, *Chemistry of Materials,* **5** (1993) 145 (b) M. Adachi, T. Harada, M. Harada, *Langmuir*, **15** (1999) 7097 (c) M. Harada, M. Adachi, *Advanced Materials,* **12** (2000) 839.

[23] H. Shin, D. –K. Jeong, J. Lee, M. M. Sung, J. Kim, *Advanced Materials,* **16** (2004) 1197.

[24] (a) J. Hwang, B. Min, J. S. Lee, K. Keem, K. Cho, M. –Y. Sung, M. –S. Lee, S. Kim, *Advanced Materials,* **16** (2004) 422 (b) R. H. A. Ras, M. Kemell, J. de Wit, M. Ritala, G. Brinke, M. Leskela, O. Ikkala, *Advanced Materials,* **19** (2007) 102.

[25] (a) M. Daub, M. Knez, U. Gosele, K. Nielsch, *Journal of Applied Physics,* **101** (2007) 09J111 (b) M. Kemell, V. Pore, J. Tupala, M. Ritala, M. Leskela, *Chemistry of Materials,* **19** (2007) 1816.

[26] L. Yang, *Ph. D thesis*, California Institute of Technology, California, (2005).

[27] L. L. Hench, J. K. West, *Chemical Reviews,* **90** (1990) 33.

[28] G. J. McCarthy, R. Roy, J. M. McKay, *Journal of the American Ceramic Society*, **54** (1971) 637.

[29] (a) R. Roy, *Journal of the American Ceramic Society*, **52** (1969) 344 (b) R. Roy, *Journal of the American Ceramic Society*, **39** (1956) 145 (c) D. M. Roy, R. Roy R, *American Mineralogist*, **39** (1954 ) 11.

[30] J. D. Wright J. D, N. A. J. M. Sommerdijk '*Sol-gel Materials: Chemistry and applications*' Advanced Chemistry Texts. (2001): Gordon and Breach Science Publishers.

[31] V. Q. Engelhardt et al., *Zeitshrift für Anorganishe und Allgemeine Chemie*, **418** (1977) 43.

[32] C. J. Brinker, G. W. Scherer, *Sol - Gel Science: The Physics and Chemistry of Sol-Gel Processing,* Academic Press, Inc.: New York, (1990).

[33] W. Vasconcelos, R. T. DeHoff, L. L. Hench, *Proceedings of the 4th International Conference on Ultrastructure Processing of Ceramics, Glasses, and Composites*, Tucson, AZ, (1989).

# 3

# 3. Physico – Chemical Characterization Techniques

## 3.1 Introduction

The characterization of nanostructures play an integral part in all technological applications of nanostructured materials as well as a fundamental research tool for researchers working in diverse fields including Physics, Chemistry, Biology, Materials Science and Engineering. The characterization techniques of one dimensional nanotubes (presented in this thesis) elucidate the texture, chemical composition and the thermal properties of the nanotubes.

The texture of a nanotube refers to the geometric structure and the morphology ranging from the finest nanoscale to the extreme macroscale. This includes the size, shape and the thickness of the walls of the nanotube etc.. The chemical composition refers to the elemental composition, structure, proportions of the individual phases or functional groups that might be present. Thermal properties refer to the thermal stability of the nanotubes and its fraction of volatile components as a function of temperature. The characterization of nanotubes serves both as a quantitative as well as a qualitative measure for the ability of the nanotube, particularly based on its application which can further provide a scope for chemical transformation under specified conditions.

This thesis utilized the following characterization techniques:

### 3.1.1 Electron Microscopy

Electron microscopy is one of the significant characterization tools in the field of nanotechnology which provides insight about the structure, morphology and composition of the nanostructures. Electron microscopes gained prominence because of their greater resolving power thereby resulting in much higher magnifications than the light microscopes.

This section addresses the different types of electron microscopes employed in determining the structure, composition and morphology of nanotubes respectively.

**(i) Transmission Electron Microscopy (TEM)**

The TEM is a potential technique to characterize the microstructure of materials with very high spatial resolution. The TEM is most analogous to the light microscope wherein the former uses electrons instead of light (photons) to scrutinize the specimen at very fine resolutions. TEMs provide a means to go beyond the magnification and resolution limits of light microscopes, which are imposed by the wavelength of visible light (400 – 700 nm) [1].

In the TEM, the electrons are generated by thermionic emission from a heated tungsten filament and focussed by electromagnetic lenses into a very thin beam. Electromagnetic lenses have the advantage of adjusting focal length controlled by the current passing through. The interior of the electron microscope, including the sample area is maintained under high vacuum (< 0.01 Pa) to prevent the scattering of the electron beam by air molecules [2]. Particles in the electron beam pass through a condenser with high energy and high intensity to produce parallel rays that infringe on the specimen. As the attenuation of the beam depends on the density and thickness of the specimen, it is subsequently magnified by projecting the electron image onto a fluorescent screen or a photographic plate located at the bottom of the microscope to produce a so called bright field image. With reference to the morphology, the size, shape and the arrangement of particles which make up the specimen along with their relationship to each other on atomic diameters can be determined. With reference to crystallographic data, the arrangement of atoms in the specimen and their degree of order, detection of atomic - scale defects in areas a few nanometers in diameter can be studied while with reference to compositional information, the elements and compounds the sample comprises and their relative ratios, within the range of few nanometers in diameter can be analyzed [3].

**(a) Selected Area Energy Diffraction Technique (SAED)**

SAED is a crystallographic experimental technique performed within the TEM. The structural information derived from the electron diffraction patterns in conjunction with chemical information from Energy Dispersive Spectroscopy (EDS) or Electron Energy Loss

Spectroscopy (EELS) helps in identification of the phases (lattice spacing) [4]. This technique also helps in determining the orientation of the crystal (defect analysis) however it is limited to one orientation relative to the more fully developed X - Ray diffraction technique.

In TEM, when beam of high energy electrons impinge on the specimen, the atoms in the crystal act as a diffraction grating to the electrons. As a result, fraction of them diffract depending on the crystal structure while others pass through the sample without deflection. Consequently, the image on the screen of the TEM will produce a series of spots called the SAED pattern when operated in diffraction mode, where each spot corresponds to diffraction condition of the crystal structure of the specimen. If the specimen is moved under the beam, bringing different sections of it under illumination, the arrangement of the spots in the diffraction pattern will alter. However if the sample is tilted, the same crystal will stay under illumination, but different diffraction conditions will be activated and apparently diffraction spots either appear or disappear.

In the TEM column, a thin metal strip with different sized apertures is inserted in the path of the beam. This movable metal strip blocks the electron beam except for the fraction of it passing through the apertures. This aperture hole when moved to the selected section of the specimen is called the 'selected area aperture' and this section contributes to the Selected Area Energy Diffraction pattern of that section on the screen. This technique helps in identifying the crystal structures and examines crystal defects in the nano regime where X - Ray diffraction technique fails to apply.

**(b) Scanning Transmission Electron Microscopy (STEM)**

Scanning transmission electron microscopy technique is an indispensable tool for providing imaging, diffraction and spectroscopic information, either simultaneously or in a serial manner, of the specimen with an atomic or a sub-nanometer spatial resolution [5]. In the fixed beam TEM, electrons scattered by the illumination of the specimen are collected over a narrow solid angle and focused by the objective lens onto the image plane. The objective lens focuses the electron beam over specimen with atomic scale volume. The scattered electrons are then collected by diverse detectors placed behind the specimen and the image is generated by moving the focussed beam step by step over the specimen. The signals based on the scattering angle and / or energy loss provide images or diffraction patterns of the specimen

thus providing the structural and chemical information simultaneously. Fig. 3.1 illustrates the schematic diagram of the common signals that are utilized in a typical STEM instrument.

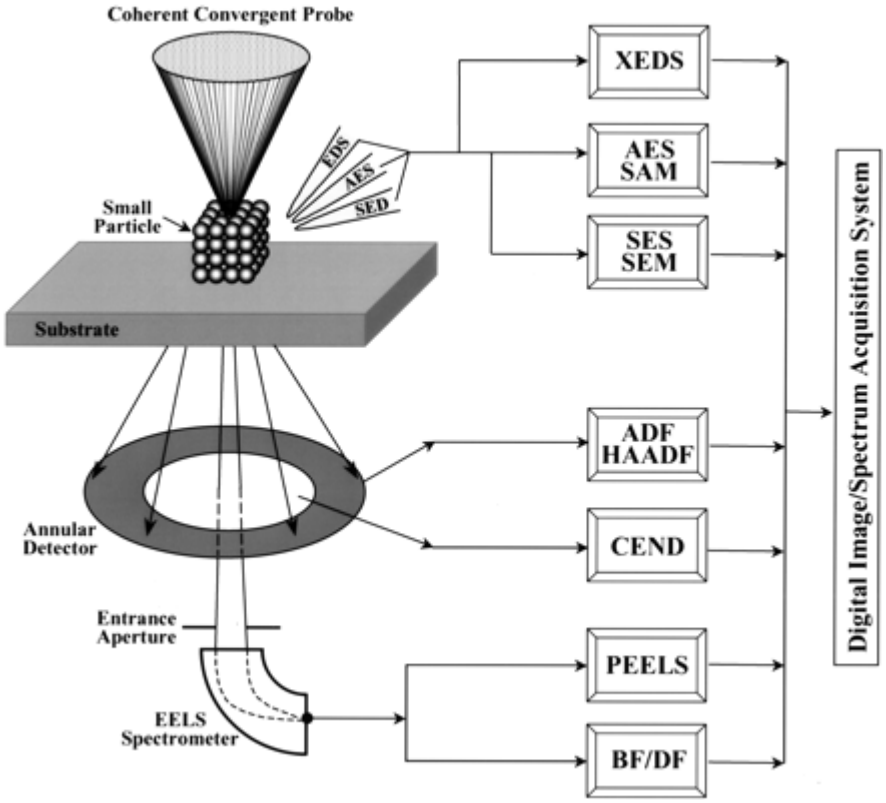


Fig. 3.1 Schematic illustration of the diverse signals generated inside a scanning transmission electron microscope [4]. X-ray energy dispersive spectroscopy (XEDS); Auger electron spectroscopy (AES) and scanning Auger microscopy (SAM); secondary electron spectroscopy (SES) and secondary electron microscopy (SEM); annular dark - field (ADF) and high-angle annular dark-field (HAADF); coherent electron nano-diffraction (CEND); parallel electron energy-loss spectroscopy (PEELS); bright - field (BF) and dark - field (DF).

The high angle scattered electrons collected from the annular detector give rise to high angle annular dark field (HAADF) images or Z contrast images. This provides the structural information on atomic level. The elastically scattered electrons intervene with the unscattered electrons to produce a phase contrast image which helps in mass determination [6]. The inelastically scattered electrons detected by Electron energy – loss spectrometer (EELS) furnish information on the electronic structure, oxidation states, and chemical composition on an atomic or sub - nanometer scale. The energy dispersive X - Ray spectroscopy

(EDXS/XEDS) manifests the quantitative information portraying elemental composition associated with inhomogeneous structures of the sample. The secondary electron (SE) and Auger electron (AE) signals can help extract data about the surface topography or surface composition of the specimen.

TEM measurements were performed at 200 kV on a field-emission instrument of the type JEOL JEM - 2100F - UHR that was equipped with a Gatan Imaging Filter (GIF 2001) and a 1024 x 1024 pixel slow – scan – charged - coupled device (CCD) camera. The imaging filter was used to enhance the signal – to - noise ratio in selected area diffraction pattern (SAED) by elastically filtering with 15 eV band width. The STEM measurements were made at 200 kV and conducted in high-angle annular dark-field (HAADF) contrast to obtain mass - thickness information. The microscope was equipped with an Oxford Instruments INCA – 200 - TEM system with an ultra - thin window that allowed performing elemental analysis by energy-dispersive X - ray spectroscopy (EDXS). To obtain TEM specimen, the suspension was deposited onto a holey carbon supporting film over a 300 mesh copper grid (Quantifoil, Multi-A) and dried under an infrared lamp.

**(ii) Scanning Electron Microscopy (SEM)**

Scanning electron microscope studies the morphology of the solid specimen using high magnification (40000x) and high resolution (1 nm). During SEM inspection, a beam of electrons emerging from the electron gun focus on a spot volume of the specimen which further attributes in the transfer of energy to the spot. These bombarding electrons, also termed primary electrons, knock out electrons from the specimen itself. The knocked out or dislodged electrons, also known as secondary electrons, are attracted and collected by a positively biased grid or detector, maintained at a positive voltage with respect to the specimen and then translated into an electrical signal. The number of secondary electrons emitted and that reach the detector relies on the topography of the surface. The electron beam when swept across the area being inspected produces many signals which are thereby collected, amplified, and displayed on a cathode ray tube. The electron beam and the cathode ray tube scan synchronously and the brightness of the picture at any point is made proportional to the number of secondary electrons reaching the detector at that instant. This gives rise to a reconstructed image of the specimen surface with high points appearing bright and valleys appearing dark. By tilting the specimen with respect to the electron beam

produces realistic shadows that in turn result in a remarkable three dimensional effect to the picture. Unlike TEM, the electron beam in a SEM is non - intrusive to the specimen.

Apart from the secondary electrons, the primary electron beam results in the emission of backscattered (or reflected) electrons from the specimen. Backscattered electrons exhibit more energy than secondary electrons, and have a definite direction. Therefore, they can not be collected by a secondary electron detector, unless the detector is directly in their path of travel. Vacuum environment is maintained inside the microscope column to avoid the presence of air molecules, which can cause a collision to the electron beam and/or can react with the specimen. If gas molecules react with the specimen, different compounds form and condense on the specimen which lowers the quality of the image.

The SEM can also be used as a microprobe to determine the compositional analysis of the specimen. The electron beam when focused on a single particle results in the emission of characteristic X - rays which are detected by the EDXS. The EDX analysis helps in identifying the elemental composition of the specimen.

SEM measurements were recorded on a JEOL JSM – 6700 F microscope and operated at a voltage of $V_{acc}$ = 2 kV in order to reduce the build up of electric charge on the surface of the specimen. EDXS measurements were performed on Oxford instruments INCA 300 which is rigged within SEM.

### 3.1.2 X - Ray Diffractometry (XRD)

XRD is one of the primary techniques used by mineralogists and solid-state chemists to extract the chemical composition and crystallographic structure of the crystalline materials. When monochromatic X - radiation strikes adjacent atomic planes of a crystal, the scattered rays interfere with each other as they leave the crystal. When certain geometric requirements are met, the scattered X - rays from the crystalline planes interfere constructively, producing a diffracted pattern. This was proposed by W. L. Bragg in 1912. Bragg's law defines the above concept mathematically [Eq. (3.1)] therefore stating that when X - rays are projected with a wavelength of $\lambda$ on to the atoms, they reflect with an angle equal to the angle of incidence $\theta$ [3]. This is depicted in Fig. 3.2.

$$n\lambda = 2d\sin\Theta \qquad \text{Eq (3.1.)}$$

Where, d represents the interatomic spacing (A°), n the order of reflection, λ is the wavelength of X - ray (A°) and θ is the angle of diffraction (°).

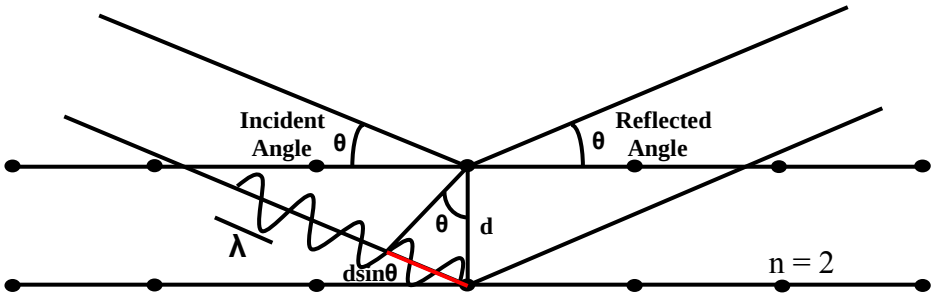


Fig. 3.2 Reflection of X-rays from two planes of atoms in a solid [3]

**(a) X - Ray Powder Diffraction**

The X - ray diffraction experiment consists of an X - ray source, the sample for investigation and a detector to pick up the diffracted X - rays. The X-ray radiation most commonly used is that emitted by copper, whose characteristic wavelength for the K radiation is 1.5418 Å. When the incident beam strikes a powder sample, diffraction occurs in every possible orientation of 2θ. For practical reasons the diffractometer measures the angle 2θ. The diffracted beam may be detected by using a moveable detector such as a Geiger counter, which is connected to a chart recorder. Normally, the counter is set to scan over a range of 2θ values at a constant angular velocity. Customarily, 2 theta with range between 10 and 100 degrees is sufficient to cover the most useful part of the powder pattern. Crystallinity can be quantitatively measured from the X - ray diffraction patterns. In general, peak heights are used to measure the crystallinity provided the crystals are larger than 0.3 micron. Apart from that, peak areas also can be used to measure the crystallinity. Furthermore, the Scherrer method helps in determining the crystallite size according to Eq. 3.2 where it offers a relation between crystallite size and peak broadening [7].

$$B_{size} = \frac{K\lambda}{L\cos\theta} \qquad (3.2)$$

where $B_{size}$ is the width (in radians) of the peak due to size effects, λ is the wavelength of the X – Ray, K is a constant whose value is close to 0.9 (0.89 <K<1), L is the crystallite length and θ being the Bragg angle.

The powdered XRD patterns of the samples were recorded on a Philips PW 1729 spectrometer (voltage = 40 kV, current intensity = 40 mA). The intensity data were performed by a step scan with 2 theta range between $10^{\circ}$ and $100^{\circ}$ with a step size of 0.03 and measuring time of 5 seconds per step.

### 3.1.3 Inductively Coupled Plasma Emission – Mass spectrometry (ICP-MS)

ICP is an analytical technique with a very high temperature (10,000 K) excitation source that dissolves, vaporizes and ionizes atoms. This excitation source reduces the molecular interferences though does not eliminate completely [8]. The ICP instrument is designed to generate plasma, which is a gas in which atoms are present in an ionized state. The basic set up of an ICP consists of three concentric tubes, most often made of silica. These tubes namely the outer loop, intermediate loop, and inner loop, collectively make up the torch of the ICP. The torch is situated within a water-cooled coil of a radio frequency (r.f) generator. As flowing gases are introduced into the torch, the r.f field is activated and the gas in the coil region is made electrically conductive. This sequence of events form the plasma.

The formation of the plasma is dependent upon an adequate magnetic field strength and the pattern of the gas streams follows a particular rotationally symmetrically pattern. The plasma is maintained by inductive heating of the flowing gases. The induction of a magnetic field generates a high frequency annular electric current within the conductor. The conductor, in turn, is heated as the result of its ohmic resistance.

In order to prevent the possible short-circuiting as well as meltdown, the plasma must be insulated from the rest of the instrument. Insulation is achieved by the concurrent flow of gases through the system. Three gases flow through the system. The outer or coolant gas, intermediate or auxiliary gas, and inner or nebulizer (or carrier gas). The outer gas is typically Argon or Nitrogen. The outer gas has been demonstrated to serve several purposes including maintaining the plasma, stabilizing the position of the plasma, and thermally isolating the

plasma from the outer tube. Argon is commonly used for both the intermediate gas and inner or carrier gas. The purpose of the carrier gas is to convey the sample to the plasma.

The instrument was Thermo X7, Thermo Electron Corp. The outer, inner and auxiliary gas utilized was argon. The analysis was performed with a power of 1200 W in a peak jump mode with 100 sweeps per each run. The dwell time was 10 milli seconds. Total of 5 runs were carried out. The carrier or auxillary gas was pumped at 0.75 l/min while the nebulizer and coolant were pumped at 0,94 and 13,0 l/min respectively. For analysis, the sample (solution) was stabilized with 5 drops of 48% HF, 5 mL of 32% HCl and diluted with deionized water to make up to 100 g.

### 3.1.4 Dynamic Light Scattering Spectroscopy (DLSS)

DLSS (also called PCS – Photon Correlation Spectroscopy) is a technique to determine the size distribution of particles suspended in a liquid. The undissolved particles in the liquid are never stationary and move in a random pattern termed as 'Brownian motion'. Brownian motion is the movement of the particles due to the random collision with the molecules of the liquid that surrounds the particle.

According to Einstein's kinetic molecular theory, molecules that are much smaller than the particles impart a change to the direction of the particle and its velocity. This is empirically shown in Eq. 3.3

$$D = \mu_p k_B T \tag{3.3}$$

where D is the diffusion coefficient, $\mu_p$ defines the mobility of the particles, $k_B$ the Boltzmann constant and T, the absolute temperature.

An important feature of Brownian motion for DLS is that larger particles move more slowly than the smaller particles under the same temperature. The diffusion co – efficient is defined in the Stokes - Einstein equation as shown in Eq. 3.4 [9].

$$D = \frac{k_B T}{6\pi\eta r} \tag{3.4}$$

where η is the viscosity of the medium

When the particles in the liquid are illuminated by a coherent source of light such as laser, the particles will scatter the light in all directions. The intensity of the scattered light fluctuates at a rate that is dependent upon the size of the particles. For larger particles, the intensity fluctuates slowly while it fluctuates faster for smaller particles. The DLSS measures the rate of the intensity fluctuation and then employs it to calculate the size of the particles.

The DLSS consists of a component called digital correlator which measures the degree of similarity between two signals over a period of time. If the intensity signal at one point of time (say t) is compared to the intensity signal, after a short time later ($t_1 + \Delta t$), the two signals will appear either similar or strongly correlated. When compared further, it can be observed that the correlation reduces with time which is represented graphically in Fig. 3.3.

When the intensity signal is compared to the intensity at much later time $t_2$, the two signals will show no relation to each other as the particles move in random directions due to Brownian motion. This explains that there exists no correlation between the signals or correlation is reported as 0. When the signal intensity is compared to itself then it would portray perfect correlation as the signals are identical and represented as Fig. 3.1 in the figure.

The graph explicates that the rate of decay for the correlation function is related to the particle size as the rate of decay is much faster for small particles that it is for the large. The software further uses algorithms to extract the decay rates for a number of size classes to produce a size distribution. The fundamental size distribution generated by DLS is an intensity distribution which can be converted to a volume distribution using Mie theory [10]. Mie theory calculation describes an analytical solution for scattering of electromagnetic radiation by spherical particles which relate the cross - sectional area of scattering $\sigma_s$ [$cm^2$] to the true geometrical cross - sectional area of the particle $A = \pi a^2$ [$cm^2$] as shown in Eq. 3.5.

$$\sigma_s = Q_s A \tag{3.5}$$

Where $Q_s$ represents the scattering efficiency parameter. The scattering power not only depends on the particle's scattering cross - section but also on the volume of particles of each size (in the case of a distribution).This volume distribution can be further converted to number distribution.

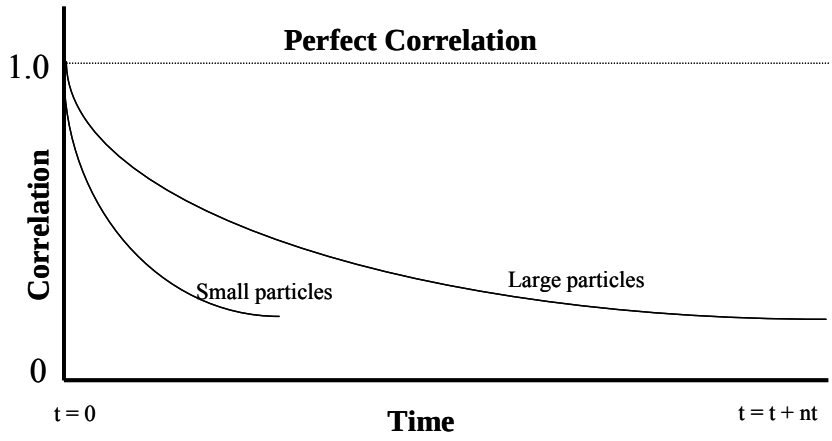


Fig. 3.3 Graph representing correlation as a function of time

The present study utilized the DLS data collected on a Malvern Zeta sizer Nano –ZS. The scattering angle was 90° and the laser wavelength was 720 nm. The autocorrelator delay was 1 µs. 3 runs with 15 scans were performed on each sample, each with a 10 s acquisition time. Initial cumulant analysis [11] was availed to dispose the uncharacteristic or erroneous scans affected by scattering from stray particles (e.g. dust) in the sample.

### 3.1.5 Thermogravimetric Analysis (TGA)

TGA is a thermal analysis technique used in measuring changes in the weight of a specimen as a function of temperature or time. In this testing procedure, the changes in weight of a specimen are recorded as the specimen is heated in air or in a controlled atmosphere such as nitrogen from room temperature (20° C) to 1000° C. TGA curve provides information concerning the thermal stability of the initial sample, intermediate compounds that may be formed and of the residue if any. In addition to thermal stability, the weight losses observed in TGA can be quantified to predict the pathway of degradation or to obtain compositional information. The ability to vary atmosphere during the TGA evaluation, particularly from an inert to a reactive gas, provides additional information about a material composition and its stability [12].

A sample is placed into a tared TGA sample pan which is attached to a sensitive microbalance assembly. The sample holder portion of the TGA balance assembly is subsequently placed into a high temperature furnace. The balance assembly measures the initial sample weight at

room temperature and then continuously monitors changes in sample weight (losses or gains) as heat is applied to the sample. TGA tests may be run in a heating mode at some controlled heating rate, or isothermally. Typical weight loss profiles are analyzed for the amount or percent of weight loss at any given temperature, the amount or percent of noncombusted residue at some final temperature, and the temperatures of various sample degradation processes.

TGA is valuable when used in conjunction with methods such as differential scanning calorimetry (DSC) and differential thermal analysis (DTA) which not only investigates a weight loss due to degradation or decomposition upon thermal changes, but also distinguishes the chemical structures that are given off. Fig. 3.4 depicts the schematic representation of TG - DTA analysis.

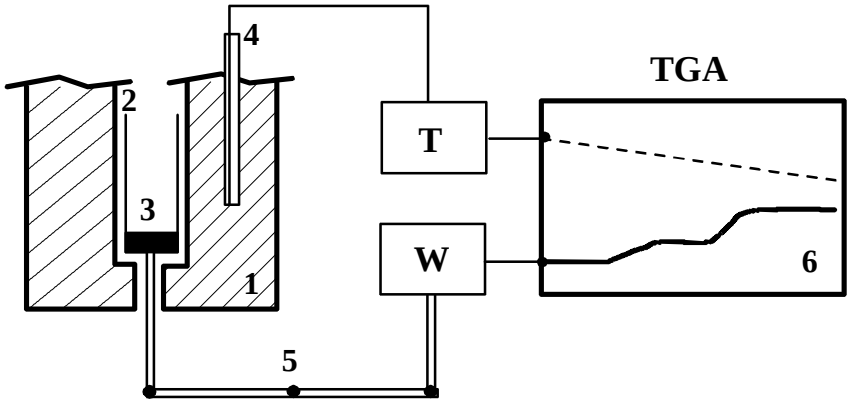


1. Heating furnace
2. Sample holder
3. Sample
4. Thermocouple
5. Balance for recording weight changes in heated sample
6. Thermogravimetric curve

Fig. 3.4 Schematic representation of TG - DTA [12]

In the present study, TGA) and DTA measurements were carried out simultaneously on a Netzsch STA429 thermoanalyzer. The measurements were carried out from room temperature to 1000$^{\circ}$C at a heating rate of 1$^{\circ}$C/min in air.

### 3.2 References

[1] D. B. Williams, C. B. Carter, '*Transmission Electron Microscopy*' Plenum publishers, New York, (1996).

[2] W. C. Hinds, '*Aerosol Technology*', 2nd edition, John Wiley & Sons., Inc. (1998) p.418.

[3] G. Ertl, H. Knözinger, J. Weitkamp, '*Hand Book of Heterogeneous Catalysis*' Vol.2, Wiley - VCH, Weinheim, (1997) p.1264.

[4] S. Turner,V. L. Karen, D. S. Bright, *Microscopy Microanalysis,* **9** (2003) 2.

[5] J. Liu, *Journal of Electron Microscopy,* **54** (2005) 251.

[6] B. D. Cullity, *Elements of X – Ray diffraction, Addison – Wesley*, Reading, MA (1978) p. 100 – 103.

[7] H. M. Rietveld, *Journal of Applied Crystallography,* **2** (1969**)** 65.

[8] M. Devadas, *Ph.D Thesis*, ETH Zürich, (1996) p.28.

[9] A. L. Kholodenko, J. F. Douglas, *Physical Review E,* **51** (1995) 1081.

[10] G. W. Petty, *Atmospheric Radiation*, 2nd edition Sundog publishing, Madison, Wisconsin., (2006) p. 351

[11] B. Wyn, *Dynamic light scattering: the method and some applications*, Clarendon press, Oxford university press, **49** (1993) p. 735.

[12] C. Aresipathi, *Master thesis*, University of Erlangen – Nürnberg, (2004) p.32.

# 4

# 4. Formation of Pt incorporated metal oxide nanotubes using $Pt(NH_3)_4(HCO_3)_2$ fibers as templates

## 4.1 Introduction and objective

The present chapter demonstrates the synthesis and characterization of metal oxide nanotubes such as $SiO_2$, $TiO_2$ and $SnO_2$ nanotubes incorporated with Pt metal employing the fibers of $Pt(NH_3)_4(HCO_3)_2$ as templating structures. As stated in Chapter 1, noble metals when embedded inside oxide nanotubes induce novel functional properties leading to diverse applications in nanoelectronics and nanodevices. Metals with low melting points like Gallium and Indium when embedded inside a nanotube core, function as nanothermometers wherein the expansion and contraction of the liquid inside the tube linearly follows the change in the environmental temperature [1, 2]. $In_2S_3$ filled $SiO_2$ nanotubes not only find their potential applications in catalysis, biochemical separation but also in photovoltaic and optoelectronics due to the high photoconductive and luminescent properties of Indium sulphide [3]. Wang et al. [4] reported that the immobilization of silver inside hollow silica nanotubes exhibits excellent antibacterial performance against Escherichia coli (E. coli), Staphylococcus aureus (S. aureus) and bacillus apart from their applications in optoelectronics. In addition they observed better dispersion of Ag particles in hollow tubes than spheres because of the tube cavity that allows for more particles to be encapsulated inside the outer and inner surfaces of the tube that allows for less loss of particles when compared to the spheres.

Traditionally, metals can be incorporated into the nanotubes chemically by wet chemical method [5], physically by capillary forces [6] and through evaporation by arc discharge method [7]. However, most of the methods are restricted to limited material systems [8] because of the complexity of the experimental set up, consumption of long time and sometimes the structural integrity of the metal oxide might degrade due to its sensitivity to the reaction conditions. Hence a simple synthesis strategy to synthesize metal filled nanotubes

with diameter in nanometer precision becomes a challenging task for potential nanotechnological applications. As reported by G. R. Patzke et al. [9] the encapsulation of a single nanotube with foreign materials by the rod – in – tube approach would be an outstanding method of intrinsic functionalization and creation of unique nanocomposite materials. Therefore the present work presents a simple synthetic approach to prepare oxide nanotubes filled with Pt metal using fibers of $Pt(NH_3)_4(HCO_3)_2$ salt as templating structures.

The synthesis approach from the present study holds advantages over the customary methods for following two reasons:

(i) Synthesis and filling of nanotubes with metal nanoparticles by subsequent calcination can be achieved simultaneously
(ii) High amount of metal can be incorporated at low temperatures

Additionally the utilization of capping agents in the present approach has yielded monodisperse and high aspect ratios of nanotubes kinetically controlling their anisotropic growth. This was evident from earlier work in our laboratory by L. Ren [10] wherein $SiO_2$ and $TiO_2$ nanotubes were synthesized from $Pt(NH_3)_4(HCO_3)_2$ fibers with aspect ratios ranging between 400 and 600.

The present investigation primarily describes the synthesis and characterization of Pt doped $SnO_2$ nanotubes availing the nanofibers of $Pt(NH_3)_4(HCO_3)_2$ salt. However, $SiO_2$ and $TiO_2$ nanotubes were also synthesized for comparison and reported. The analysis was based on the use of complementary characterization techniques to probe the structure, morphology and dimensions of the nanotubes in the solid state as well as aqueous phase. Samples withdrawn at optimized time intervals from the nanotube synthesis reactor were characterized using Scanning electron microscopy (SEM), Transmission electron microscopy (TEM), Selected area electron diffraction (SAED), Energy dispersive X-ray analysis (EDXS), X-ray diffractometry (XRD), Thermogravimetric analysis (TGA) and Inductively Coupled Plasma Emission – Mass spectrometry (ICP - MS). The combination of these characterization techniques revealed new aspects in the process of nanotube formation and their structure, which will be discussed in the next sections of this chapter.

## 4.2 Templating structures from $Pt(NH_3)_4(HCO_3)_2$ salt

### 4.2.1 Introduction

Out of the processing methods investigated to synthesize one dimensional tubular structures, template assisted approach stands advantageous because of its facile fabrication, diversity in composition of materials and uniform sizes of the formed nanotubes [11]. Since template - engaged synthesis of nanotubes limits its dimensions to that of the template, the morphology of the templating structures plays a vital role in deciding the final morphology of the nanotubes. Diverse nanostructures have been used as scaffolds for the generation of oxide nanotubes such as polymers [12], carbon nanotubes [13] or ionic or neutral surfactant molecules [14, 15], metal nanorods [16] and D - and L - tartaric acid [17] including metal salt fibers [18]. Although most of these templates result in a relatively facile synthesis process for synthesis of oxide nanotubes with controlled diameters, additional process steps are required to incorporate metal nanoparticles into the tubes as stated above though metal salt fibers stand advantageous in this aspect.

The present section deals with the formation of template fibers from $Pt(NH_3)_4(HCO_3)_2$ salt, influence of parameters such as temperature, concentration of the salt, rate of solvent addition etc. on the morphology of templating structures together with the proposed mechanism for narrow size distribution of template formation.

### 4.2.2 Experimental details

#### (i) Chemical reagents utilized

Reagents used in the preparation of template nanofibers include $Pt(NH_3)_4(HCO_3)_2$ salt (Chempur), ethanol (99.9%, Merck), aqueous ammonia solution (25%, Merck) and $H_2O$ (deionised). All the reagents were used as supplied.

#### (ii) Formation of templating fibers from $Pt(NH_3)_4(HCO_3)_2$ salt

Typically, 0.0025 mmol of $Pt(NH_3)_4(HCO_3)_2$ salt was dissolved in 2 mL of 0.4 N aqueous ammonia solution and placed in a bath maintained at $0^{\circ}C$. The transparent solution turned

turbid when 2 mL of ethanol was added rapidly into the mother solution at a stirring rate of 300 rpm. The immediate formation of precipitates from the salt portends the onset of primary nucleation.

Samples of suspension were collected at varied reaction conditions and directly dropped on a polished surface of a brass sample holder. The samples were dried in air and subjected to analysis. SEM was used as a primary tool for characterizing templating fibers.

### 4.2.3 Mechanistic pathway for formation of Template fibers

#### (i) Formation of nanofibers from $Pt(NH_3)_4(HCO_3)_2$ salt

As stated in chapter 1, platinum amino complexes ($Pt(NH_3)_4(HCO_3)_2$ in present case) are dissolved in saturated aqueous ammonia solution and with addition of ethanol undergo re - precipitation giving rise to fine fiber shaped nanofibers. Water readily dissolves the $Pt(NH_3)_4(HCO_3)_2$ salt while ethanol works as a poor solvent inducing precipitation. Due to the strong tendency of tetraaminoplatinum salt to grow into one - dimensional morphology, rapid addition of ethanol immediately led to the formation of precipitated fibers.

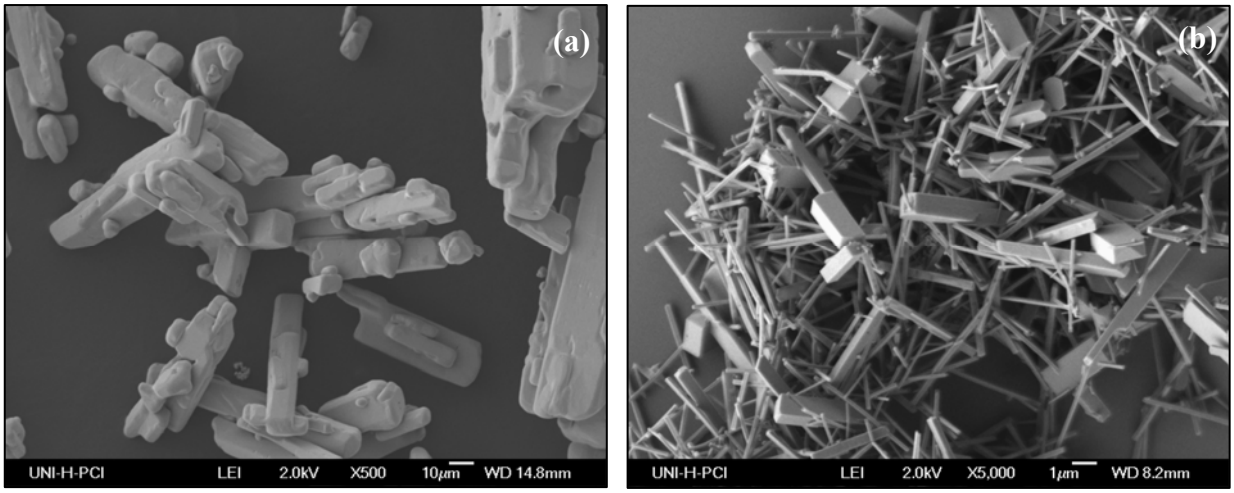


Fig. 4.1 SEM images of (a) Commercial $Pt(NH_3)_4(HCO_3)_2$ salt (b) Template fibers of $Pt(NH_3)_4(HCO_3)_2$ salt after re - precipitation with ethanol

Figure 4.1 (a) shows the SEM image of commercial $Pt(NH_3)_4(HCO_3)_2$ salt which already exhibits one dimensional morphology. Though the particles do not exhibit a uniform shape throughout the length of the tube few of them show defined rectangular cross section (as

indicated by arrow marks in the image) while few showed curved ends. Further it can be noticed that the particles are very thick with diameter in the range of 8 – 20 μm.

The aqueous solution of $Pt(NH_3)_4(HCO_3)_2$ attains state of supersaturation due to the insolubility or sparing solubility of Pt salt in ethanol. In the present study, lowering the temperature of reaction to $0^{\circ}C$ would also have helped in reaching the supersaturation. The building blocks from the salt aggregate to form nuclei which serves as a seed for the anisotropic growth of intermediate nanofibers. The intermediate nanofibers upon aging partially grow into a mixture of microfibers and nanofibers as shown in Fig. 4.1 (b). The templating fibers after re – precipitation with solvent exhibit diameters in the wide range of 100 - 1000 nm with an average length of 6 μm. The study clearly shows that the size distribution of particles from commercial salt significantly reduced with the addition of ethanol. Suitable templating structures for the formation of uniform nanotubes can be achieved by controlling the morphology of Pt salt fibers. The morphology of the precipitated fibers from $Pt(NH_3)_4(HCO_3)_2$ depends on a number of parameters that can be varied to obtain homogeneous fibers which will be discussed in detail in the next parts of this section.

From the fibers emanated from $Pt(NH_3)_4(HCO_3)_2$ salt, a formation mechanism was deduced as illustrated in Fig. 4.2. When the solvent, ethanol was dropped into the solution the aqueous solution of $Pt(NH_3)_4(HCO_3)_2$ salt starts to concentrate forming ions or building blocks. As the concentration of the ions increases, the unstable ions aggregate until they attain a critical size which is more stable giving rise to a nucleation site as elaborated in (homogeneous nucleation in section 2.1.2). These nuclei encounter other ions in the solution depending on the availability of ions eventually by anisotropic growth into intermediate nanofibers. These unstable intermediate nanofibers laterally aggregate to form bundles. As shown, upon aging

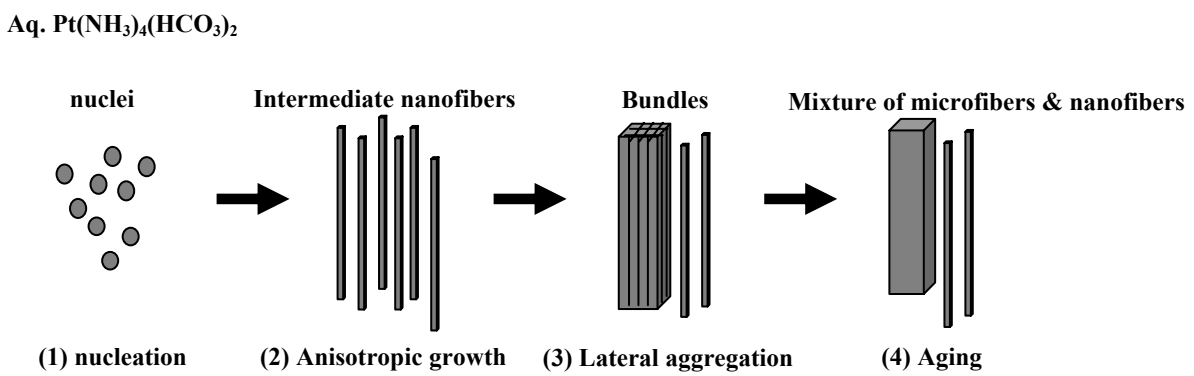


Fig. 4.2 Formation mechanism of fibrous structures from aqueous $Pt(NH_3)_4(HCO_3)_2$ salt [15]

the fibers gradually transform into fibers of micrometer and nanometer thick. A similar anisotropic growth of $Pt(NH_3)_4(HCO_3)_2$ salt fibers was observed by L. Ren et al. [19].

The addition of ethanol into aqueous $Pt(NH_3)_4(HCO_3)_2$ leads to supersaturation state due to its poor solubility in ethanol. As explained in section 2.1.4, when supersaturation is higher the growth units integrate faster on the faces where the adsorption energy is largest. As the surface energies of the nuclei are different, the continuous providing of building blocks results in the nuclei serving as seeds for further anisotropic growth. As reported by C. Hippe et al. [20], the strong tendency of tetraaminoplatinum salt to grow into one - dimensional morphology is due to its high anisotropy in the crystallographic structure owing to the unit cell of the $Pt(NH_3)_4(HCO_3)_2$ salt that slightly enlarges in the $c$ – direction. Hence the (001) face might possess the highest surface energy consequently leading to faster growth. If the preferred growth commences in a direction, the attachment of further nuclei leading to imperfections on the growing face enhances the growth further resulting in long and thin fibers. Such an anisotropic bonding in crystallographic structure can be compared to minerals such as asbestos, chrysolite and amosite in literature [21] that also possess a tendency of growing into bundles and longer lengths.

In accord with Xia et al. [22] it can be observed that the control of dimension, morphology and monodispersity becomes the key issue in synthesis of nanostructures. Since the reaction parameters play a critical role in the precipitation of fibers, its influence on the morphology was studied and optimized to obtain fibers with narrow size distribution for further synthesis process.

**(ii) Strategy for formation of fibers with narrow size distribution**

From the earlier studies it was observed that there is lateral aggregation of fibers leading to larger size distribution. The phenomenon of aggregation to larger particles to minimize surface energy is a general tendency [23]. However in the present strategy the addition of capping agent prohibits the aggregation of intermediate nanofibers and was also noticed to promote the anisotropic growth of $Pt(NH_3)_4(HCO_3)_2$ salt fibers. Fig. 4.3 explains the schematic representation of the controlled growth strategy to obtain narrow size distribution of templating fibers.

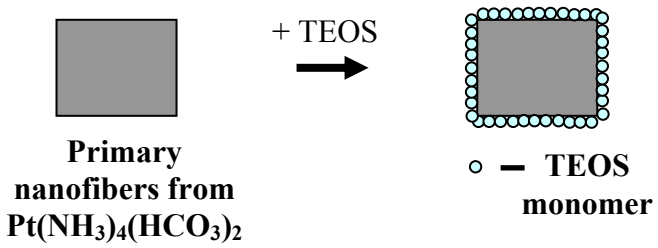


Fig. 4.3 Schematic representation of capping mechanism

A strong electron donor - acceptor interaction (hydrogen bonding) attracts the silica species to adsorb on the Pt salt nuclei or nanofibers as shown in Fig. 4.3. Hence, the aggregation of nanofibers possible through an adsorptive layer of water molecules on the fibres is effectively prohibited. With a suitable supply of building blocks by addition of solvent, the nuclei can only grow in the single direction (c - direction) which is not blocked by the adsorptive layer of silica monomers or oligomers. This silica layer grows simultaneously along the same direction as the crystal. This enhances the anisotropy further. In addition, there is also lateral growth, where the silica layer gets thicker by condensation of silica monomers on it. Eventually, with the one - dimensional growth on the one hand and the lateral layer growth on the other, the high aspect ratio, template - containing NTs result which will be shown in the next sections of this chapter.

## 4.3 Pt – $SiO_2$ NTs

### 4.3.1 Introduction and objective

$SiO_2$ NTs drew special significance due to their remarkable applications in bioanalysis [24], in the storage of environmentally sensitive materials [25] and as optical devices [26]. $SiO_2$ NTs are conventionally synthesized by sol – gel processing in the presence of a template. The various templates reported include anodic aluminium oxide membranes [27], stiff inorganic structures like nanowires of Ag, Si, ZnO or $V_3O_7$ [28], carbon nanotubes [29] or organogelators, surfactants and hydrocarboxylic acids [30, 31].

Chaudhary et al. [32] synthesized $SiO_2$ NTs with Au and Ag particles by hydrothermal method which are expected to have wide range of applications in various catalytic and opto – electronic devices. Also Geng et al. [33] synthesized CdSe – $SiO_2$ NTs by a thermochemistry

method which are expected to be promising for optoelectronic devices. Similarly Qian et al. [34] reported noble metal embedded $SiO_2$ NTs using hybrid fleece as template which are expected to improve the catalytic behaviour of $SiO_2$ NTs.

The present section follows the controlled synthesis strategy as explained in section 4.2 to synthesize Pt – $SiO_2$ NTs using the fibers from $[Pt(NH_3)_4](HCO_3)_2$ salt. Though the morphology of templating crystals from $[Pt(NH_3)_4](HCO_3)_2$ salt seemed identical to the results from L. Ren et al. [35], the size distribution of the tubular structures from Pt – $SiO_2$ NTs reported were narrower when compared to the results from the present study. However, in order to compare to the Pt – $SiO_2$ NTs synthesized from MGS nanofibers which is the primary focus of this thesis, silica nanotubes from $[Pt(NH_3)_4](HCO_3)_2$ salt were prepared under similar reaction conditions and reported in this section.

### 4.3.2 Experimental details

#### (i) Chemical reagents used:

The chemical reagents used in the synthesis of Pt - $SiO_2$ NTs were Platinum tetramine hydrocarbonate ($[Pt(NH_3)_4](HCO_3)_2$, Chempur), Tetraethyl ortho silicate (TEOS) (98%, Aldrich), ethanol (99.9%, Merck), and $H_2O$ (deionised). All the commercial pure reagents were used without any further purification.

#### (ii) Synthesis of Pt – $SiO_2$ NTs

Pt – $SiO_2$ NTs are prepared by varying all the influential reaction parameters. The optimized reaction conditions are presented. Typically, 0.01 g of platinum tetramine hydrogen carbonate ($[Pt\ (NH_3)_4](HCO_3)_2$) salt was immersed in 2 mL of aqueous ammonia solution (0.4 N) at a stirring rate of 300 rpm. The reaction system was maintained at $0^{\circ}C$.

When 2 mL of ethanol was added to the mother solution the transparent solution turned opaque indicating the onset of primary nucleation. After 10 min of stirring in the cold bath, 14 µL of TEOS was added into the reaction system and the stirring was continued for 2 more minutes at the same stirring speed. Then the stirring speed was increased to 1000 rpm and 0.1 mL of ethanol was injected rapidly into the reaction system. The stirring rate was reduced to

300 rpm after 2 min and 10 mL of ethanol was slowly added at a rate of 0.5 mL/min. After aging in the cold bath for 3 h the system was allowed to warm up to room temperature for around 4 h. The resulting product thus obtained was rinsed in water and dried at room temperature overnight. The dried samples were calcined at 350°C for 5 h at a heating rate of 1°C/min in air. The as – prepared and calcined samples were then characterized and the results were illustrated in the next parts of this section.

### 4.3.3 Results and discussion

SEM images of Pt – $SiO_2$ NTs synthesized by controlled strategy mechanism are displayed in Fig. 4.4. The tubes exhibit high aspect ratios (400) and monodispersity as seen in Fig. 4.4 (a). The diameter of the tubes as observed from Fig. 4.4 (b) is around 200 – 800 nm. The tube lengths are around 20 μm long. Few of the nanotubes were also of 1 – 3 μm range comparable to the size distribution of templating crystals from ($[Pt(NH_3)_4](HCO_3)_2$) salt. Unlike the Pt – $SnO_2$ NTs which demonstrated open ends, Pt – $SiO_2$ NTs as seen from the SEM images are mostly close ended. Also, the tubes had rectangular cross – section which could have been inherited from the structure of the commercial salt as shown in Fig. 4.4 (a). The formation of the fibers from $[Pt(NH_3)_4](HCO_3)_2$ salt nanofibres follows a procedure of nucleation and growth.

With the drop wise addition of ethanol, the insoluble Pt salt in the aqueous solution gets concentrated and reaches the supersaturation state with the adequate supply of building

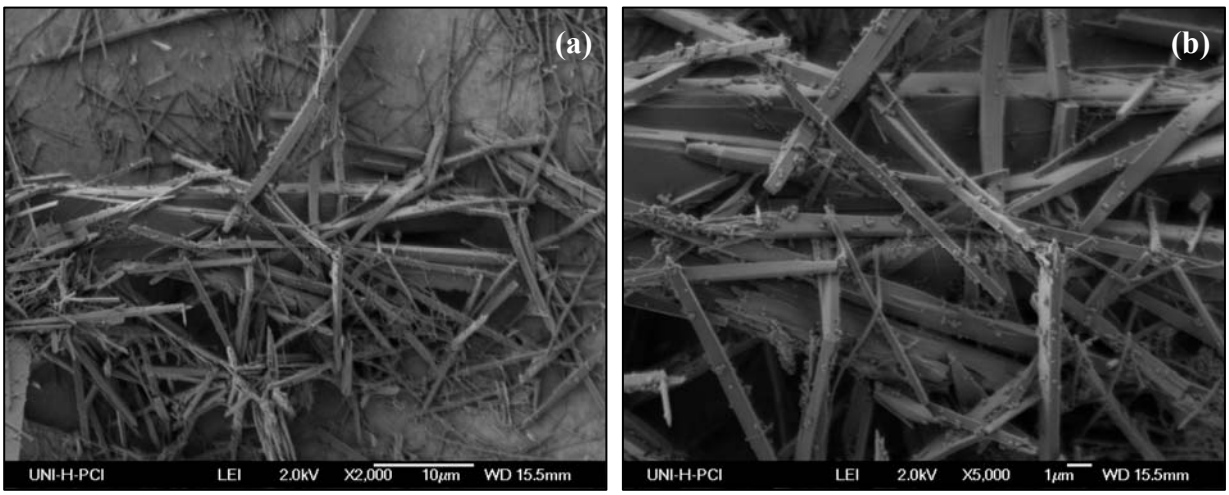


Fig. 4.4 SEM images of Pt – $SiO_2$ NTs showing monodispersity and high aspect ratios at (a) lower magnification (b) higher magnification

blocks. As explained in Chapter 2, when the concentration of building blocks becomes sufficiently high they aggregate into small clusters (nuclei) through a homogeneous nucleation. These nuclei serve as seeds for further anisotropic growth to form intermediate NFs. According to the controlled synthesis strategy uniform, thin and long oxide nanotubes by employing TEOS as capping agent impede the aggregation among intermediate nanofibers.

TEOS when added to the mother solution undergoes intensive hydrolysis. In order to enhance the hydrolysis of TEOS, aqueous $NH_3$ in our system acts as a base catalyst, wherein the silicate monomers deprotonate and adsorb on the facets of nuclei formed from the $Pt(NH_3)_4(HCO_3)_2$ in the mother solution. The precipitated $Pt(NH_3)_4(HCO_3)_2$ nanofibers arange the TEOS monomers via hydrogen bonds. Another possibility could be an exchange of $HCO_3^-$ with silicate anion on the surface of the precipitated templates where the platinum complex cations are expected to connect to the silicate anions via electrostatic interaction. These anchored silicate monomers act as nucleation points while $SiO_2$ walls start to form by a condensation process. Owing to these interactions with the template, a layer of silanol molecules would adsorb on the surface of the template and subsequently the follow - up adsorbates (TEOS monomers) deposit on the first layer and the –Si-O-Si- bonds are formed by rapid condensation. The enrichment of $SiO_2$ on the templating crystals takes place by Ostwald ripening mechanism as explained in chapter 2, which states that the particles gradually grow in size at the walls of the tube and highly soluble silicon dioxide particles re - dissolve in the reaction solution.

The interior structure of the Pt – $SiO_2$ NTs was analyzed by TEM evaluation. Fig. 4.5 shows TEM image of Pt – $SiO_2$ NT calcined at 350°C for 5 h in air at a heating rate of 1°C/min. The image shows that walls of the tube are thick with Pt particles doped inside the tubes whose average diameter was around 50 nm. Metal particles were aggregated most of the times due to the calcination temperature employed. Furthermore from TEM observations it can be observed that the Pt - nanoparticles were highly dispersive on the surface of the tube and Pt particles are closely contacted walls of the tube. Few of the Pt particles outside the tube could be due to the employed calcination temperature that reduced the particles through the porous network of $SiO_2$.

Table 4.1 shows the elemental analysis of single Pt – $SiO_2$ NT where the Pt content with weight percent as much as 37 wt.-%. was observed. Further the EDX analysis confirms the

presence of Pt and Si elements. The value is in accord with the result obtained by L. Ren [6] from the thermal decomposition curves.

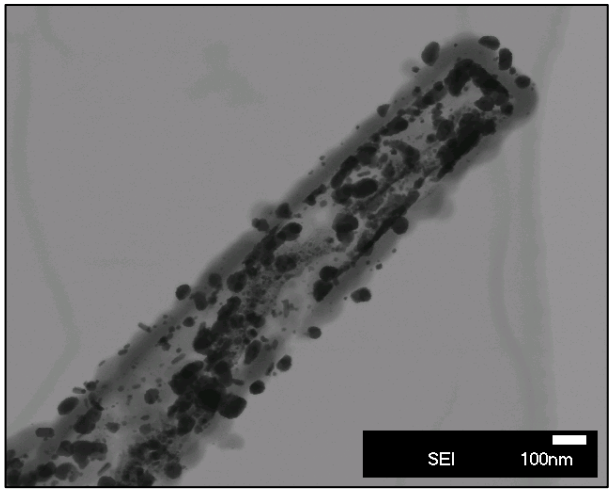


Fig. 4.5 TEM image of a single Pt – $SiO_2$ NT

| **Spectra of single $SiO_2$ NT** | **C** | **O** | **Pt** | **Si** | **Cu** |
|---|---|---|---|---|---|
| **Pt – $SiO_2$ NT (wt. %)** | 8.66 | 14.15 | 36.81 | 9.49 | 30.89 |

Table 4.1 Elemental analysis of a single calcined Pt - $SiO_2$ NT obtained from EDXS

### 4.3.4 Conclusions

From the present study it can be concluded that templating fibers from $Pt(NH_3)_4(HCO_3)_2$ could effectively incorporate into the hollow shells of $SiO_2$ NTs. Pt to as much as 37 wt. % was observed to have loaded inside the tubes. The tubes were monodisperse with lengths around 20 μm long while the diameter is within the range of 200 – 800 nm. Pt - $SiO_2$ NTs are expected to improve the catalytic behaviour of $SiO_2$ catalysts.

## 4.4 Pt – $TiO_2$ NTs

### 4.4.1 Introduction and Objective

Nanostructures of $TiO_2$ attained tremendous attention because of their diverse applications in high performance hydrogen sensors [36, 37], in heterogeneous catalysis [38], in electrocatalysis [39], photocatalysis [40], photocleavage of water [41, 42], gas sensing [43], dye - sensitized solar cells [44], corrosive protective coating and optical coating [45]. $TiO_2$ NTs in particular, acquired considerable interest for their strong oxidizing capability, chemical inertness and non-toxicity [46 - 48].

The groups of Nakahira et al. [49] and Adachi et al. [50] reported that $TiO_2$ NTs by themselves do not exhibit high photocatalytic properties although they have high absorption ability from their high surface area. While, Akita et al. [51] discovered that $TiO_2$ NTs when encapsulated with noble metals demonstrated improved photocatalytic properties. On the other hand, the group of Cabot et al. and others [52] claim that the introduction of catalytic metals such as Au, Pt, Pd and Nb into metal oxides not only amend the sensing performances but also their crystalline structure. This was evident from the research group of Epifani et al. [53] who observed that Pt - $TiO_2$ nanostructures displayed enhanced sensitivity to $H_2$ gas when compared to its pure counterpart. Sato et al. [54] found that the catalytic activity and selectivity for methanol in CO - $H_2$ reaction was extraordinarily high when Pt - $TiO_2$ NTs were used as catalysts. Therefore, metal incorporated $TiO_2$ NTs induce novel functional properties leading to various applications in nanoelectronics and nanodevices. Hence a simplified synthesis approach to prepare metal doped $TiO_2$ NTs has become a quest of research.

From the earlier studies (section 4.3), it was found that Pt – $SiO_2$ NTs gave rise to considerably high yield of tubes with diameter in range of 200 – 800 nm and lengths upto 20 µm when templating fibers from $Pt(NH_3)_4(HCO_3)_2$ salt were used. With a similar intention to synthesize Pt - $TiO_2$ NTs, fibers from $Pt(NH_3)_4(HCO_3)_2$ salt were investigated by varying different reaction parameters. Quite contrary to the results reported [40], synthesis of Pt – $TiO_2$ NTs in the present study exhibited mostly amorphous particles demonstrating the decomposition of templating nanofibers with the coating of various titanium alkoxides. Moreover the controlled mechanistic growth of nanotubes and regulating the reaction

parameters failed to produce impurity free nanotubes. The possible cause behind the redundancy of undesired particles was briefly discussed in the present work.

### 4.4.2 Experimental details

#### (i) Chemicals reagents used

Reagents used in the synthesis of Pt - $TiO_2$ NTs were Platinum tetramine hydrocarbonate ($[Pt(NH_3)_4](HCO_3)_2$, Chempur), Tetrabutyl orthotitanate (TBOT) (p.a., Merck), Titanium isopropoxide (TIP) (97%, Aldrich), Tetraethyl ortho silicate (TEOS) (98%, Aldrich), ethanol (99.9%, Merck), isopropanol (99.9%, Merck) and $H_2O$ (deionised). All the commercial pure reagents were used as obtained.

#### (ii) Synthesis of Pt - $TiO_2$ NTs

Owing to the higher hydrolysis rates of titanium alkoxides, the synthesis of Pt – $TiO_2$ NTs using the fibers from $Pt(NH_3)_4(HCO_3)_2$ salt as template was carried under various reaction conditions with varying reaction parameters. Two different alkoxides were used to coat the fibers from $Pt(NH_3)_4(HCO_3)_2$ salt. Sample $TiO_2$ – 1 and sample $TiO_2$ – 2 were prepared under similar reaction conditions and compared.

In a typical experiment, 0.01 g of platinum tetramine hydrogen carbonate ($[Pt(NH_3)_4](HCO_3)_2$) salt was dispersed in 2 mL of aqueous ammonia solution (0.4 N) at a stirring rate of 300 rpm. The reaction system was placed in a bath maintained at - 20 $^{\circ}$C. The clear solution turned murky with the addition of 2 mL of ethanol. After 10 min of stirring in the cold bath, 14 μL of TEOS was added into the reaction system and the stirring was continued for 2 more minutes at the same stirring speed. 88 μL of pre – cooled TBOT (for sample $TiO_2$ – 1) was added drop - wise into the mother solution. After 2 min, the stirring speed was increased to 1000 rpm and 0.1 mL of ethanol was injected rapidly into the reaction system. The stirring rate was reduced to 300 rpm after 2 min and 10 mL of ethanol was slowly added at a rate of 0.5 mL/min. After aging in the cold bath for 3 h the system was allowed to warm up to room temperature (≈ 4 h). The resulting product was washed with water several times and dried at room temperature. The dried samples were sintered at a temperature of 250$^{\circ}$C for 6 h at a heating rate of 1$^{\circ}$C/min in air.

In case of sample $TiO_2$ – 2, 132 µL of pre – cooled TIP was added and isopropanol was used as solvent while the rest of the synthesis was performed under similar conditions as sample $TiO_2$ – 1.

### 4.4.3 Results and discussion

#### (i) Characterization using SEM technique

The amorphous structures from as – synthesized samples $TiO_2$ -1 and $TiO_2$ – 2 are revealed by SEM in Fig. 4.6. Both the samples illustrated nanoparticles with no fibers from $Pt(NH_3)_4(HCO_3)_2$ salt contrary to Pt – $SiO_2$ NTs. The particles could be from the alkoxides in the solution which could not coat the template fibers. The condensation rates of TBOT and TIP were controlled by maintaining the temperature of the reaction bath at -20°C. When temperature was reduced further to -30°C similar results were yielded. The formation of particles could have been from the $TiO_2$ or $H_3TiO_7$ fragments that usually result in presence of large amount of water originating from the metal alkoxides.

When TBOT/TIP was added prior to the addition of solvent it could have been that the primary nuclei from the first addition of solvent in the aqueous solution could have dispersed into the coating matrix of $TiO_2$. When the fibers are dispersed into the matrix the anisotropic growth is hindered thereby resulting in the formation of nanoparticles. Though drying stresses could also be considered, the presence of TEOS as capping agent is expected to protect the fibers/particles from stress that develop with the evaporation of the solvent.

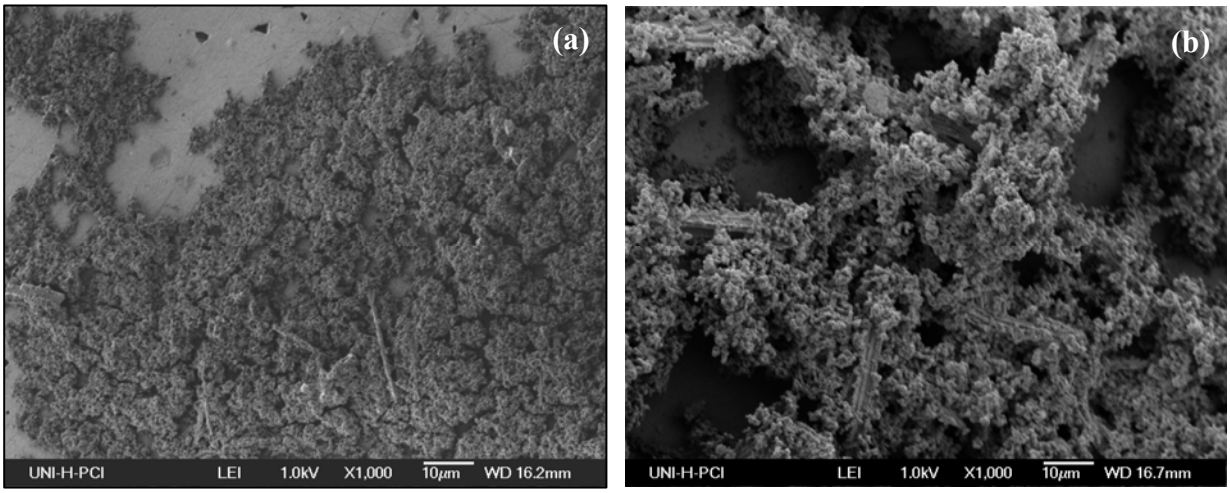


Fig. 4.6 SEM images of as – synthesized samples of sample (a) $TiO_2$ -1 and (b) $TiO_2$ - 2

Conversely the results reported from L.Ren [10] and Y. Sato et al [54] could effectively synthesize one dimensional Pt – $TiO_2$ NTs using the templating fibers from $Pt(NH_3)_4(HCO_3)_2$ salt. Stabilizers to reduce the hydrolysis and condensation rates of titanium alkoxide were employed in either of the studies. On comparing the results from the present study, it could be inferred that higher hydrolysis rates of alkoxide could be the reason for the formation of amorphous nanostructures. Hence in the synthesis of Pt – $TiO_2$ NTs from MGS, stabilized TIP was used to coat the fibers which resulted in the formation of impurity free, highly crystalline titania nanotubes which is elucidated in detail in section 5.4.

**(ii) Characterization with TEM**

Fig. 4.7 represents the TEM image from calcined sample $TiO_2$ -2. The TEM studies depict the presence of Pt particles with diameter around 10 - 50 nm. No traces of titanium element were observed from the EDX analysis (not shown). It could be that the $TiO_2$ particles would have been left out in the solution fraction while the TEM analysis was performed from the dried sample suspension.

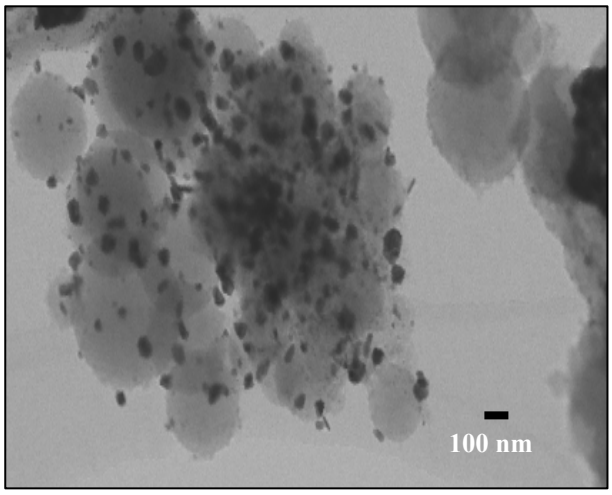


Fig. 4.7 TEM image of sample $TiO_2$ -2

### 4.4.4 Conclusions

The results from Pt – $TiO_2$ NTs synthesized from $Pt(NH_3)_4(HCO_3)_2$ salt indicate that the presence of stabilizers to control the hydrolysis and condensation rates of titanium alkoxide greatly influence the crystallinity of the samples.

## 4.5 Pt – $SnO_2$ NTs

### 4.5.1 Introduction

Stannic oxide ($SnO_2$) gained particular attention because of its large band gap (3.6 eV) which makes it transparent to the visible light of the electromagnetic spectrum and consequently finds its potential applications as transparent electrodes for solar cells [55], photoconductors [56] and acts as anode in lithium ion batteries [57]. Furthermore, this n-type semiconductor because of its existing oxygen vacancies in the lattice lets the electrons localized in states whose energies are close to the conduction band and function as n type donors [58]. This leads to the considerable increase in the conductivity of the oxide. Moreover, the atoms or molecules interacting with the surface of the oxide adsorb on these vacancy sites thus making this semiconducting oxide an effective gas sensor to detect gases such as $H_2S$, CO, $NO_2$ etc. [59 - 63].

The conductivity of the n - type semiconducting oxides is altered by the adsorption or the desorption of the oxidizing gas species and the surrounding space charge effects. Therefore, changes in the surface of the oxide layer can vary the sensor response considerably. Sauvan et al. [64] reported that the sensing properties of metal oxides can be enhanced by addition of noble metals to the active layer. Bittencourt et al. [65] reported that Pt loaded $SnO_2$ material showed high sensitivity and fast response to ethanol compared to pure $SnO_2$ material. F. Morazzoni et al. [66] presented in their work that doped metal centers aggravated the electron trapping which in turn increased the electrical resistance of Pt doped $SnO_2$ films when compared to the un - doped $SnO_2$ films in detecting CO gas. The co-workers of A. Dieguez et al. and others [67 – 69] claimed that the presence of metals (such as Pt or Pd) allows for a significant decrease in the operating temperature of the sensors, the enhancement of sensitivity to different gases and reduces response time.

Hence it opens perspective for developing a facile approach to synthesize noble - metal doped $SnO_2$ materials. In this section, Pt - $SnO_2$ NTs by a cost effective sol - gel technique using $[Pt(NH_3)_4](HCO_3)_2$) fibers as templating structures was explicitly described. The strategy for controlled growth synthesis of Pt - $SnO_2$ NTs together with the influence of capping agent in the synthesis approach followed by the morphology dependence on varying synthesis conditions was elucidated with experimental evidence. Crystalline Pt - $SnO_2$ NTs with

diameters in the broad range of 200 - 800 nm and lengths ranging between 2 and 5 μm with a high incorporation of as much as 38 - 40 wt.- % of Pt inside the tubes were observed from the present study.

### 4.5.2 Experimental section

#### (i) Chemical reagents used

Tin isopropoxide ($[Sn(O^iPr)_4]$, $^iPrOH$, ABCR), TEOS (tetraethyl ortho silicate) (98%, Aldrich), $[Pt(NH_3)_4](HCO_3)_2$ (Chempur), Isopropanol (99.9%, Merck), $H_2O$ (deionised). All the reagents were used as supplied without further purification. For the preparation of 0.4 N ammonia solution (pH = 10 - 11, 20 °C), 5.6 g of saturated ammonia solution (25 %, Merck) was diluted with 100 mL of distilled water.

#### (ii) Synthesis procedure of Pt - $SnO_2$ NTs

In a typical synthesis, 0.11 g of tin isopropoxide ($[Sn(O^iPr)4]$), was dropped in 30 mL of absolute isopropanol and the mixture was heated to 100°C under constant stirring for 1 h. The mixture was cooled down to room temperature and then placed in a cold bath (- 30°C) for around 45 min.

At a stirring rate of 300 rpm, 0.02 g of platinum tetramine hydrogen carbonate ($[Pt(NH_3)_4](HCO_3)_2$) salt was dissolved in 2 mL of aqueous ammonia solution (0.4 N) and placed in a bath maintained at - 30 °C. The transparent solution turned opaque with the addition of 2 mL of isopropanol. Followed by 10 min of stirring in the cold bath, 14 μL of TEOS was added into the reaction system and the stirring was continued for 2 min at the same stirring speed. Later, the tin isopropoxide mixture was added drop - wise into the mother solution. After 2 min of continuous stirring, the stirring speed was increased to 1000 rpm and 0.1 mL of isopropanol was injected rapidly. The stirring rate was reduced to 300 rpm after 2 min and 10 mL of isopropanol was added at a rate of 0.5 mL/min. The reaction system was aged in the cold bath for 3 h and then allowed to warm up to room temperature for 4 h. The resulting product was washed with water several times and dried at room temperature.

The dried samples were calcined at 250°C for 6 h at a heating rate of 1°C/min in a stream of $H_2$ gas. In order to study the influence of calcination temperature, the dried samples were also sintered at 300°C under same calcination conditions and compared.

### 4.5.3 Results and discussion

#### (i) Characterization with Electron Microscopy

Fig. 4.8 portrays the morphology of as - synthesized products of Pt - $SnO_2$ NTs obtained from the optimized conditions of the reaction parameters. The SEM images shown in Fig. 4.8(a) and 4.8(b) depict nanotubes with a clear surface at lower and higher magnifications respectively. Each nanotube exhibited uniform width along its entire length. The mean length of the nanotubes was ≈ 3 μm (Fig. 4.8 (a)). Contrary to the result from tube lengths of Pt – $SiO_2$ NTs (section 4.3), it can be observed that Pt – $SnO_2$ NTs are shorter. This distinct feature arising from the short length was further inspected by collecting the samples at intermediate growth times of 3, 5, 7, 9, 12, 15, 20 and 24 hours. The fitted lengths of the nanotubes obtained from SEM imaging as function of synthesis time are shown in Fig. 4.9. The error bars on the fitted lengths were obtained by averaging the results from five independent samples taken in different experiments. From the analysis it can be inferred that there does not appear a physically significant change in length of the nanotube with the increase in the synthesis time. Minute increase in fitted lengths could be due to the aggregation of nanotubes at higher concentrations. The constant length of the nanotubes throughout the synthesis time (over 24 hours) appears to favor a self - assembly mechanism over a kinetic mechanism which rather involves the formation of 'proto- nanotube' intermediates which increase in length by addition of precursors as discussed in chapter 2 (section 2.1.5).

The diameter distribution of Pt - $SnO_2$ NTs was shown in Fig. 4.10. It can be seen from the histogram plot that the maximum of diameter distribution occurred in the range of 200 - 800 nm. In contrast to the length of the tube, the diameter distribution seems to favor the kinetic mechanism in conjunction with the capping effect. Peng et al. [70] discuss two distribution modes for the growth rate of particles depending upon the concentration of monomer present namely 'focusing' of the size distribution and 'defocusing'. When the concentration of the monomers is higher than the solubility of the particles then the particles grow irrespective of the size. At such a high monomer concentration, the smaller particles grow faster than the

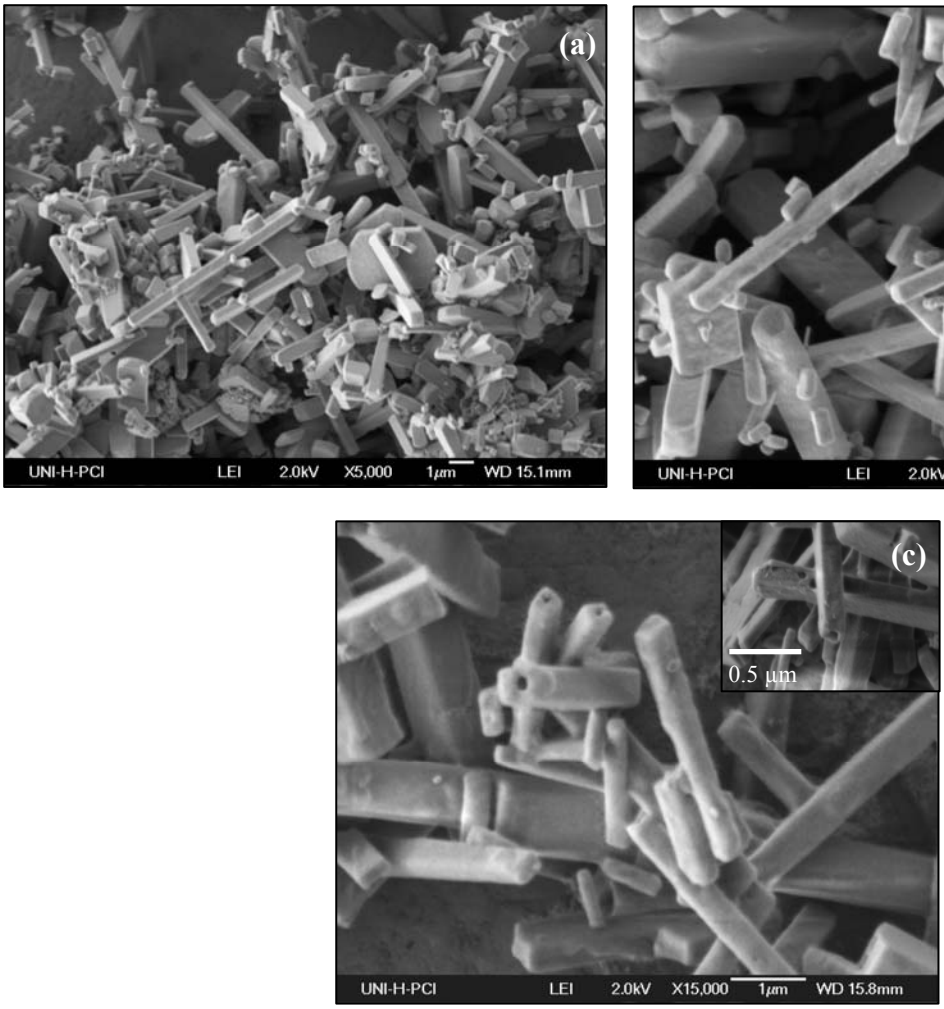


Fig. 4.8 SEM images of Pt - $SnO_2$ nanotubes (a) at low magnification (b) at higher magnification depicting the size distribution in the range of 200 – 800 nm (c) with a high resolution view illustrating open ended nanotubes

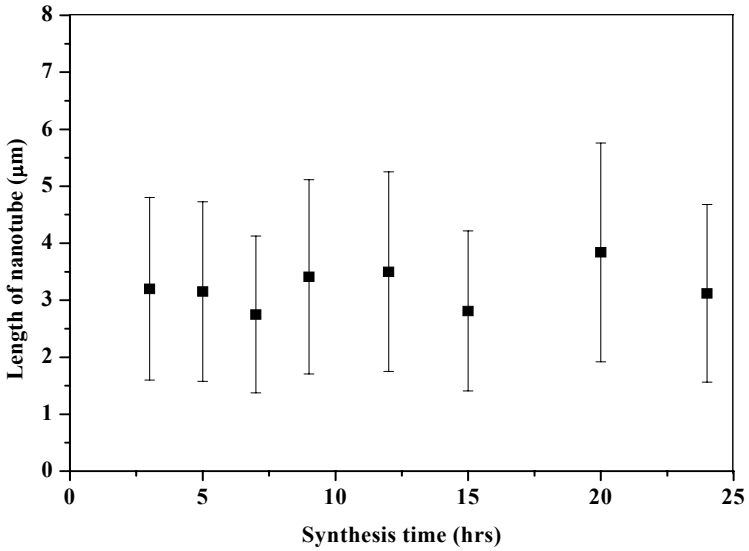


Fig. 4.9 Fitted lengths of Pt - $SnO_2$ NTs obtained from SEM images as function of synthesis time

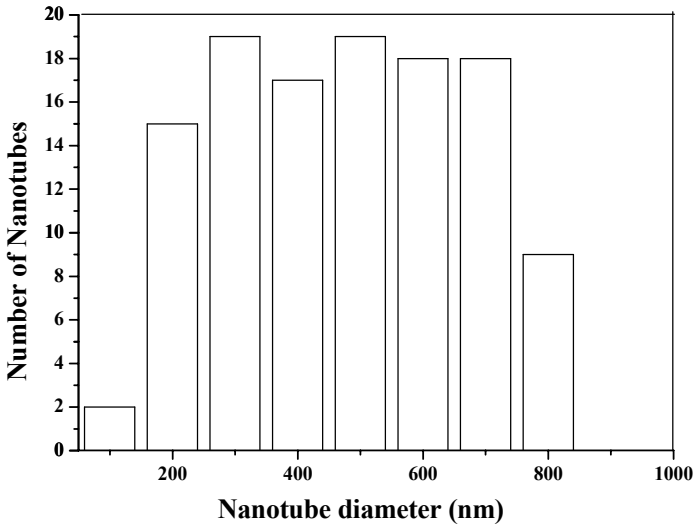


Figure 4.10 Histogram of Pt – $SnO_2$ NTs with diameter distribution

larger ones resulting in a size distribution that can be focused down to one that is nearly monodisperse. On the other hand, when the monomer concentration drops lower than the critical threshold, small nanocrystals are depleted as larger ones grow. Consequently, the distribution widens or defocuses. In accordance to the above interpretation, initially when the concentration of the nuclei was higher, a narrow distribution could have been established while the size eventually broadened as the concentration became lower leading to a wide range of diameter distribution (200 – 800 nm).

As explained in section 4.2.3, the fortuitous presence of capping agents hampers the aggregation of primary nanofibers. Hence, the capping agent (TEOS in the present case) was added prior to tin alkoxide in the reaction mixture which is likely to bind relatively stronger to the facets of nuclei formed from the $Pt(NH_3)_4(HCO_3)_2$ salt in the mother solution. However, when the availability of monomers in the solution is high, the particles grow too fast not giving enough time for the deposition of capping agent on the new surface of the particles leading to aggregation. This could also be a cause for the formation of large size distribution of nanotubes.

The cross - sectional view of the nanotubes examined at higher magnifications was shown in Figure 4.8 (c). Apparently, the tubular nanostructures had rectangular cross section while few of them revealed open ends. The opening of the tube ends in few of the nanotubes could be correlated to the hollow opening observed in some of the template crystals (section 4.2 (Fig. 4.4 (b)). Moreover, the deposition of TEOS on the ends is relatively difficult because of the

continuous growing of the corresponding facet. Further, the inset from Fig. 4.8 (c) portrays thick walls of the tubes with width around 50 nm. The thick walls of the tube can be attributed to the presence of silanol molecules and subsequently the hydroxyl groups of tin isopropoxide that adsorb on the surface of the template nanofibers during condensation.

Besides acting as a capping agent, TEOS in our study, served as a protective layer for the Pt nanofibers avoiding their deformation at higher temperatures and as a reactant supporting the formation of Pt – $SnO_2$ NTs free of Pt - Sn alloys while the latter will be elaborated in the next parts of this section. The Pt - $SnO_2$ NTs were calcined at an optimum temperature of 280° C and the even distribution of Pt particles along the tube as seen from the bright field image of TEM in Fig. 4.11 (a) indicate the effective decomposition of Pt template. The high electron scattering potential of Pt makes it appear in dark contrast when focussed under selected imaging conditions. The core of the tube was filled with plenty of Pt particles with diameter in the range of 10 – 30 nm. However the concentration of Pt particles was relatively lower along the tube walls. The TEM image is consistent with the SEM images confirming the tubular morphology of the NTs. Unlike the open ends of the nanotubes observed in SEM imaging, most of the TEM images displayed tubes with closed ending. Hence there arises no risk of losing the Pt particles to the exterior part of the tube.

In order to study the influence of capping agent in the reaction mixture during calcination, a sample was prepared without the addition of TEOS and calcined, however at a slightly higher temperature of 300°C under similar conditions. Most of the tubes lost their morphology and decomposed into amorphous materials.

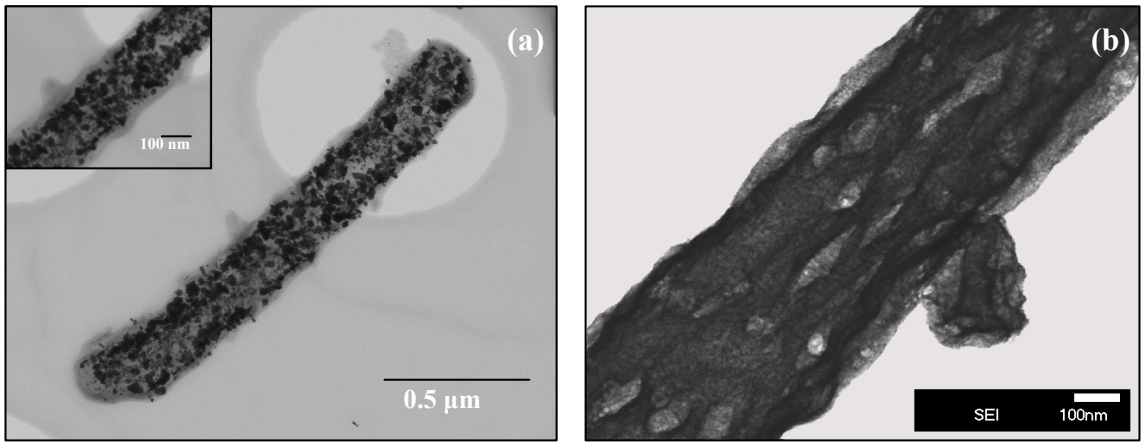


Fig. 4.11 TEM images of Pt - $SnO_2$ NTs (a) calcined at 280°C in presence of TEOS (b) calcined at 300°C in absence of TEOS

Fig. 4.11 (b) displays TEM image of a nanotube calcined at 300°C in absence of TEOS. The tube was distorted losing its uniformity demonstrating that the addition of TEOS is vital in the reaction mixture not only to hinder the aggregation of primary nanofibers from $Pt(NH_3)_4(HCO_3)_2$ salt but also to enhance the strength of the gel structure and to increase its resistance to the thermal stress. The thermal decomposition of Pt – $SnO_2$ NTs was further studied by thermogravimetric analysis (TGA) described in the subsequent part of this section.

**(ii) Thermogravimetric Analysis (TGA)**

The thermal behaviour of Pt - $SnO_2$ NTs has been investigated by TGA analysis as shown in Fig. 4.12. The heating rate was maintained at 1°C/min in $H_2$ gas atmosphere for comparing with the calcination conditions employed. A closer inspection into the TGA curve exhibits distinctive weight loss in two steps. The loss in mass seems to initiate at 50 °C prolonging until 150°C and then becoming acute in the range of 200 – 250 °C. Thereafter the weight loss became less intense without showing any significant weight loss pointing out the complete decomposition of the template. The lower weight loss until 150 °C could be from desorption of the residual water from the micropores. The weight loss from 190 - 250 °C depicts the complete removal of template and dehydration of hydroxyl groups. The weight loss of commercial $Pt(NH_3)_4(HCO_3)_2$ salt from earlier work [19] further ensures the removal of template in the temperature range of 200 – 250°C.

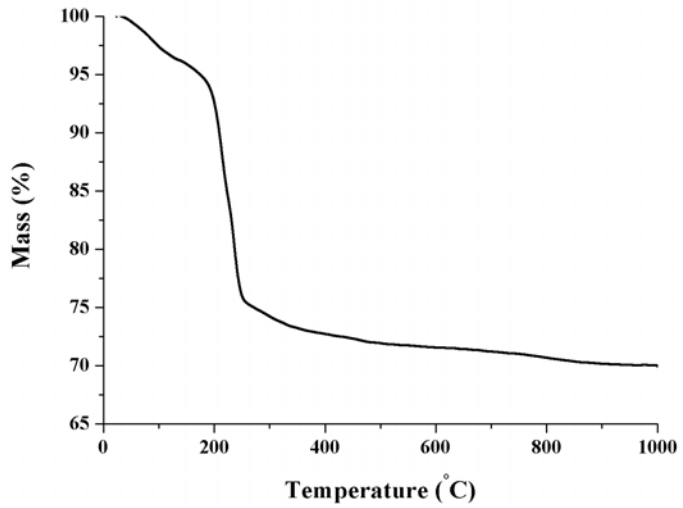


Fig. 4.12 Thermogravimetric curve of Pt - $SnO_2$ NTs

The Pt template during the heat treatment decomposes according to the reaction shown in (4.1).

$$[Pt(NH_3)_4(HCO_3)_2] \rightarrow Pt + 2N_2 + 5H_2 + 2CO_2 + 2H_2O \quad (4.1)$$

The gases such as $N_2$, $H_2$, $CO_2$, water vapor and $NH_3$ that release during decomposition escape through the porous walls of the tube. Under the reducing atmosphere ($H_2$), the diffusion of Pt metal particles through the walls is generally noticed. However in our present study the walls of the tubes were scarcely seen with Pt particles (inset of Figure 4.11 (a)) because of the lower calcination temperature.

The quantitative analysis from the TGA measurements reveal that the weight loss of Pt - $SnO_2$ NTs is approximately 25 wt.-%. Acute weight loss observed in the range of 190 – 250°C is about 18 wt.-%. The weight loss of commercial salt from our studies showed a mass loss of 45 wt.-% [15]. This value is in close agreement with the actual decomposition of $NH_3$, $CO_2$ and $H_2O$ from the Pt–salt nanofibers, since 47.4 wt.-% of the mass of the Pt salt results from metal Pt. Comparing to the weight loss of Pt salt, it can be deduced that about 40 wt.-% of Pt particles were embedded inside $SnO_2$ NTs.

**(iii) Characterization with X - ray diffractometry**

Though the expected role of Sn lies in modifying Pt by interacting with $Sn^{2+}$ions, as described by Kuznetsov et al. [71], Sn is more susceptible to form alloys with Pt and partly to ionic $Sn^{2+}$or $Sn^{4+}$ and as $Sn^0$. Hence the XRD patterns from the present work were scrutinized to gain insight into the internal structure of Pt – $SnO_2$ NTs. The study discloses the diffraction patterns of Pt – $SnO_2$ NTs that were synthesized with and without TEOS and the interaction of Sn with Pt were studied.

As illustrated in Fig. 4.13 (a), it can be understood that, with absence of TEOS, XRD patterns illustrated four phases indicating the formation of alloys $Pt_3Sn$, PtSn, $PtSn_3$ and metallic platinum with insignificant traces of $SnO_2$ peaks. The peaks were compared to the values reported in the respective works. Peaks at 2Θ = 26.0, 30.0, 33.9, 42.08, 44.4, 51.4, 54.6, 62.5 correspond to PtSn alloy (JCPDS No 25-614) while peaks at 2Θ = 38.8, 45.4, 65.9 correspond

to $Pt_3Sn$ alloy (JCPDS No 35-1360) and peaks at 2Θ = 27.9, 29.8, 34.4, 61.7, 69.0 with very low intensity correspond to $PtSn_3$ alloy (JCPDS No 37-1197).

The influence of TEOS was studied by preparing Pt – $SnO_2$ NTs with the presence of TEOS. The resultant peaks were shown in Fig. 4.13 (b). The peaks at 2Θ = 11.1 and 16.2 correspond to the peaks from the templating Pt metal nanofibers that fit well with those reported by L.Ren et al.[19]. However with TEOS in the reaction mixture, no such alloys were observed but two well resolved phases with peaks at 2Θ = 26.5, 33.9, 51.7 corresponding to the

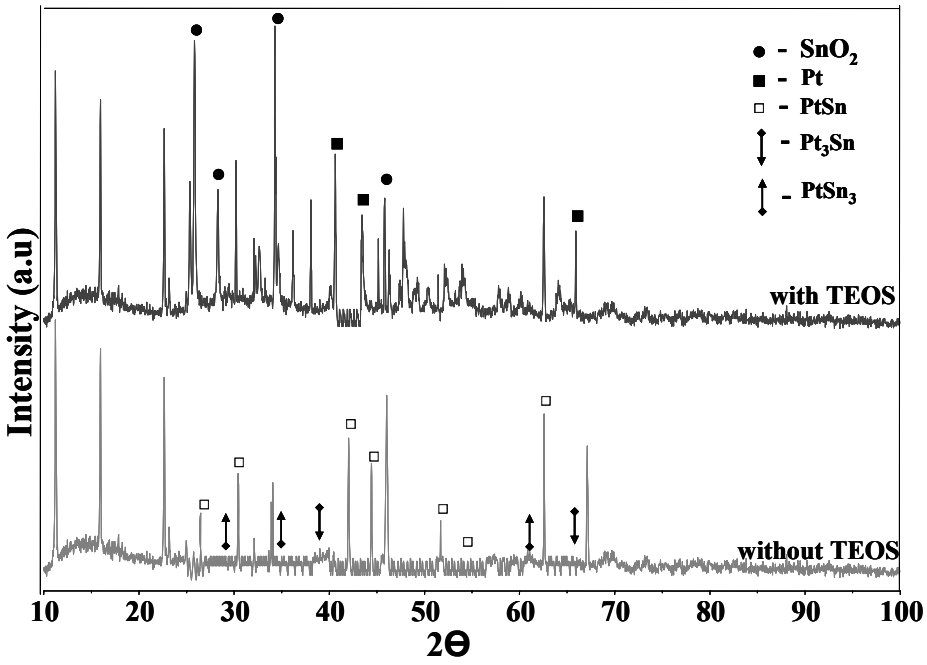


Figure 4.13 XRD patterns of Pt - $SnO_2$ NTs (a) without TEOS (b) with TEOS

$SnO_2$ phase (JCPDS No 21-1250) and that of metallic Pt were recognized.The formations of distinct phases of $SnO_2$ and Pt in the presence of TEOS without the formation of the possible alloys could be because of the presence of amorphous $SiO_2$ layer around the platinum which might impede the interaction of Pt with Sn.

### 4.5.4 Conclusions

From the experimental investigation it can be concluded that Pt – $SnO_2$ NTs in presence of TEOS disclosed distinct peaks of $SnO_2$ as well as metallic Pt with no formation of alloys. Moreover the TGA results show that Pt to as much as 40 wt.-% could be doped inside $SnO_2$

NTs at much lower temperatures. Such a high Pt loading is likely to enhance the sensing properties of the material thereby reducing the response time.

### 4.6 References

[1] Y. H. Gao, Y. Bando, *Nature,* **415** (2002) 599.

[2] Y. B. Li, Y. Bando, D. Golberg, *Advanced Materials*, **16** (2004) 37.

[3] C. Liang, Y. Shimizu, T. Sasaki, H. Umeharab, N. Koshizaki, *Journal of Materials Chemistry*, **14** (2004) 248.

[4] J. X. Wang, L. X. Wen, Z. H. Wang, J. F. Chen, *Materials Chemistry and Physics*, **96** (2006) 90.

[5] G. Grubert, J. Rathousky, G. Schulz – Ekloff, M. Wark, A. Zukal, *Microporous Mesoporous Materials,* **22** (1998) 225.

[6] E. Dujardin, T.W. Ebbesen, H. Hiura, K. Tanigaki, *Science,* **265** (1994) 1850.

[7] Y. Li, C. H. Ye, X. S. Fang, L. Yang, Y. H: Xiao, L. D. Zhang, *Nanotechnology,* **16** (2005) 501.

[8] Y. B. Lim, Y. S. Bando, D. Goldberg, *Advanced Materials,* **15** (2003) 581.

[9] G. R. Patzke, F. Krumeich, R. Nesper, *Angewandte Chemie International Edition,* **41** (2002) 2446 and references therein.

[10] L. Ren, 'Inorganic salt nanofibers as templates for the formation of oxide nanotubes' *Ph.D Thesis*, Leibniz University of Hannover, 2004.

[11] C. Bae, H. Yoo, S. Kim, K. Lee, J. Kim, M. M. Sung, H. Shin, *Chemistry of Materials,* **20** (2008) 756.

[12] M. Volel, M. Armand, W. Gorecki, M. L. Saboungi, *Chemistry of Materials,* **17** (2005) 2028.

[13] G. An, Y. Zhang, Z. Liu, Z. Miao, B. Han, S. Miao, J. Li, *Nanotechnology,* **19** (2008) 035504.

[14] H. -P. Lin, C. -Y. Mou, S. -B. Liu, *Advanced Materials,* **12** (2000) 103.

[15] F. Krumeich, H. -J. Muhr, M. Niederberger, F. Bieri, R. Nesper, *Journal of American Chemical Society,* **121** (1999) 8324.

[16] Y. Sun, B. Mayers, Y. Xia, *Advanced Materials,* **15** (2003) 641.

[17] H. Nakamura, Y. Matsui, *Journal of the American Chemical Society,* **117** (1995) 2651.

[18] F. Krumeich, M. Wark, L. Ren, H. -J. Muhr, R. Nesper, *Zeitschrift für Anorganische und Allgemeine Chemie,* **630** (2004) 1054.

[19] L. Ren, M. Wark, *Chemistry of Materials,* **17** (2005) 5928.

[20] C. Hippe, M. Wark, E. Lork, G. Schulz - Ekloff, *Microporous Mesoporous Materials,* **31** (1999) 235.

[21] W. Noll, *Zeitschrift für Anorganische und Allgemeine Chemie,* **261** (1950) 1.

[22] Y. Xia, P. Yang, Y. Sun, Y. Wu, B. Mayers, B. Gates, Y. Yin, F. Kim, H. Yan, *Advanced Materials,* **15** (2003) 353.

[23] N. Jongen, P. Bowen, J. Lemaitre,J. Valmalette, H. Hofmann, *Journal of Colloid and Interface Science,* **226** (2000) 189.

[24] S. B. Lee, D. T. Mitchell, L.Trofin, T. K. Nevanen, H. Söderlund, C. R: Martin, *Science,* **296** (2002) 2198 ; *Journal of the American Chemical Society,* **124** (2002) 11864.

[25] M. Zhang, Y. Bando, K. Wada, L. L. Cend, P. Pirouz, *Applied Physics Letters*, **80** (2002) 491.

[26] K. Okamoto, C. J. Shook, L. Bivona, S. B. lee, D. S. English, *Nano Letters,* **4** (2004) 233.

[27] N. I. Kovtyukhova, T. E. Mallouk, T. S. Mayer, *Advanced Materials,* **15** (2003) 780.

[28] G. R. Patzke, F. Krumeich, R. Nesper, *Angewandte Chemical International Edition,* **41** (2002) 2446.

[29] B. C. Satishkumar, A. Govindaraj, E. M. Vogl, L. Basumallick, C. N. R. Rao, *Journal of Maerials Research,* **12** (1997) 604.

[30] J. H. Jung, S. Shinkai, T. Shimizu, *Chemistry of Materials,* **15** (2003) 2141.

[31] L. Wang, S. Tomura, F. Ohashi, M. Maeda, M. Suzuki, K. Inumai, *Journal of Materials Chemistry,* **11** (2001) 1465.

[32] Y. S. Chaudhary, J. Ghatak, U. M. Bhattab, D. Khushalani, *Journal of Materials Chemistry*, **16** (2006) 3619.

[33] B. Geng, G. Meng, L. Zhang, G. Wang, X. Peng, *Chemical Communications*, **5** (2003) 2572.

[34] H. S. Qian, M. Antoniette, S. H. Yu, *Advanced Functional Materials*, **17** (2007) 637.

[35] L. Ren, *Ph. D Dissertation*, Leibniz University of Hannover, 2004.

[36] G. K. Mor, M. A. Carvalho, O. K. Varghese, M. V. Pishko, C. A. Grimes, *Journal of Materials Research,* **19** (2004) 628.

[37] O. K. Varghese, D. W. Gong, M. Paulose, K. G. Ong, C. A. Grimes, *Sensors and Actuators B,* **93** (2003) 338.

[38] B. F. G. Johnson, *Topics in Catalysis,* **24** (2003) 147.

[39] J. Qu, X. Zhang, Y. Wang, C. Xie, *Electrochimica Acta*, **50** (2005) 3576.

[40] S. P. Albu, A. Ghicov, J.M. Macak, P. Schmuki, *Nano Letters,* **7** (2007) 1286.

[41] C. Ruan, M. Paulose, O. K. Varghese, G. K. Mor, C. A. Grimes, *Journal of Physical Chemistry B,* **109** (2005) 15754.

[42] K. Shankar, G. K.Mor, H. E. Prakasam, S. Yoriya, M. Paulose, O. K. Varghese, C. A. Grimes, *Nanotechnology,* **18** (2007) 065707.

[43] O. K. Varghese, D. W. Gong, M. Paulose, K. O. Ong, E. C. Dickey, C. A. Grimes, *Advanced Materials,* **15** (2003) 624.

[44] M. Adachi, Y. Murata, I. Okada, S. Yoshikawa, *Journal of the Electrochemical Society,* **150** (2003) G488.

[45] G. Guisbiers, O. Van Overschelde, M. Wautelet, *Applied Physics Letters,* **92** (2008) 103121.

[46] K. Shimizu, H. Imai, H. Hirashima, K. Tsukuma, *Thin Solid Films,* **351** (1999) 220.

[47] H. Imai, M. Matsuda, K. Shimizu, H. Hirashima, N. Negishi, *Journal of Materials Chemistry,* **10** (2000) 2005.

[48] T. Kasuga, M. Hiramatsu, A. Hoson, T. Sekino, K. Niihara, *Langmuir,* **14** (1998) 3160.

[49] A. Nakahira, W. Kato, M. Tamai, T. Isshiki, K. Nishio, H. Aritani, *Journal of Materials Science,* **39** (2004) 4239.

[50] M. Adachi, Y. Murata, M. Harada, S. Yoshikawa, *Chemistry of Letters,* **29** (2000) 942.

[51] T. Akita, M. Okumura, K. Tanaka, K. Ohkuma, M. Kohyama, T. Koyanagi, M. Date, S. Tsubota, M. Haruta, *Surface Interface Analysis,* **37** (2005) 265.

[52] (a) A. Cabot, J. Arbiol, J. R. Morante, U. Weimar, N. Bársan, W. Göpel, *Sensors and Actuators B,* **70** (2000) 87 (b) J. Arbiol, A. Cirera, F. Peiró, A. Cornet, J. R. Morante, J. J. Delgado, J. J. Calvino, *Applied Physics Letters,* **80** (2002) 329 (c) A. Ruiz, J. Arbiol, A. Cirera, A. Cornet, J. R. Morante, *Materials Science and Engineering C,* **19** (2002) 105 (d) J. Arbiol, J. Cerd`a, G. Dezanneau, A. Cirera, F. Peir´o, A. Cornet, J. R. Morante, *Journal of Applied Physics,* **92** (2002) 853.

[53] M. Epifani, A. Helwig, J. Arbiol, R. D´ıaz, L. Francioso, P. Siciliano, G. Mueller, J. R. Morante, *Sensors and Actuators B,* **130** (2008) 599.

[54] Y. Sato, M. Koizumi, T. Miyao, S. Naito, *Catalysis Today,* **111** (2006) 164.

[55] M. Okuya, S. Kaneko, *Journal of the European Ceramic Society,* **21** (2001) 2099.

[56] S. Mathur, S. Barth, H. Shen, J. C. Pyun, U. Werner, *Small,* **1** (2005) 713.

[57] B. Liu, H. C. Zeng, *Journal of Physical Chemistry B,* **108** (2004) 5867.

[58] V. E. Henrich, P. A. Cox, *Surface Science of Metal Oxides*; Cambridge University Press: Cambridge, England, 1996.

[59] W. Gopel, *Microelectronic Engineering,* **32** (1996) 75.

[60] D. Kohl, *Journal of Physics D: Applied Physics,* **34** (2001) R125.

[61] P. T. Moseley, *Measurement Science and Technology,* **8** (1997) 223.

[62] G. Sberveglieri, *Sensors and Actuators B: Chemical,* **23** (1995) 103.

[63] J. Liu, X. Huang, G. Ye, W. Liu, Z. Jiao, W. Chao, Z. Zhou, Z. Yu, *Sensors,* **3** (2003) 110.

[64] M. Sauvan, C. Pijolat, *Sensors and Actuators B: Chemical,* **58** (1999) 295.

[65] C. Bittencourt, E. Llobet, P. Ivanov, X. Correig, X. Vilanova ,J. Brezmes, J. Hubalek, K. Malysz, J. J. Pireaux, J. Calderer, *Sensors and Actuators B: Chemical,* **97** (2004) 67.

[66] F. Morazzoni, C. Canevali, N. Chiodini, C. Mari, R. Ruffo, R. Scotti, L. Armelao, E. Tondello, L. E. Depero, E. Bontempi, *Chemistry of Materials,* **13** (2001) 4355.

[67] A. Diéguez, A. Vilà, A. Cabot, A. Romano - Rodrıguez, J. R. Morante,J. Kappler, N. Barsan, U. Weimar, W. Göpel, *Sensors and Actuators B: Chemical,* **68** (2000) 94.

[68] K. D. Schierbaum, J. Geiger, U.Weimar,W. Göpel, *Sensors and Actuators B: Chemical,* **13** (1993) 143.

[69] A. Heilig, N. Barsan, U. Weimar, W. Göpel, *Sensors and Actuators B: Chemical,* **58** (1999) 302.

[70] X. G. Peng, J. Wickham, A. P. Alivisatos, *Journal of the American Chemical Society,* **120** (1998) 5343.

[71] V. I. Kuznetsov, A. S. Belyi, E.N. Yurchenko, M. D. Smolikov, M. T. Protasova, E. V. Zatolokina, V. K. Duplyakin, *Journal of Catalysis,* **99** (1986) 159.

# 5

# 5. Formation of Pt incorporated metal oxide nanotubes using Magnus green salt fibers as templating structures

## 5.1 Introduction and objective

As described in chapter 4, Pt incorporated oxide nanotubes improve the physical and chemical properties of the materials which might be promising for applications in catalysis, separation, fuel cells and nanoelectronic devices. Moreover the facile synthesis method proposed for the simultaneous filling up of nanotubes with Pt metal by using metal salt nanofibers as templating structures is another key issue of the present study. Chapter 4 elucidated the synthesis of oxide nanotubes such as $SiO_2$, $TiO_2$ and $SnO_2$ nanotubes embedded with Pt metal using templating nanofibers from $Pt(NH_3)_4(HCO_3)_2$ salt. As part of the study, discrete metal salts of platinum have been investigated to employ as templating structures for the synthesis of metal oxide nanotubes.

The present chapter focuses on the synthesis of oxide nanotubes particularly $SiO_2$ and $TiO_2$ NTs incorporated with Pt metal using nanofibers from a novel salt namely magnus green salt (abbreviated as MGS hereafter) as templating structures. The platinum embedded oxide nanotubes synthesized from MGS demonstrated higher aspect ratio (600 – 800) and higher incorporation of Pt metal inside the nanotubes (≈ 50 wt. - %) at lower temperatures (280°C) when compared to the metal salt, $Pt(NH_3)_4(HCO_3)_2$. Additionally, the incorporation of metal inside the tubes can be achieved at much lower molar ratios of Pt salt.

The strategic formation of nanofibers from quasi one dimensional MGS ($[Pt(NH_3)_4][PtCl_4]$) and their morphology dependence on various parameters were reported in this chapter. A systematic examination of Pt – $SiO_2$ NTs and Pt – $TiO_2$ NTs synthesized from MGS using diverse available characterization techniques were performed and discussed in detail in the subsequent sections of this chapter.

## 5.2 Formation of templating structures from MGS

### 5.2.1 Introduction

MGS is a supramolecular quasi one dimensional platinum compound with a structural formula $[Pt(NH_3)_4][PtCl_4]$. The complex is a semiconductor with columnar structure comprising chains of $[Pt(NH_3)_4]^{2+}$ and $[PtCl_4]^{2-}$ moieties stacked alternatively with linear arrays of platinum atoms separated by a distance of 3.25 A° as illustrated in Figure 5.1 [1]. This inter - platinum distance is larger than the typical bond length of 2.6 – 2.8 A° found e.g. in metallic Pt [2]. The formation of supramolecular arrangement is a consequence of the electrostatic interactions between the oppositely charged coordination units rather than the bonds between the platinum atoms, although the Pt - Pt interactions still exist [3 - 5].

Yamada et al. and others [6 - 9] reported that the green color of the magnus salt is unusual for platinum (II) compounds and arises due to the relatively short Pt – Pt distances. Furthermore their studies proved that this color is characteristic for complexes with inter platinum distances below 3.4 A°. This peculiarly short Pt – Pt spacing is responsible for the semiconducting properties of MGS [10 -12] because shorter the distance between the metal

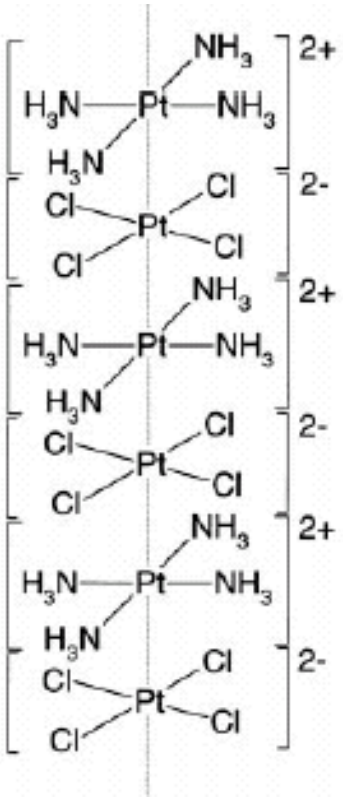


Fig. 5.1 Schematic illustration of crystal structure of MGS

centers higher is the delocalization of the electrons in the quasi one dimensional backbone which largely determines the electrical and optical properties of such compounds. M. Fontana [13] reported that conjugated polymers which usually have low conductivity values when doped with MGS or its derivatives can notably find increase in their conductivity. Hence MGS would be of interest in regard to the better electrical conductivity when compared to $Pt(NH_3)_4(HCO_3)_2$ salt where the Pt atoms are at a distance of 3.8 $A^{\circ}$ [14].

The present section outlines the formation of nanofibers from MGS by solvent modification process which act as templating structures for the formation of oxide nanotubes. The morphology dependence on variation of several parameters were studied and optimized for narrow size distribution. The morphology and the structure of MGS nanofibers were ascertained prominently by using characterization tools such as SEM, XRD, dynamic light scattering spectroscopy (DLSS) and selected area electron diffraction (SAED) in TEM.

### 5.2.2 Experimental details

#### (i) Chemical reagents used

Reagents used in the preparation of MGS nanofibers comprise MGS (Merck), ethanol (99.9%, Merck), TEOS (tetraethyl ortho silicate) (98%, Aldrich) and $H_2O$ (deionised). All the reagents were used as obtained.

#### (ii) Formation of templating nanofibers from MGS

In a typical experiment, 0.0042 mmol of MGS was dissolved in 2 mL of aqueous ammonia solution (0.4 N). At a stirring rate of 300 rpm, 2 mL ethanol was added into the mother solution that resulted in the immediate formation of precipitates from the MGS indicating the onset of primary nucleation.

Customarily, the nanofibers are prepared at $0^{\circ}C$ however for analyzing the influence of temperature the reaction was carried out at $-20^{\circ}C$ and room temperature respectively. Influence of TEOS on the size distribution of the fibers was examined for DLSS analysis by adding 14 μL of TEOS to the mother solution.

### 5.2.3 Results and discussion

#### (i) SEM characterization

Fig. 5.2 (a) depicts the SEM micrograph of commercial MGS which already exhibits one dimensional morphology. Although the structures are not regular, they manifest unambiguously rectangular edges with a rather big size distribution of around 3 μm (Fig. 5.2 (a)). MGS when re – precipitated with ethanol easily yielded Pt salt nanofibers with more regular morphology (Fig. 5.2 (b)). However the size of the fibers reduced sparsely (0.8 - 1 μm) compared to the commercial MGS. Conversely, the template filled nanotubes from MGS exhibited narrow size distribution in the range of 300 – 700 nm. The reduction in size could be attributed to the presence of capping agent that helped in effective control of the particle diameter from the onset of primary nuclei. A detailed description together with experimental data for the formation of thin and monodisperse nanotubes will be discussed in the next sections of this chapter.

As explained in section 4.2.3, Pt nanofibers were developed through the re – precipitation of a soluble $Pt(NH_3)_4(HCO_3)_2$ salt. On contrary, MGS structures when dispersed in ammonia solution were sparingly soluble. Hence, the un - dissolved fraction of salt was separated and only the dissolved fraction of MGS structures in solution was utilized for study so as to have uniform formation of nanofibers.

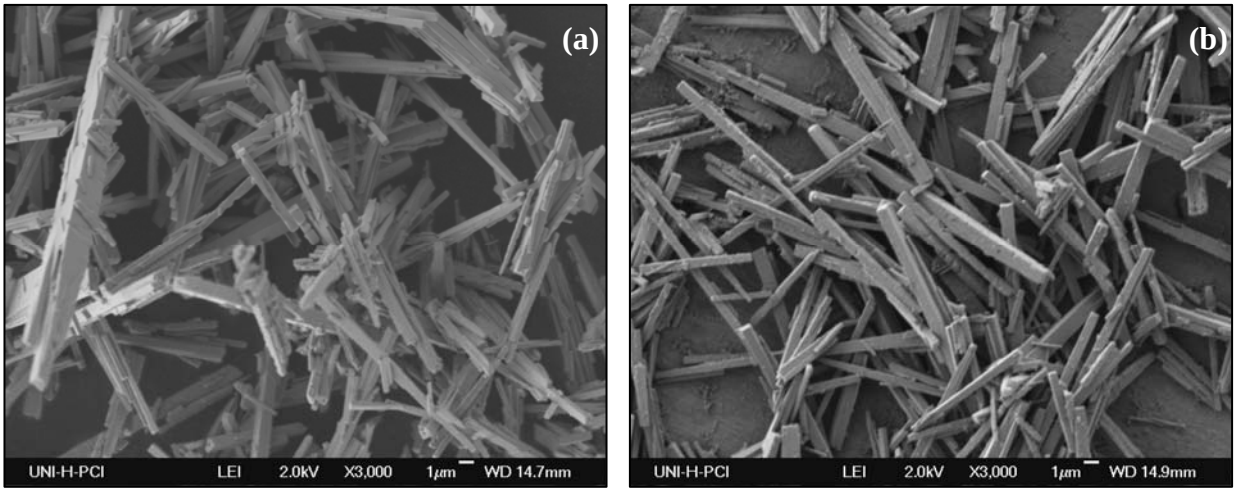


Fig. 5.2 SEM image of (a) commercial MGS and (b) MGS nanofibers obtained by re-precipitation with ethanol

**(ii) Quantitative analysis of nanofiber growth by dynamic light scattering spectroscopy (DLSS)**

The dimensions of nanoparticles at dilute concentrations were investigated using this technique. The present synthesis produces nanofibers with diameter from several hundred nanometers to micromolecular dimensions. Based on the fact that particles of nano size tend to aggregate, the present technique is undoubtedly not an appropriate tool to determine the nanofiber or tube diameter as the data provides quantitative information of the total particle diameter rather than the individual particle diameter. However, in the present case, the analysis helped in estimating the influence of TEOS addition on the size of particles which is

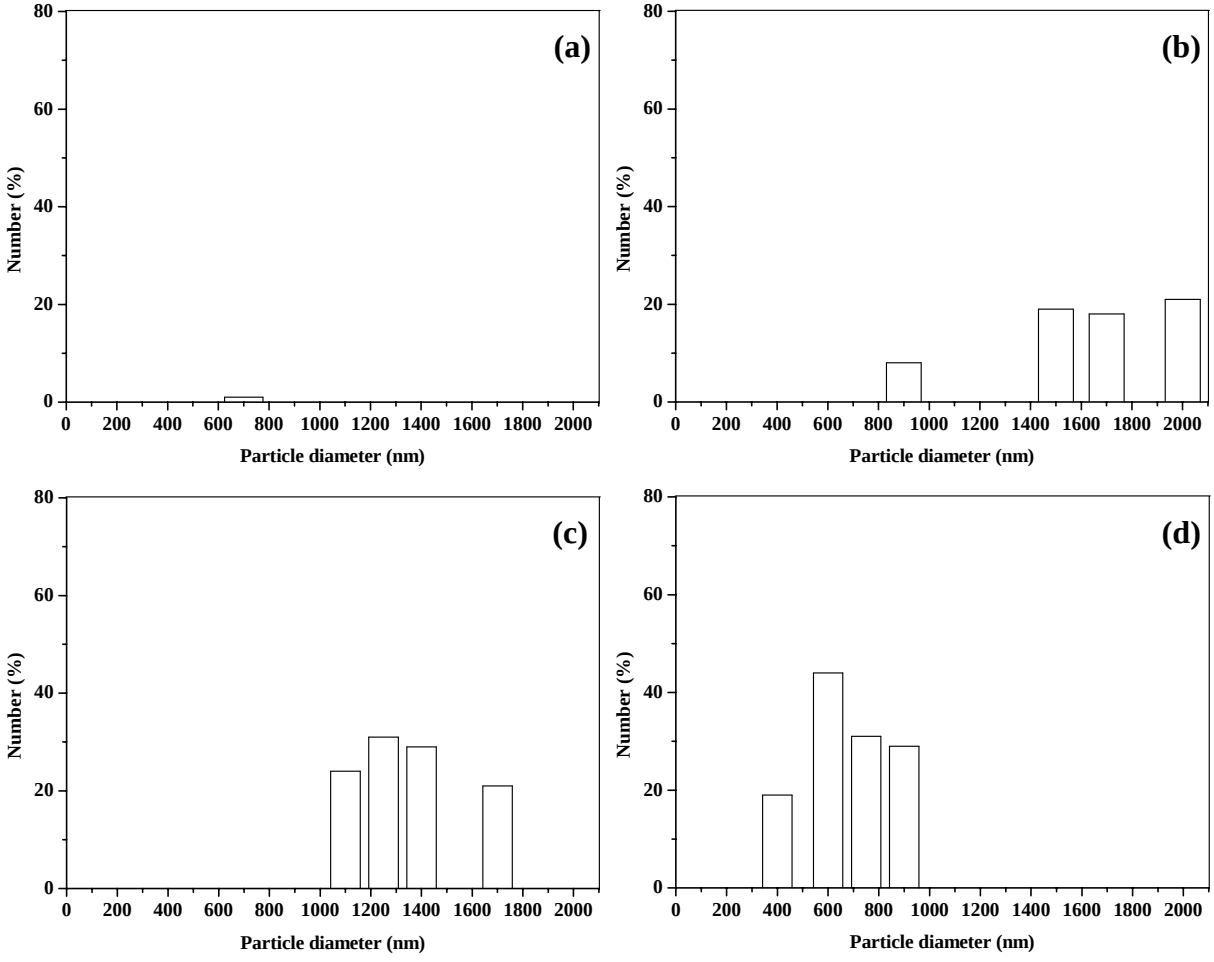


Fig. 5.3 Quantitative data of number concentration (%) obtained from DLS experiments as function of particle diameter (nm). 0.0042 mmol of MGS was dissolved in 2 mL of aqueous ammonia solution and the amounts of ethanol varied are as follows. (a) 1 mL ethanol addition (b) after 5 min of 1 mL ethanol addition (c) 2 mL ethanol addition (d) 2 mL ethanol addition followed by immediate addition of TEOS

in accord with the argument regarding prevention of aggregation of nanofibers using capping agent. DLS experiments were performed to probe the nanoparticle evolution upon the addition of solvent. Fig. 5.3 illustrates the histogram plot of number concentration of nanoparticles suspended in solution as function of particle diameter. As stated earlier, the dissolved fraction of MGS structures in solution was alone utilized for study to ensure monodisperse formation of nanofibers. Accordingly complete dissolution of precursors (i.e lack of nanoparticles) was witnessed from the experiment (not shown). 1 mL of ethanol was added to completely dissolved MGS in aqueous ammonia solution (0. 4 N). No significant nanoparticle condensates were noticed as shown in Fig. 5.3 (a) except for a few particles 700 nm in size. It could be that condensates would have been in smaller diameter distribution which was undetected due to the limitations of the spectroscopy. After 5 min lapse, microparticles with an average size of 1.7 μm were perceived as shown in Fig. 5.3 (b). However 2 mL addition of ethanol to mother solution resulted in a quick appearance of nanoparticle condensates with an average diameter of 1.4 μm as seen from Fig. 5.3 (c). On comparing Fig. 5.3 (b) and Fig. 5.3 (c), it can be apprehended that considerable number of particles form with increased amount of ethanol due to higher availability of precipitates. In order to understand the influence of capping agent in the synthesis of nanotubes, TEOS was added immediately after the addition of 2 mL ethanol to mother solution. Fig. 5.3 (d) shows that the particle diameter remarkably reduced to 0.65 μm upon TEOS addition. The fact that the particles in Fig. 5.3 (d) are smaller when compared to particles in Fig. 5.3 (c) demonstrates that the aggregation in Fig. 5.3 (c) might take place during the measurement. The result thus validates that the presence of hydrolyzed TEOS in the suspension was responsible in blocking the surface of MGS nanofibers from aggregation similar to the observation recognized with nanofibers from $Pt(NH_3)_4(HCO_3)_2$ salt [15].

**(iii) X – ray diffraction analysis**

Fig. 5.4 displays XRD patterns of commercial MGS and the nanofibers from MGS obtained by re – precipitation of the aqueous salt solution with ethanol. To investigate the XRD pattern of nanofibers from MGS, the suspended nanofibers in solution were centrifuged and the solid fraction was separated. The solid particles were then dried in air at room temperature for analysis.

The XRD patterns reveal that the composition of Pt metal nanofibers matches with that of the commercial MGS though the intensities of Pt fibers are relatively weaker when compared to the commercial salt. The slight discrepancy in the crystallinity could have been from the impurities in ethanol. However the strong and intense peaks reveal that both commercial MGS as well as the nanofibers from MGS exhibit good crystallinity.

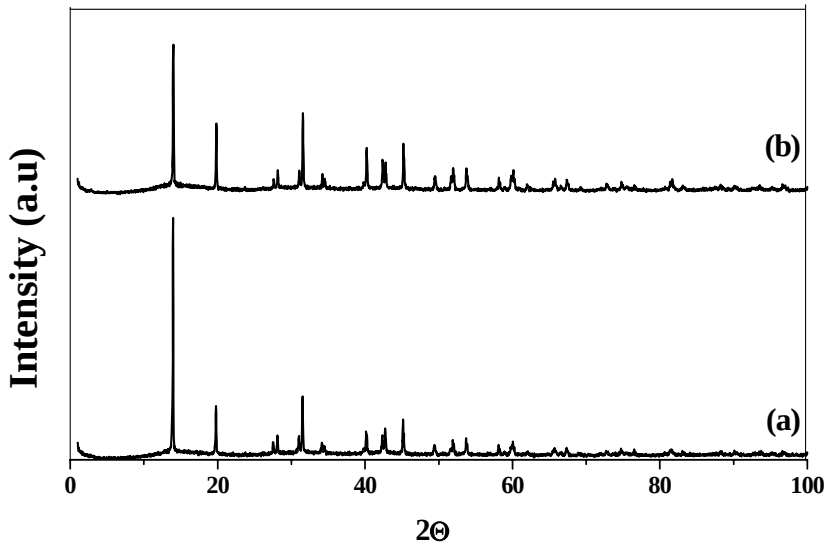


Figure 5.4 XRD patterns of commercial (a) MGS and (b) Pt metal nanofibers

**(iv) TEM and SAED analysis**

The micrograph in Fig. 5.5 represents the TEM image of MGS fiber. The solid fiber was homogenous and consistent with SEM observations indicating a tubular morphology with diameter close to 1 μm. The crystalline structure of MGS fibers could be easily destroyed under illumination with high - energy electrons in the TEM leaving an amorphous product.

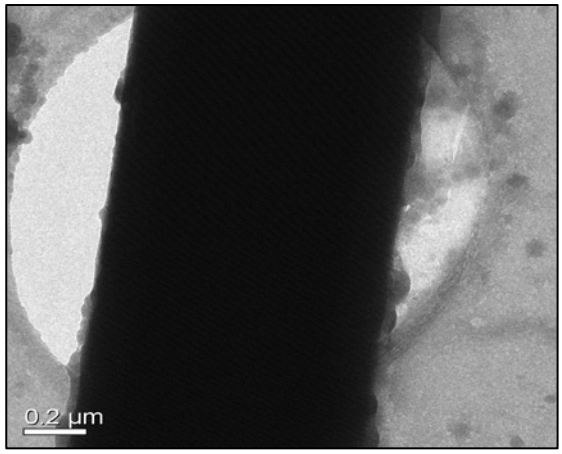


Fig. 5.5 TEM image of MGS nanofiber

Therefore, to obtain a diffraction pattern, it was essential to work at lower electron intensities of approximately 0.3 A/cm$^2$ at specimen scale by choosing proper spot sizes and defocusing the condenser lens (CL3). MGS fibers were oriented relative to the electron beam using a double - tilt specimen holder. Strongly defocused diffraction pattern was observed on the TV rate camera of the imaging filter until 'zone - axis pattern' was obtained that showed diffraction spots along the fiber axis. Finally, the diffraction pattern was acquired on a slow scan CCD camera.

A bright - field micrograph of MGS fiber is shown in Fig. 5.6 (a). The electron diffraction pattern in Fig. 5.6 (b) and Fig. 5.6 (c) was taken from the marked circular area shown in Fig. 5.6 (a). Usually the zone axis is determined by the periodic banding resulting from the fiber

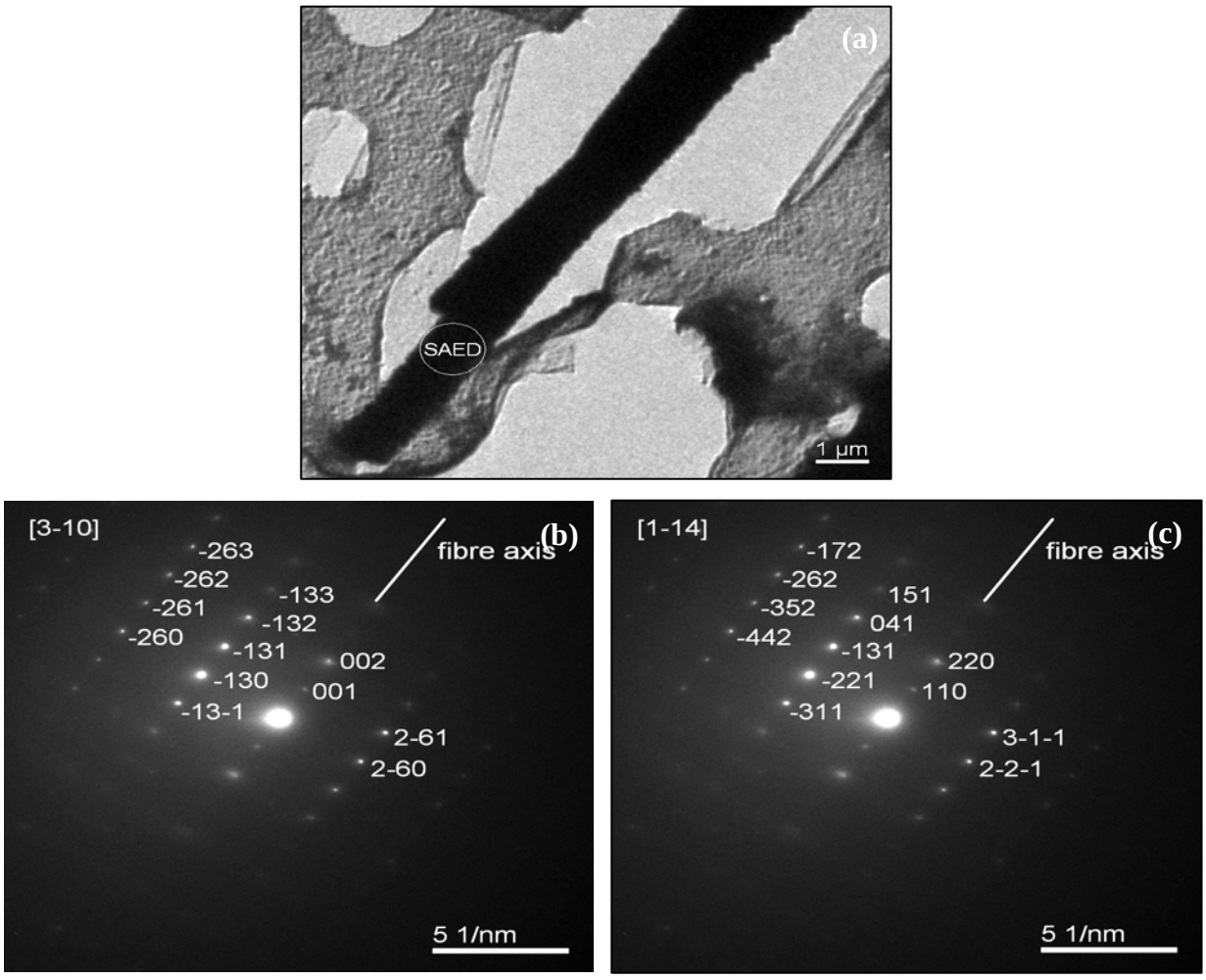


Fig. 5.6 (a) TEM bright - field micrograph of precipitated MGS salt fiber on a carbon foil (b, c) electron diffraction pattern of selected area (marked in (a)) with indices of lattice planes according to two different zone axes [3-10] and [1-14] as depicted in (b) and (c) respectively

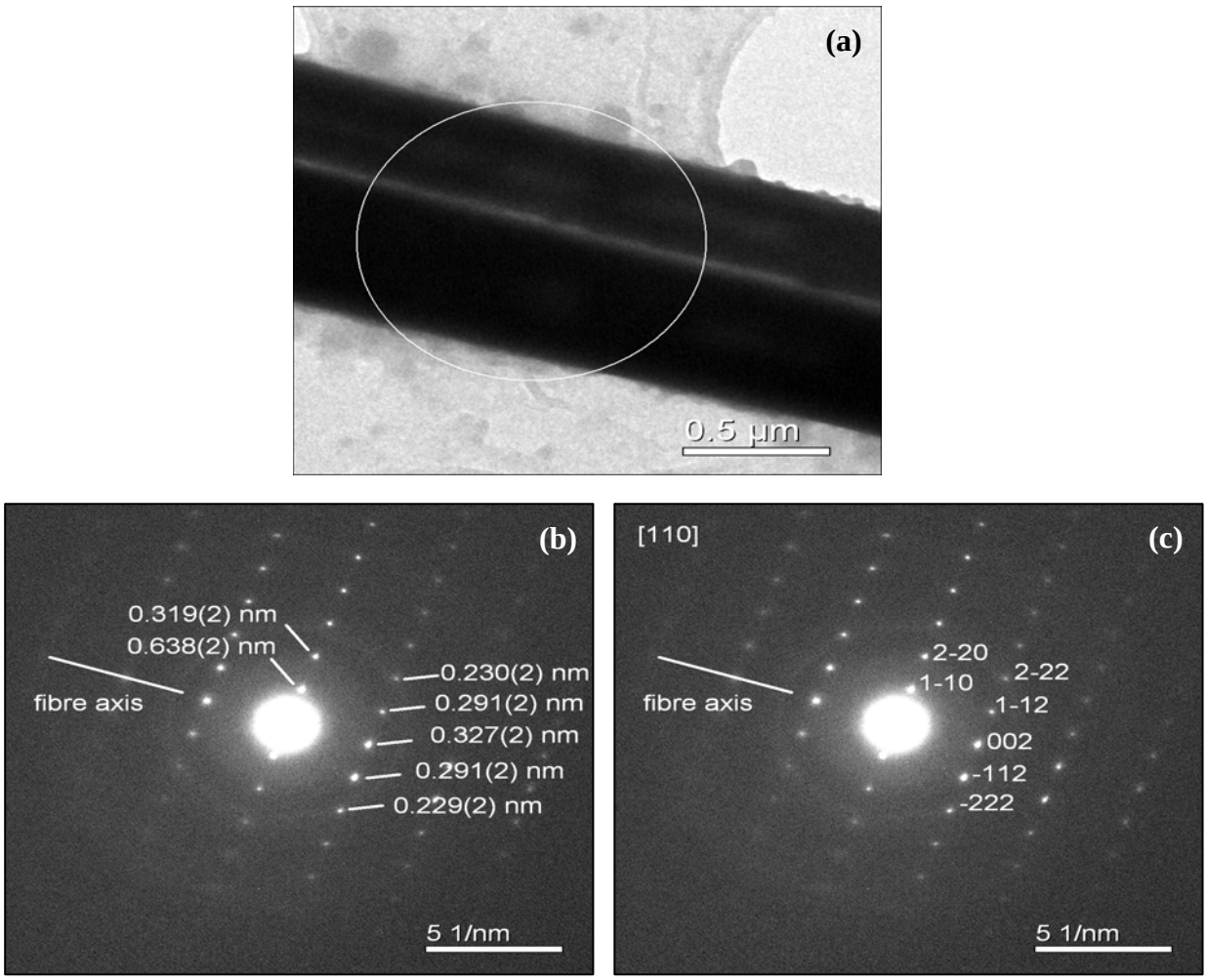


Fig. 5.7 Electron diffraction pattern of a 1.2 µm circular area on a gold - coated MGS fiber with indication of (a) measured lattice plane distances (b, c) indexed according to the [100] and [110] zone axes

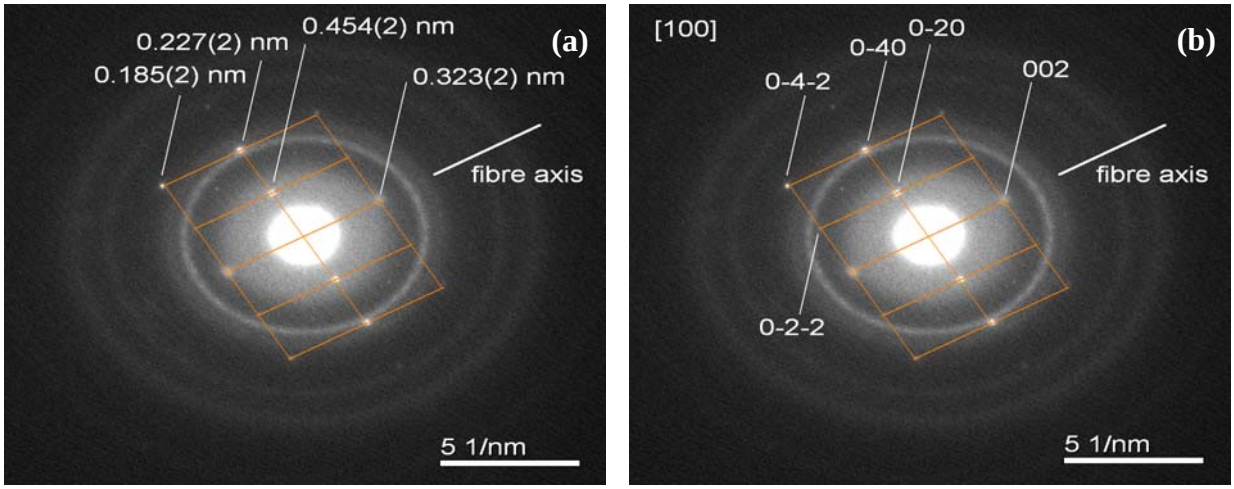


Fig. 5.8 (a) TEM bright - field micrograph of precipitated MGS salt fiber on a carbon foil coated with gold (b) electron diffraction pattern of selected area marked with indication of measured lattice plane distances, (c) pattern of (b) indexed according to the [110] zone axis

crystals. A highly periodic banding was reported by Wang et al. [16] in determining the chalcedony specimens. However alternate banding is also noticed when the distance between the coarse and fiber grained crystals oscilliate [17]. As demonstrated by Miehe et al. [18], grains that share a common crystallographic orientation align. Presumably, such strings of crystallites make up the fiber axis as shown in the Fig. 5.6. Due to the complex crystal structure of MGS [19], few lattice fringe distances of different Miller's indices (hkl) are too close and not easily distinguishable within the accuracy of SAED pattern. Due to this difficulty, the diffraction pattern in Figs. 5.6 (b, c) could be indexed on one hand according to a [3-10] zone axis (Fig. 5.6 (b)) and on the other hand according to a [1-14] zone axis (Fig. 5.6 (c)). Thus, there arises two possibilities for determining the fiber axis namely along [001] (Fig. 5.6 (b)) or along [110] planes (Fig. 5.6 (c)).

To improve the accuracy of the diffraction measurement, specimen was coated with gold as an internal standard. The lattice planes of gold with $d_{111}$ (Au) = 0.2355 nm give rise to a pronounced Debye - Scherrer ring as portrayed in Figs. 5.7 (a, b). This internal calibration of the diffraction pattern allowed a more accurate measurement of the lattice plane distances from the corresponding MGS reflexes as indicated in Fig. 5.7 (a). Thus indexing of the diffraction pattern of Figs. 5.7 (a, b) according to a [100] zone axis was undoubtedly possible, yielding the fiber axis to be along [002] and subsequently [001].

In order to substantiate the fiber axis, an analogous measurement was performed as shown in Fig. 5.8. Gold particles of up to 100 nm in diameter were recognized (Fig. 5.8 (a)). Measured lattice fringe distances are indicated in Fig. 5.8 (b)). The indexing of the [110] zone axis pattern (Fig. 5.8 (c)) yields the fiber axis to be along [002] and subsequently [001] as well. This coincides the result from earlier measurement confirming the fiber axis along [001] zone axis. It is worthy to not that within the accuracy of SAED method, no single diffraction pattern was found to contradict the conclusion of the fibre axis.

### 5.2.4 Influence of parameters on morphology of MGS nanofibers

Wang et al. [20] observed that rapid addition of aqueous ammonia solution under static conditions yielded uniform micro - sized rods while slow addition under stirring conditions gave $SiO_2$ NTs in presence of citric acid as templating molecules. Therefore, it is evident that synthetic conditions play a key role in influencing the formation of desired structures.

Likewise, our earlier studies on fibers from $Pt(NH_3)_4(HCO_3)_2$ salt as disclosed in chapter 4 also revealed that the morphology of templating structures are largely influenced by reaction conditions. Hence detailed evaluations of the reaction parameters that can influence the morphology of MGS fibers are discussed in this section. Since our aim lies in attaining uniform geometry with narrow size distribution of product nanotubes, it becomes essential to tune the template nanofibers as well to smaller sizes under optimum reaction conditions. As demonstrated in chapter 4, capping agents played a significant role also in controlling the growth of MGS nanofibers by hindering their aggregation to achieve monodisperse and high aspect ratios of nanotubes which will be elaborated with experimental results in succeeding sections of this chapter.

**(i) Variation of temperature**

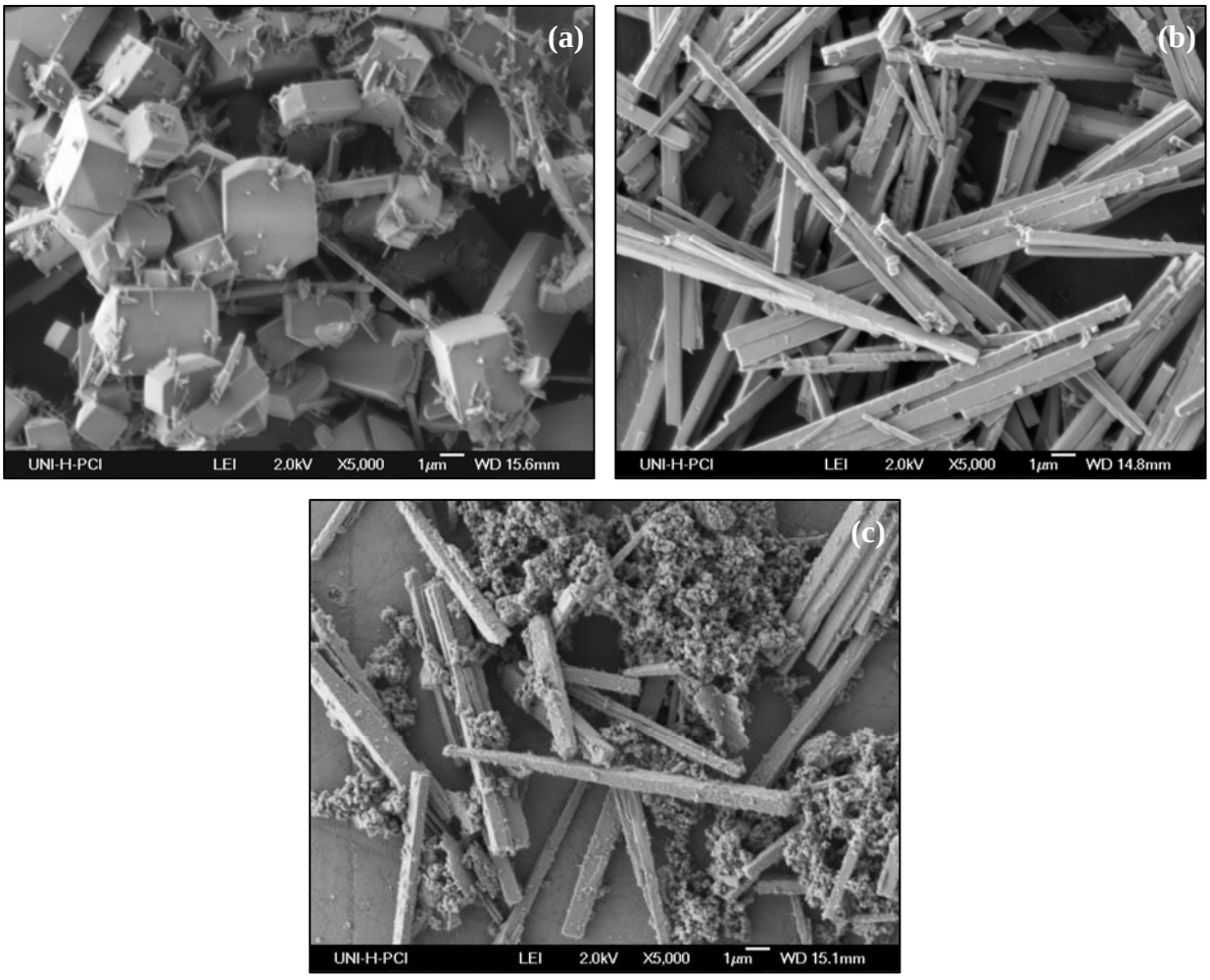


Fig. 5.9 Template nanofibers of salt concentration 0.0013 M with a rate of ethanol addition 0.5 mL/min and ethanol/water ratio of 5:1 at a temperature of (a) 21°C (room temperature) (b) 0°C (c) -20°C

As explained in section 5.2.2, template structures were prepared from MGS by varying the temperature of reaction. Fig. 5.9 shows the SEM images illustrating the effect of varying temperature on the morphology of nanofibers. At room temperature fibers of size with diameter in range of 0.3 – 2.5 μm were obtained while at 0°C, long tubes of lengths between 5 and 20 μm and diameter in range of 0.2 – 1 μm were noticed. As temperature was further reduced to -20°C the tubes became shorter in length (4 – 8 μm) and were accompanied by lot of undesired materials. On the other hand, maintaining the temperature at -20°C was difficult to handle and often resulted in freezing of the aqueous solution.

From Fig. 5.9 (a) and Fig. 5.9 (b) it is obvious that as the temperature was reduced from room temperature to 0°C the fibers shrinked in diameter. At 0°C the dissolution of salt in aqueous solution is lower than at room temperature leading to formation of a higher number of nuclei. Moreover there is less mobility of ions at lower temperature and hence less time available for ions to organize into larger crystals. Therefore the crystals remain smaller in size. On the contrary there is rapid mobility of ions at higher temperatures leading to aggregation thereby the crystals grow larger.

When temperature was further reduced to -20°C the tubes not only became shorter but were also associated with some particles as seen in Fig. 5.9 (c). A similar observation was made by Miyaji et al. [21] where they describe the process of crystallization as 'incipient crystallization. When a solution is cooled down to a temperature below the incipient crystallization temperature, particularly from a supersaturated solution, undesired spontaneous nucleation in the bulk of the solution occurs, resulting in the formation of a solid mass which cannot be stirred, pumped, filtered or washed conveniently. The shorter tube lengths could be because of the lesser mobility of ions at such lower temperature and consequently lack of adequate time for the growing of crystals. Henceforth a temperature of 0°C was considered as an optimum temperature for the formation of monodisperse nanofibers from MGS.

**(ii) Variation of salt concentration**

The influence of varying concentration of salt on morphology of MGS fibers was examined with different molar ratios of MGS whose images from SEM are shown in Fig. 5.10. The study of salt concentration plays a vital role in the present work as the objective lies in synthesizing well defined geometry of MGS fibers with narrow size distribution at lower

molar ratios. From earlier studies it was realized that narrow size distribution is favored only when the lateral aggregation of primary nuclei in the reaction system is suppressed. As demonstrated in chapter 4, capping agents worked efficiently in arresting the aggregation of fibers from $Pt(NH_3)_4(HCO_3)_2$ salt. Hence, in similar way, TEOS was also adopted in the present situation to avoid the aggregation of primary nanofibers resulting from MGS. As addition of TEOS plays a prominent role in regulating the size distribution of template nanofibers, the samples in this study constitute TEOS in order to compare to the actual synthesis process of nanotubes.

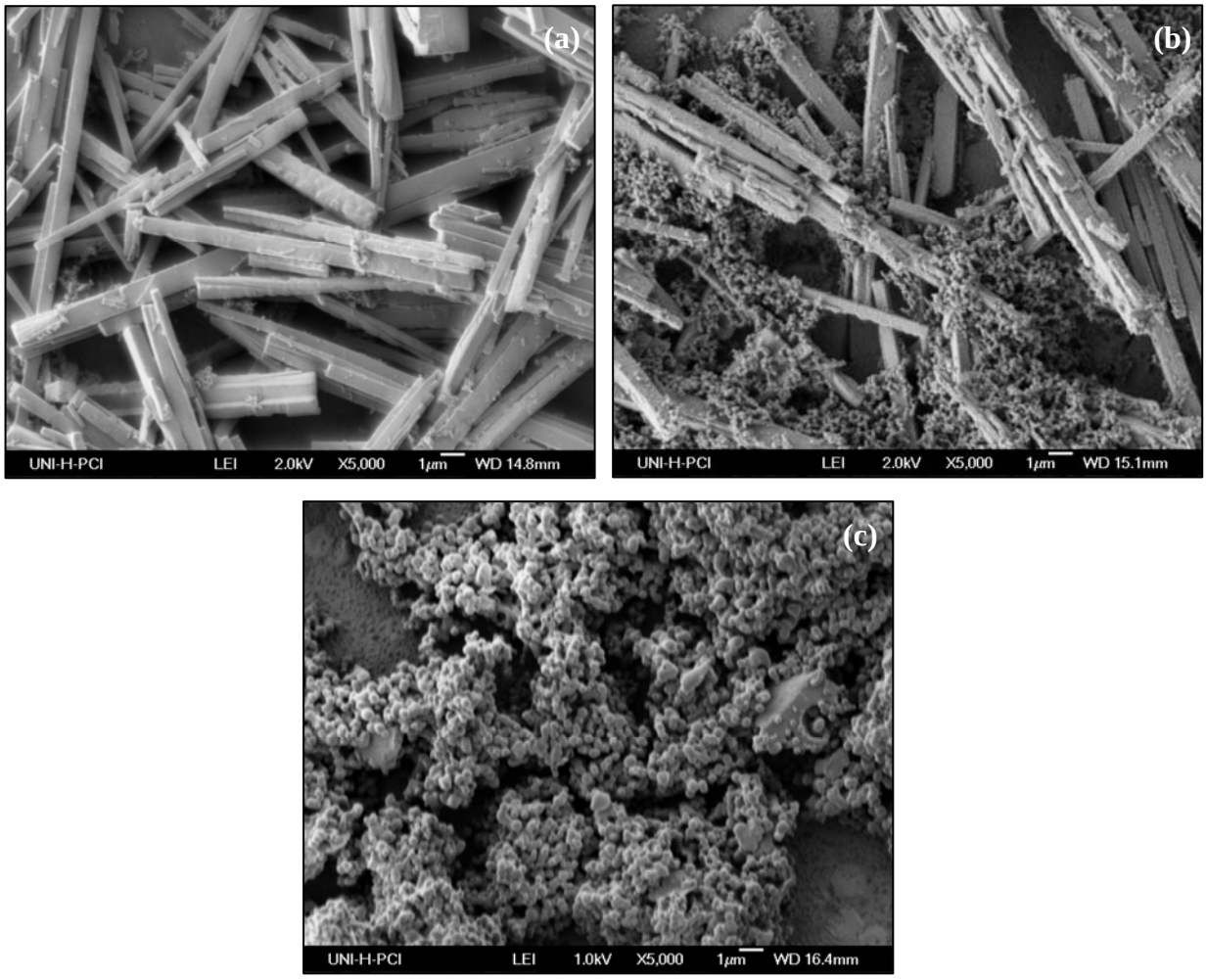


Fig. 5.10 Template nanofibers were prepared at a temperature of $0^{\circ}C$ consisting of ethanol/water ratio of 5:1 with ethanol added at a rate of 0.5 mL/min into the mother solution. The concentration of salt in mother solution was varied from (a) 0.0013 M (b) 0.0006M to (c) 0.0003M under above reaction conditions

With a salt concentration of 0.0013 M, monodisperse fibers with smooth surfaces were obtained as shown in Fig. 5.10 (a). However when concentration was reduced to half its value

to 0.0006 M, not only the amount of fibers decreased but also particles of around 50 nm were observed as illustrated in Fig. 5.10 (b). When the concentration was further reduced to 0.0003 M, spherical spheres of silica with complete absence of fibers were observed as seen in Fig. 5.10 (c).

As explained in chapter 2, in a solution where the concentration is close to saturation the solute molecules undergo in - situ aggregation because of the attractive forces existing between them. The solute molecules agglomerate to form a protocrystal which serves as a nucleation site and the other solute molecules in the solution adhere to this protocrystal thereby forming a crystal. In the present scenario, when the concentration of salt is 0.0013 M, the solute molecules are adequate to grow into bigger crystals and with addition of TEOS before formation of template structures resulted in uniform and considerable size distribution of fibers. When the concentration was reduced (0.0006 M), it is probable that the solute molecules were not sufficient enough to aggregate to the protocrystals and hence the TEOS added, was deposited on these pre - crystals resulting in the formation of particles.

When the concentration was reduced even further, fibers were vanished completely and only particulates from TEOS were observed similar to the observation made by Stöber et al. [22] who could obtain monodisperse silica spheres from TEOS which were of 50 – 2000 nm in diameter. The study therefore concludes that the concentration of 0.0013 M is optimum value for formation of uniform fibers with no traces of impurities. However undesired particles with meagre amount of fibers start to dominate as the concentration was reduced.

**(iii) Variation of ethanol to water concentration and rate of addition of ethanol**

Another competent parameter that can greatly influence the size distribution of templating structures is the ethanol/water ratio and the rate at which it is added into the solution. Hence, the samples in Fig. 5.11 were prepared with an optimum salt concentration of 0.0013 M by maintaining the reaction system at a temperature of $0^{\circ}$C while varying the ethanol/water ratios along with its speed of addition into solution as shown.

The SEM image shown in Fig. 5.11 (a) portrays the morphology of fibers with ethanol/water ratio of 1:1 (2 ml of ethanol was added into the mother solution) while that of Fig. 5.11 (b) and Fig. 5.11 (c) represent the fibers with ethanol/water ratio of 5:1 and 10:1 added at a rate

of 0.5 mL/min respectively. When the ratio of ethanol concentration to water was 1:1 it can be noticed that the fibers were laterally aggregated into bundles. When the ethanol to water

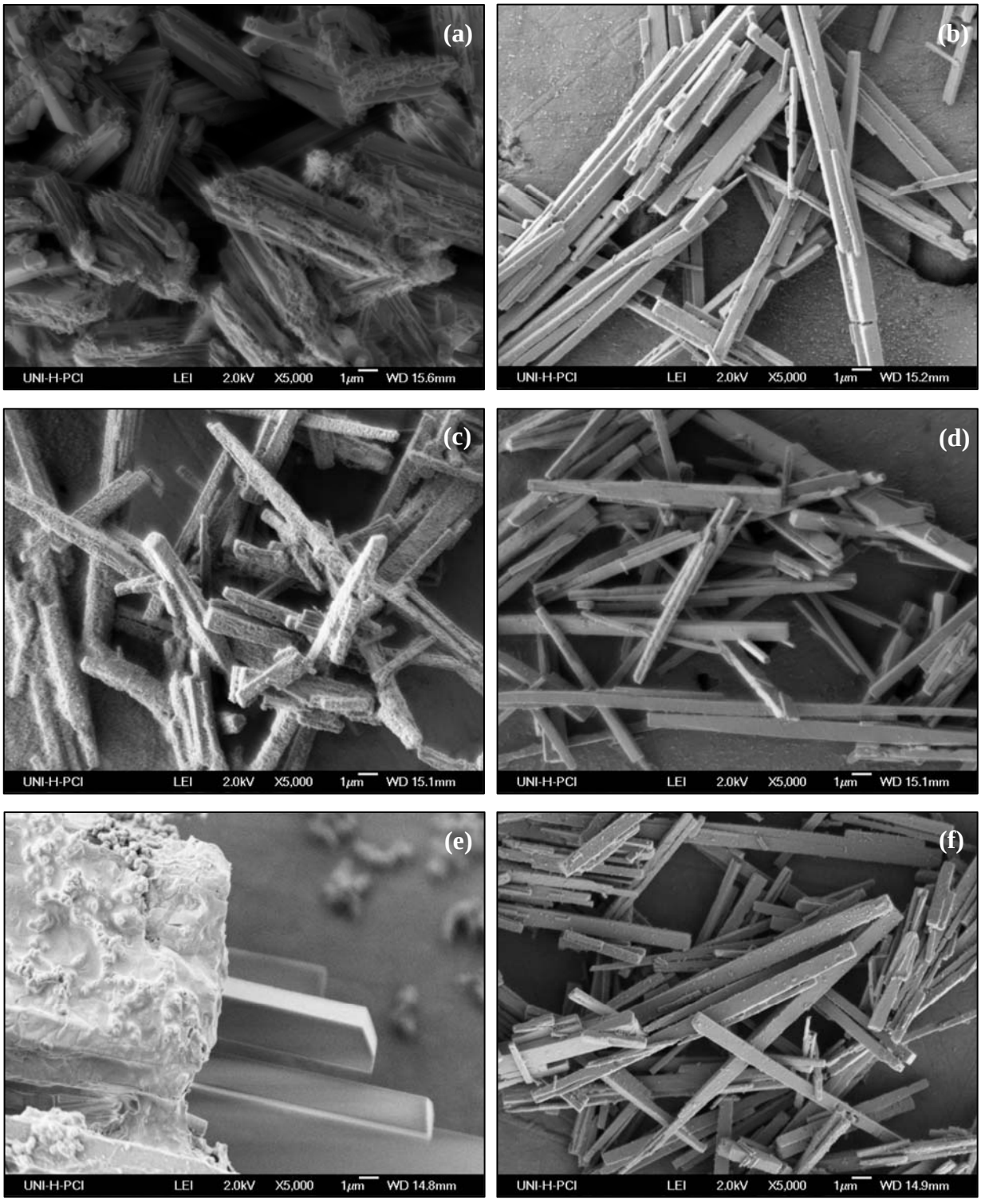


Fig. 5.11 MGS nanofibers were prepared with a salt concentration of 0.0013 M and at a temperature of 0°C. The ethanol/water ratio and rate of ethanol addition parameters were varied in the respective sequence as (a) 1:1 ; 0.5 mL/min (b) 5:1 ; 0.5 mL/min (c) 10:1 ; 0.5 mL/min (d) 5:1 ; 1 mL/min (e) 5:1 ; 1 mL/min in presence of TEOS (f) 5:1 ; 0.25 mL/min

concentration was increased to 5:1 not only the yield was higher but also the fibers were grown to the longest (≈ 50 μm). However when the ethanol/water was further increased to 10:1, the fibers became shorter besides resulting in the formation of undesired particles. The result concludes that the addition of more solvent acts as a randomizing force in solution causing the aggregates of molecules to break up. Nevertheless, when the concentration of solvent was increased beyond the optimum value (5:1) the solute molecules take longer time to agglomerate into a crystal. Hence the fibers were shorter due to the lapse while the precipitates from the addition of solvent remained as particles in the solution.

The addition of ethanol with an optimum ratio of ethanol concentration to water 5:1 was varied and compared. The rate of ethanol addition at 1 mL/min as shown in Fig. 5.11 (d) exhibited narrow size distribution than the 0.5 mL/min addition (Fig. 5.11 (b)) due to the faster nucleation rate in the former case. In order to compare with the actual synthesis process, TEOS was added prior to the addition of ethanol at 1 mL/min and examined by SEM as illustrated in Fig. 5.11 (e). The image shows that TEOS could not coat the template assembly uniformly as the speed of ethanol addition was too fast not providing adequate time for deposition. The slower addition of ethanol (0.25 mL/min) as shown in Fig. 5.11 (f) also resulted in monodisperse fibers with size distribution of 1 μm similar to Fig. 5.11 (b). However optimum of 0.5 mL/min was taken into consideration with respect to faster time of formation of fibers.

Apart from the above factors, choice of solvent plays an effective role in influencing the mechanism of crystal growth as the solvent is more likely to be incorporated into the crystal lattice. While the use of isopropanol as solvent gave identical results to ethanol, methanol resulted in formation of spherical particles resulting from TEOS addition with no presence of fibers from MGS. The absence of fibers could have been from the higher condensation rates coming forth from more polar methanol.

**(iv) Influence of pH and stirring speed in the reaction system**

Table 5.1 displays the yield of fibers with varying ammonia concentration in $NH_4OH$ solution. It can be perceived that the yield of the fibers increases as the concentration of ammonia in $NH_4OH$ solution increases. The concentration of $NH_3$ in the solution is compared to the pH of the mother solution. When the pH of the mother solution was 10 not only the

yield of the fibers formed was higher but also the tubes were longer. When the pH was lower, the tubes became shorter and the yield of fibers decreased remarkably. The decrease in pH can be reflected to the increase in amount of water because the addition of water lowers the basicity of solution. Hence the scenario becomes similar to the increase in solvent concentration as discussed in the earlier section (Fig. 5.11 (c)). With the increase in the amount of water in solution the solute molecules take longer hours to aggregate into a crystal and consequently shorter fibers result associated with lot of particles.

With respect to the stability of basic aminometallic compounds (MGS in present case), pH in the range of 9 – 10 is usually favoured. As explained in chapter 2, Ostwald ripening process favours in a basic medium where the growth occurs essentially through the addition of monomers to the highly condensed particles rather than by mere aggregation of particles. As a result, pH around 10 was preferred. Added to that, solubility of silica increases with increase in pH. Hence higher ammonia concentrations were ruled out as TEOS plays a key parameter in the present synthesis approach.

| pH | No. of fibers (%) |
|---|---|
| 9 | 35 |
| 10 | 90 |
| 10.5 | 80 |
| 11 | 75 |

Table 5.1 Effect of varying $NH_3$ to water in $NH_4OH$ solution

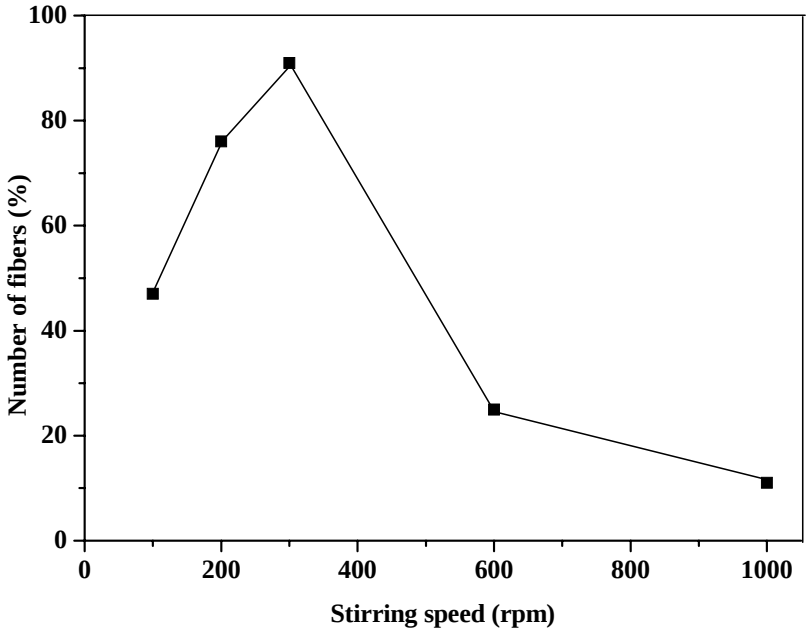


Fig. 5.12 Effect of stirring rate on number of fibers formed

The influence of stirring rate was studied by varying the speed in the range of 100 – 1000 rpm. Fig. 5.12 shows that stirring rate influences the formation of fibers. As the stirring speed is increased from 100 – 300 rpm the yield of fibers increases and thereafter the yield decreases until no fibers were formed at stirring rates higher than 1000 rpm. Beyond the stirring rate of 300 rpm, the decrease in formation of fibers could be attributed either to the breaking up of template assemblies or to the unfavoured aggregation of solute molecules in crystal growth. The effect of stirring speed is subtle and cannot be generalized for every system.

## 5.3 Pt – $SiO_2$ NTs

### 5.3.1 Introduction

Availing templating fibers from a novel salt namely MGS ($[Pt(NH_3)_4][PtCl_4]$) to synthesize Pt – $SiO_2$ NTs stands out as one of the primary focuses of the present study. The interpretation of the experimental study reveals high aspect ratios of nanotubes with lengths upto 60 μm long and 300 - 700 nm in diameter. Additionally, these ultra long Pt – $SiO_2$ NTs could host explicitly higher amounts of Pt (48 - 51 wt. - %) in their interior voids at lower temperatures and lower molar ratios when compared to Pt – $SiO_2$ NTs synthesized from fibers of $Pt(NH_3)_4(HCO_3)_2$ salt.

The present section investigates the synthesis approach of Pt – $SiO_2$ NTs using fibers from MGS and explores the possible growth mechanisms. The effect of TEOS as capping agent in the synthesis study was examined and elaborated in detail with experimental evidence.

### 5.3.2 Experimental details

#### (i) Chemical reagents used

Reagents used in the synthesis of $SiO_2$ NTs included TEOS (tetraethyl ortho silicate) (98%, Aldrich), ethanol (99.9%, Merck), MGS (Merck), $H_2O$ (deionised). All the reagents were used as supplied without further purification.

**(ii) Synthesis of high aspect ratio Pt - $SiO_2$ NTs**

To couple the rate of hydrolysis of TEOS and its interaction with the template nanofibers so as to form higher aspect ratios of $SiO_2$ NTS, various parameters such as ageing time, amounts of TEOS and water, temperature and pH of the solution were varied. The optimized molar ratios to synthesize $SiO_2$ NTs using MGS as template are given below.

In a typical synthesis, 0.0042 mmol of MGS was dispersed in 2 mL of aqueous ammonia solution (0.4 N). To this solution, 2 mL of ethanol was added at a stirring rate of 300 rpm. The system was placed inside an ice bath (0°C) for 10 min. 14 µL of tetraethyl orthosilicate (TEOS) was added drop wise into the mother solution and stirred for 2 min. After increasing the rate of stirring to 1000 rpm 0.1 mL of ethanol was injected swiftly. A few minutes later, the stirring rate was reduced to 300 rpm and 10 mL of ethanol was added slowly at a rate of 0.5 mL/min. The reaction system was aged in the cold bath for 3 h and then allowed to warm up to room temperature for 4 h. The obtained product was then washed with water and dried at room temperature. The dried samples were calcined at 280°C for 6 h at a heating rate of 1°C/min.

### 5.3.3 Results and discussion

**(i) Characterisation with SEM on morphology of the tubes**

Scanning electron micrographs shown in Fig. 5.13 from as - synthesized Pt - $SiO_2$ NTs prove the regularity of the fibrous structures. The tubular morphology exhibited by the nanotubes clearly stands as replica from the MGS fibers demonstrated in section 5.2. From Fig. 5.13 (a), it can be noticed that the tubes are up to 60 µm long. The length of the silica tubes is on average much increased with respect to the templating fibers indicating that the growth of $SiO_2$ tube by itself is anisotropic. Majority of nanotubes exhibited diameters in the range of 300 – 700 nm as shown both in Figs. 5.13 (b, c) as well as in the histogram plot in Fig. 5.14 collected from a typical batch of $SiO_2$ NTs. The tubes further depicted rectangular cross – section with very few tubes having open tube endings as represented in the inset of Fig. 5.13 (c). A similar observation was established in the case of Pt – $SnO_2$ NTs (section 4.5).

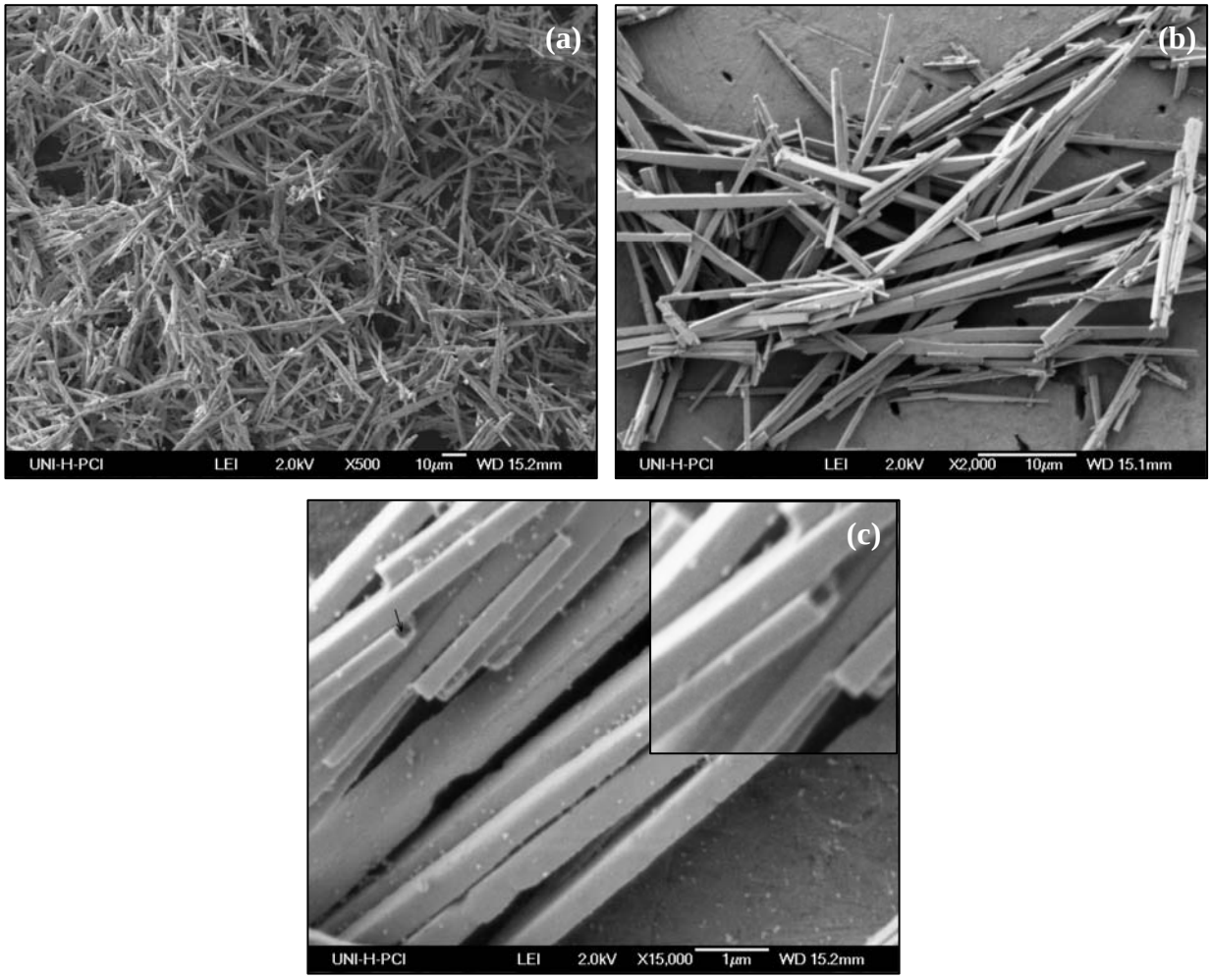


Fig. 5.13 SEM micrograph revealing high aspect ratios (600-800) of Pt - $SiO_2$ NTs (b, c) narrow size distribution of Pt - $SiO_2$ NTs at lower and higher magnifications respectively with inset indicating the rectangular cross - section of the tubes.

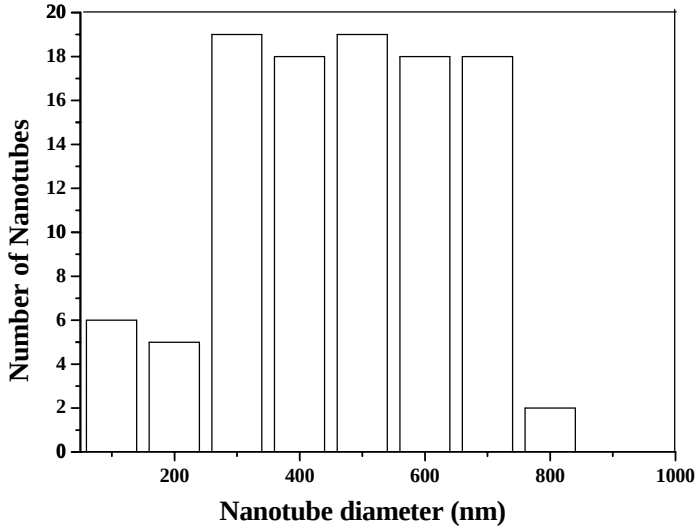


Fig. 5.14 Histogram plot of a typical batch of $SiO_2$ NTs with number of nanotubes in a given diameter class versus diameter of the tube

As described in section 5.2, Pt - $SiO_2$ NTs seem to possess narrow size distribution than the MGS fibers obtained from re – precipitation of MGS salt. The reduction in size could be attributed to the presence of capping agent that helped in effective control of the particle diameter from the onset of primary nuclei itself. In our earlier work (chapter 4), TEOS was utilized as capping agent which effectively stabilized the primary nanofibers from $[Pt(NH_3)_4](HCO_3)_2$ salt leading to the controlled growth of metal containing silica NTs. Hence in the present study too, TEOS helped in arresting the aggregation of MGS nanofibers resulting in the formation of monodisperse nanotubes with high aspect ratios (600 - 800).

As narrated in Chapter 2, DLVO theory suggests that the stability of a colloidal system is determined by the sum of the van der waals attractive forces and electrical double layer repulsive forces that exist between particles as they approach each other due to the Brownian motion they are undergoing. This theory proposes that an energy barrier resulting from the repulsive force prevents two particles approaching one another and adhering together. The steric repulsion mechanism involves adding polymers similar to capping agents in our system adsorbing onto the particle surface and preventing the particle surfaces coming into close contact. If enough capping agent adsorbs, the thickness of the coating is sufficient to keep particles separated by steric repulsions between the monomer layers, and at those separations the van der waals forces are too weak to cause the particles to adhere. Under basic conditions silanol would be deprotonated and hence mutually repulsive also relatively stable according to the DLVO theory [23]. As proposed by Sun et al. and others [24 – 27] capping agents kinetically control the growth rates of various faces through adsorption and desorption. Xia et al. [28] achieved silver nanowires with high aspect ratios (approx. 1000) with the presence of PVP (poly vinyl pyrrolidone) which adsorbed on the surfaces of silver nanoparticles by preventing them from aggregation. Similarly, Shi et al [29] attained monodisperse CdSe nanorods with controlled aspect ratio by using a mixture of trioctyl phosphine oxide and hexyl phosphonic acid as capping agents. Therefore, TEOS was opted in our synthesis approach as capping agent which can achieve steric as well as electrostatic stabilization.

TEOS when added to the mother solution (MGS salt in aqueous ammonia solution) undergoes intensive hydrolysis. As explained in section 4.3, in order to promote the hydrolysis of TEOS, aqueous $NH_3$ acts in our system as a base catalyst, wherein the silicate monomers from the TEOS deprotonate and adsorb on the specific facets of nuclei formed from the MGS in the mother solution. For e.g in the alkali medium, the resulting negatively charged silicate monomers might behave as electron donors and form hydrogen bonds with the $NH_3$ ligands of

the cationic $Pt^{2+}$ complex in the MGS. However, the interaction occurs with different probabilitites on the different facets of the salt fibers. In the growth direction of MGS, less $[Pt(NH_3)_4]^{2+}$ units are available and thus the coating with silicate monomers is hampered. On the other hand the small faces at the top and bottom side of the MGS fibers are attractive for an interaction with other fibers because $[Pt(NH_3)_4]^{2+}$ units can interact with $[PtCl_4^{2-}]$ units. This attractive interaction promotes the formation of $SiO_2$ tubes even longer than the original MGS fibers as mentioned above. Owing to these interactions with the template, a layer of silanol molecules would adsorb on the surface of the template and subsequently the follow-up adsorbates (TEOS monomers) deposit on the first layer and the –Si-O-Si- bonds are formed by rapid condensation. Consequently strong bonds form between growth units according to the Periodic bond theory [30], which claims that an uninterrupted chain of strong bonds repeat periodically in the formation of a crystal. Subsequent addition of monomers lead to few nanometer thick walls depending on the availability of TEOS monomers.

Comparatively the tubes were thinner than the fibers from MGS because of the addition of TEOS during the growth of protocrystals itself which suppressed the lateral aggregation from the fibers. In addition, maintaining the reaction temperature to $0^{\circ}C$ was important in this study as it slows down the hydrolysis and condensation rate sufficiently that the soluble silicates are only polymerized on the surface of the template and any unwanted formed morphologies are thwarted from aggregating.

Pt – $SiO_2$ NTs synthesized in the absence of TEOS led to the formation high size distribution of nanotubes (4 – 10 μm) thus ensuring that TEOS as capping agent proved to be an essential factor in controlling the growth of the nanotubes. The images from Fig. 5.13 show that the tubes had clear and smooth surfaces pointing that the consumption of TEOS on the surface of the templating MGS fibers was complete. However the open tube ends in few of the tubes could be ascribed to the similar argument as stated in section 4.5 that the deposition of TEOS on the tube ends would have been relatively difficult because of the continuous growing of the corresponding facet. Apart from acting as a capping agent, TEOS in the present study also served as a protective layer for the Pt nanofibers thereby avoiding their deformation at higher temperatures which will be discussed in the next parts of this section.

**(ii) TEM and SAED characterization**

The dispensation of metal clusters in the nanocomposites can be incited either by electron bombardment or by auto - reduction in a heat treatment. In the present study, metal – filled nanotubes were calcined at 280°C for 6 h in air. The structure directing template nanofibers were reduced to Pt nanoparticles in $SiO_2$ NT as shown by TEM image in Fig. 5.15. Fig. 5.15 (a) shows that abundant Pt metal that was dispersed into the tubes upon reduction. Pt particles of diameter (5 - 10 nm) were embedded in the $SiO_2$ matrix and distributed inside the whole tube wall. The sample was probed by dark field image from TEM (Fig. 5.15 (b)) which displays high amount of Pt incorporated inside the tubes. The tubes further portray thin silica walls (10 nm) with rectangular cross-section (shown in Fig. 5.13 (c)). Since the nanotubes

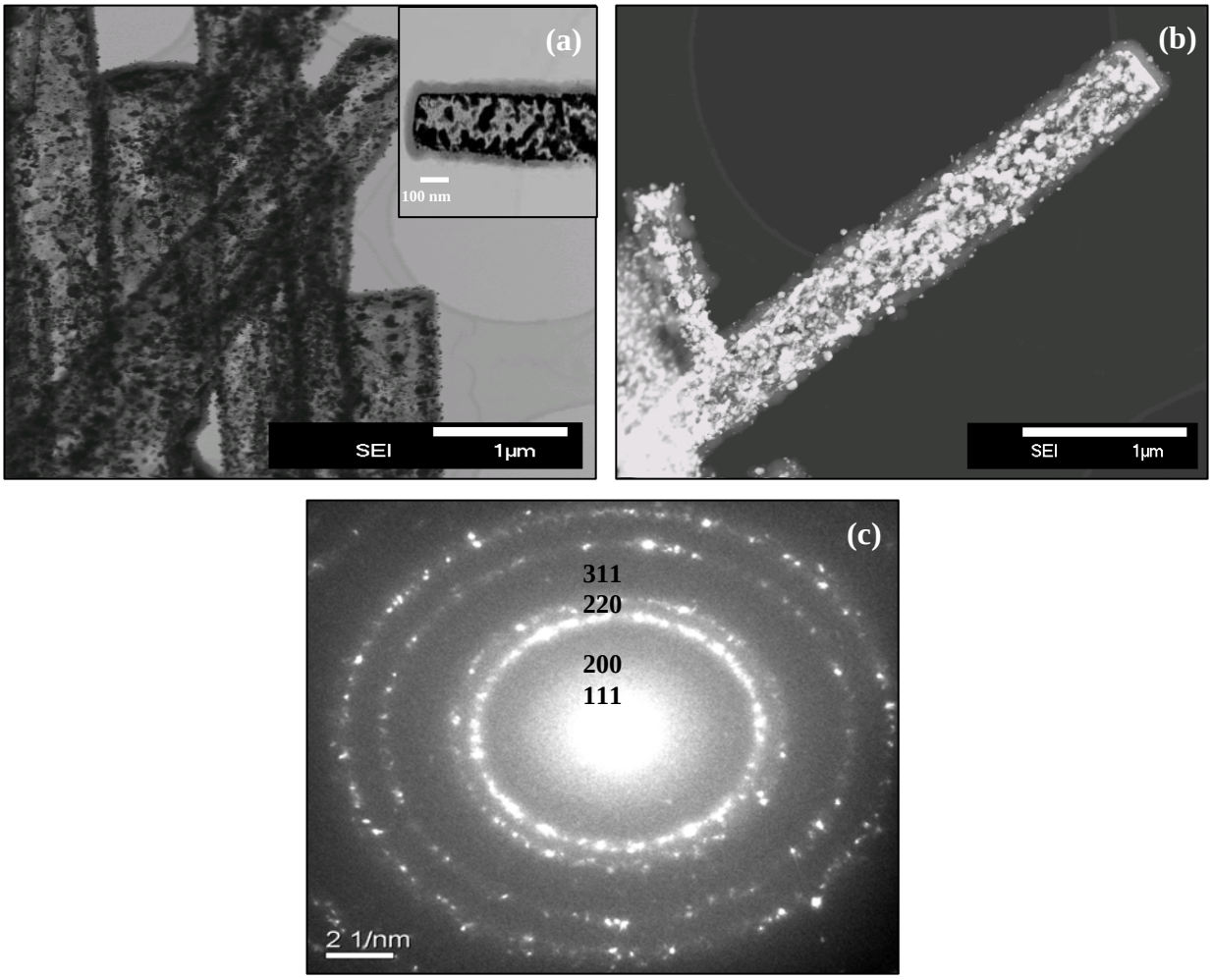


Fig. 5.15 (a) TEM micrograph demonstrating Pt - $SiO_2$ NTs (b) dark field image of a single Pt - $SiO_2$ NT (c) Selected area electron diffraction (SAED) pattern of Pt - $SiO_2$ NTs

possessed rectangular cross section, the density of the Pt metal was found higher along the walls than the interior of the tubes. Pt particles were barely observed in the outer surface of $SiO_2$ NTs.

The SAED pattern shown in Fig. 5.15 (c) was obtained from a 1.2 μm circular region of a nanotube placed over a hole in the carbon support film. The crystallinity of the Pt particles as well as the amorphous $SiO_2$ could be well established from the pattern. It shows Debye-Scherrer rings that could be indexed according to FCC platinum with a lattice constant of a = 3.944 Å which is close to the ideal FCC platinum crystal reported with lattice constant of 3.920 Å [31]. Besides, the diffuse intensities in the background can be attributed to amorphous silica that coats the tubes indicating the amorphous $SiO_2$ forming the walls.

**(iii) TGA analysis**

The thermal decomposition of Pt – $SiO_2$ NTs has been studied by TGA analysis as elucidated in Fig. 5.16. Upon calcination at 280°C, for 6 h in air, the structure directing Pt salt template was reduced to Pt containing $SiO_2$ NTs. The heating rate was chosen to be 1°C/min to compare to the calcination conditions employed. During the calcination process, MGS decomposes according to the reaction (5.1).

$$[Pt(NH_3)_4][PtCl_4] \rightarrow 2Pt + 2N_2 + 4H_2 + 4\,HCl \qquad (5.1)$$

From the TGA curve it can be comprehended that weight loss occurs in two steps. The loss in mass seems to initiate at 90 °C prolonging until 160°C and then becoming intense in the range of 250 – 280 °C. Thereafter the weight loss became less intense without showing any significant weight loss pointing out the complete decomposition of the template. The lower weight loss until 160 °C could be from desorption of the residual water from the micropores. The weight loss from 250 – 280 °C depicts the complete removal of template and dehydration of hydroxyl groups. The weight loss of commercial MGS takes place in the temperature range of 270 – 300°C as portrayed in the TG curve.

According to the ratios in the molecular weight (2Pt: $[Pt(NH_3)_4][PtCl_4]$ = 390 : 598 g/mole) the mass of the pure MGS should decrease by about 33%. The observed mass loss (approx. 35%) could be due to the presence of water molecules in the salt. In the Pt - $SiO_2$ NTs the

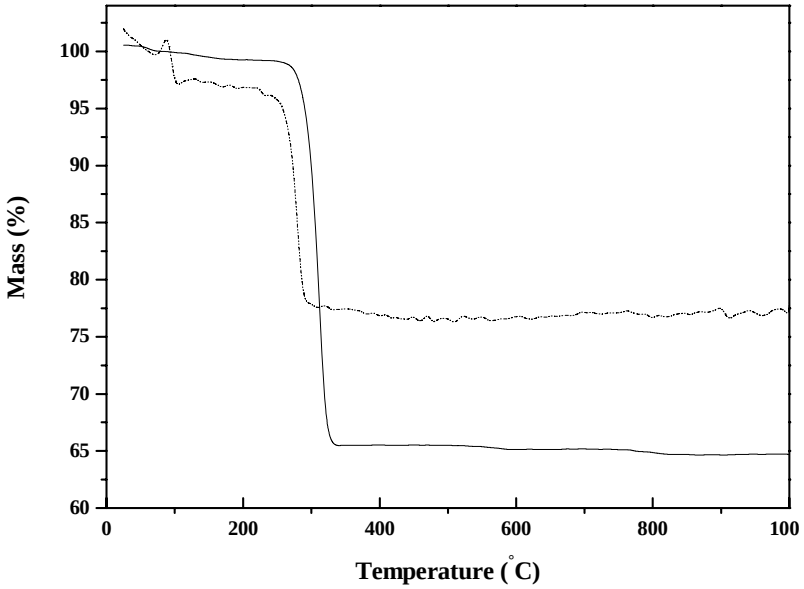


Fig. 5.16 TGA curve of MGS (-) and Pt - $SiO_2$ NTs (---)

weight loss is approximately 23 %. A part of this loss is due to desorption of water. For the sharp decrease in mass observed at 270°C, a mass loss of about 18 % can be deduced. When compared to the 35 % weight loss from pure MGS, this demonstrates that in tubes about 51 wt. - % of Pt particles were encapsulated. The increase in the decomposition temperature of the MGS incorporated in the tubes of about 20°C is another indication for the confinement.

By using the MGS template with Pt salt to TEOS molar ratio of 0.1, $SiO_2$ NTs were synthesized hosting upto 48 - 51 wt.-% of Pt in its interior. In contrast, $SiO_2$ NTs with $[Pt(NH_3)_4](HCO_3)_2$ template, were limited to 40 wt.-% incorporated Pt [14]. The additional presence of Pt in the anion of MGS could be responsible for the higher incorporation of metal inside the tubes at much lower molar ratios of Pt salt.

**(iv) X – ray diffraction analysis**

The powder XRD patterns of commercial MGS, MGS nanofibers, as - synthesized Pt - $SiO_2$ NTs and calcined Pt - $SiO_2$ NTs are illustrated in Fig. 5.17. The XRD pattern of commercial salt, Pt template obtained by the re-precipitation of ethanol shown in Figs. 5.17 (a, b) are almost similar to the XRD pattern of Pt - $SiO_2$ NTs shown in Fig. 5.17 (c). A closer examination indicates that the intensity of diffraction patterns in Fig. 5.17 (c) is slightly decreased when compared to the templating structures and pure salt. This could be because of

the relatively lower crystallinity in Pt – $SiO_2$ NTs (≈ 60 wt.- %) when compared to pure MGS (100 %). Nevertheless, the peak positions are in good agreement with the literature data reported by Atoji et al. [19].

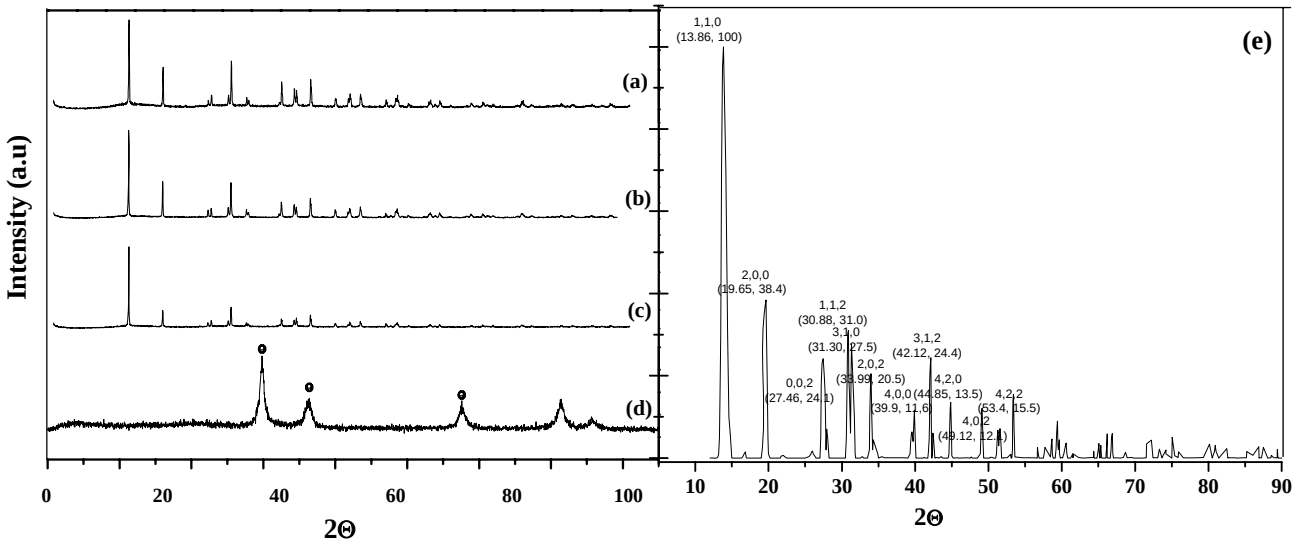


Fig. 5.17 XRD patterns of (a) MGS (b) MGS nanofibers (c) MGS - $SiO_2$ NTs (d) calcined Pt - $SiO_2$ NTs ('0' indicating Pt peaks) (e) XRD pattern simulated from [19]

The XRD pattern obtained from the calcination of as – synthesized Pt – $SiO_2$ NTs was shown in Fig. 5.17 (d). The diffraction pattern is identical to the metallic platinum. The reflection of crystalline platinum (annotated as 0 in (d)) fit well in the literature plot [32] and proves the presence of Pt metal nanoparticles inside the amorphous framework of $SiO_2$. The diffractograms are in accord with the dark field TEM shown in Fig. 5.15 (b) wherein the Pt nanoparticles are found to be well dispersed in the $SiO_2$ matrix. The absence of $SiO_2$ peaks in (d) can be attributed to its transformation into amorphous phase.

**(v) EDXS analysis**

Fig. 5.18 represents the EDX spectrum of Pt – $SiO_2$ NTs. The presence of Pt and Si metals are ensured from the EDX analysis as well as from the mapping images shown in Fig. 5.19. Fig. 5.19 (a) shows the SEM image of single tube of Pt – $SiO_2$ NTs sample. In order to study the presence of elemental analysis along the nanotube, mapping was performed along the selected area. Figs. 5.19 (b, c, d) show the mapping images from Pt, Si and Cu respectively. Copper metal detected both in the spectrum as well as in the mapping images is obviously from the

specimen holder. Furthermore, elemental analysis by EDXS yields a Si/Pt ratio of 1:10 in the tubes.

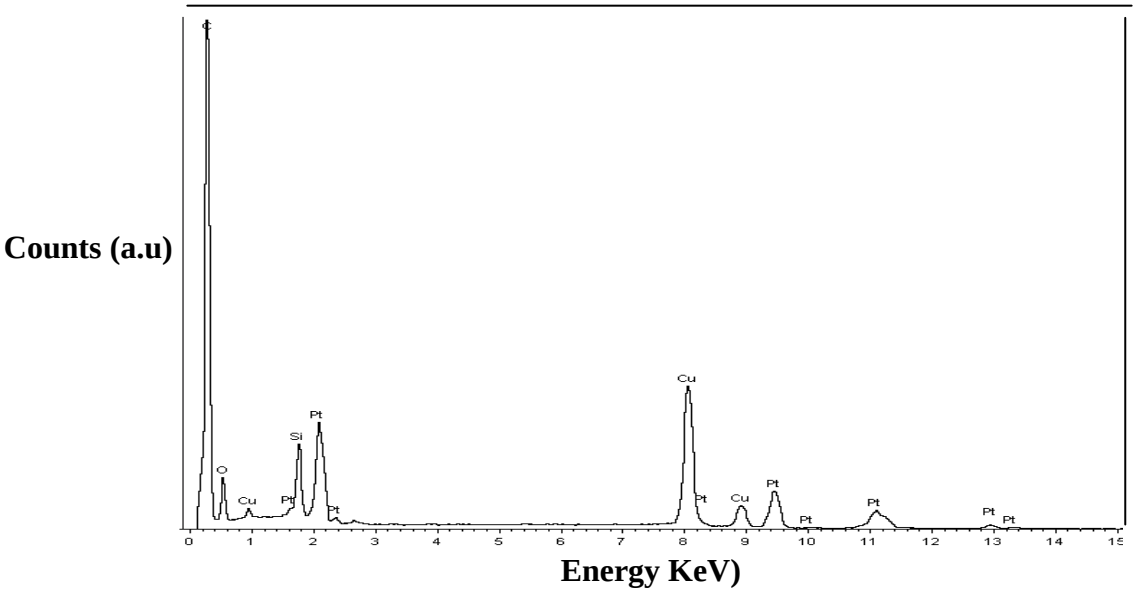


Fig. 5.18 Energy dispersive X - ray spectrum (EDX) of Pt – $SiO_2$ NTs

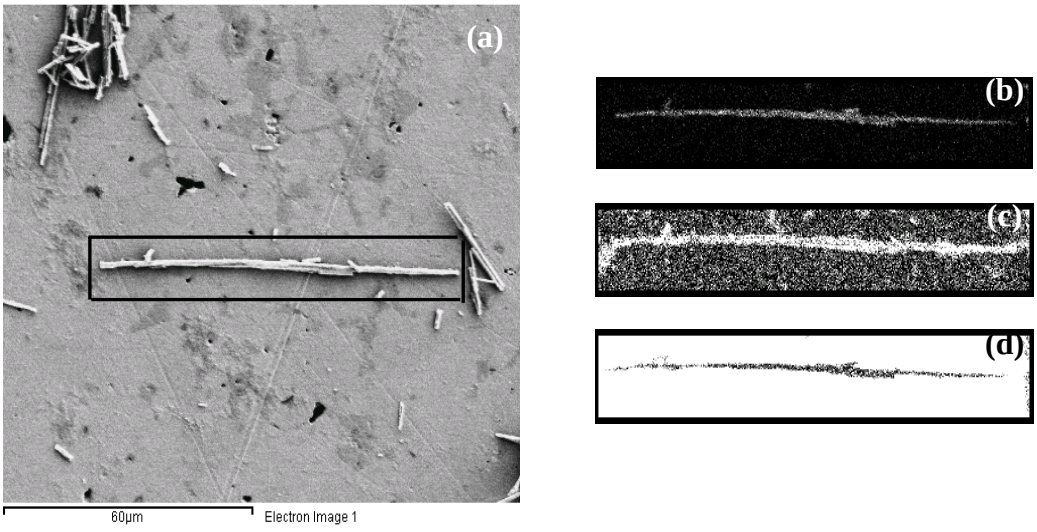


Fig. 5. 19 (a) SEM image of Pt – $SiO_2$ NTs and mapping images confirming the presence of (b) Pt metal (c) Si (d) Cu respectively

### 5.3.4 Conclusions

The results presented here exhibit that the proposed approach can be generalized to embed $SiO_2$ nanotubes with a high population of noble - metal nanoparticles. Since Pt nanoparticles can serve as primary catalysts, $SiO_2$ NTs arranged in a linear geometry may find applications in areas such as catalysis. For e.g. Qian et al. [33] reported that Pt confined $SiO_2$ NTs act as good catalysts in conversion of CO to $CO_2$ at low temperatures. Apart from acting as catalyst supports, Pt – $SiO_2$ NTs are expected to have their extensive applications in gas - selective adsorption, direct heterogeneous catalysis and bioseparation media.

## 5.4 Pt – $TiO_2$ NTs

### 5.4.1 Introduction

$TiO_2$ nanotubes are one of the most sought after nanostructures among the transition metal oxides because of their larger surface area and higher photocatalytic activity [34]. These unique properties of nanoscale tubular $TiO_2$ materials make them applicable in great expanse as described in section 4.4. Owing to the increase in catalytic, photocatalytic activity and sensing performance with Pt metal trapped inside $TiO_2$ NTs, the necessity to synthesize Pt – $TiO_2$ NTs by a simple approach especially at low temperatures becomes a challenging task.

In an attempt to synthesize $TiO_2$ NTs by simultaneously filling with Pt metal, the templating fibers from $Pt(NH_3)_4(HCO_3)_2$ salt were investigated. However the results as demonstrated in section 4.4.3 indicate that no tubular morphologies were observed inspite of varying prominent reaction parameters, instead the fibers from $Pt(NH_3)_4(HCO_3)_2$ salt seem to have transformed into amorphous particles with addition of either of the titanium alkoxides namely Tetrabutylorthotitanate (TBOT) and Titanium isopropoxide (TIP).

The present study investigates the synthesis of Pt – $TiO_2$ NTs employing fibers from MGS as templating structures. By tuning the hydrolysis rate of titanium alkoxide, Pt – $TiO_2$ NTs with an average diameter of 500 nm and lengths in the broad range of 4 - 15 μm were produced from templating fibers of MGS. The tubes not only exhibited well defined morphology but also a high loading of Pt (44 - 48 wt. - %) inside the tubes was detected. Shorter reaction time

and synthesis at lower temperatures are the other advantages of the synthesis strategy reported in this work.

### 5.4.2 Experimental details

#### (i) Chemicals used

Reagents used in the synthesis of Pt - $TiO_2$ NTs include Tetraamineplatinum tetrachloroplatinate (MGS) (97%, Aldrich), Titanium isopropoxide (TIP) (97%, Aldrich), Tetramethyl ammonium hydroxide (TMAOH) (25%, Aldrich), Tetraethyl ortho silicate (TEOS) (98%, Aldrich), isopropanol (99.9%, Merck), $H_2O$ (deionised). All the commercial extra pure reagents were used as received.

#### (ii) Synthesis of well defined Pt - $TiO_2$ NTs

The synthesis of Pt - $TiO_2$ NTs can be categorized into two parts namely (a) Stabilization of TIP (b) Formation of Pt incorporated $TiO_2$ NTs.

#### (a) Stabilization of TIP

The stabilization process of TIP with TMAOH in the presence of water at room temperature was carried out almost similar to the method described in [35] except that the concentrations of the reagents in the present study were altered. 0.05 M TIP was directly dropped into 0.1 M TMAOH solution which resulted in the formation of an opaque colloidal solution. The solution was stirred continuously at uniform stirring speed until it became transparent. The degree of transparency was observed to increase with time. Typically, a clear solution was observed in the range of 96 h – 120 h.

#### (b) Formation of Pt - $TiO_2$ NTs

The present attempt involves synthesis of $TiO_2$ NTs at low temperature. In a typical synthesis, 0.02 g (0.0084 mmol) of MGS was immersed into 2 mL of aqueous ammonia solution (0.4 N) at a stirring speed of 300 rpm. To this mixture, 2 mL of isopropanol was added and the system was placed inside a cold bath maintained at -25$^{\circ}$C for about 10 min. Later, 14 μL of TEOS

was added into the solution and stirred for 2 min followed by the dropwise addition of stabilized TIP solution. After 2 min of vigorous stirring, the stirring rate was increased to 1000 rpm and 0.1 mL of isopropanol was injected swiftly into the mixture. After few minutes, the stirring rate was reduced to 300 rpm and 10 mL of isopropanol was added at a steady rate of 0.5 mL/min. The reaction mixture was aged in the cold bath for 3 h and then allowed to warm up to room temperature for 4 h.

The product thus obtained was rinsed several times in distilled water to wash away undesired impurities. Then the sample was dried overnight at room temperature. The dried samples were calcined at 280°C for 6 h at a heating rate of 1°C/min in air. The calcined samples were dissolved in isopropanol and a 10 μL suspension was dropped on a TEM grid for investigation.

### 5.4.3 Results and discussion

#### (i) Stabilization of Titanium alkoxide

As discussed in section 4.4.3, titanium alkoxides manifest higher rates of hydrolysis and greater speeds of condensation in the presence of large amount of water when compared to TEOS. Hence controlling the hydrolysis rate of titanium alkoxide (TIP in the present case) becomes essential together with appropriate reaction conditions to favour high yield of Pt - $TiO_2$ NTs.

The chemical modification of titanium alkoxides with stabilizers is a well - known procedure in the sol – gel processing of such precursors whose role is to stabilize the alkoxide molecule against uncontrolled hydrolysis upon water addition. β - diketones in particularly acetylacetone is often used to stabilize metal alkoxides towards hydrolysis reactions [36]. Jiang et al. [37] observed that glycolate precursors are resistant to form precipitates even when left open to air for long period of time.

In the present study the alkoxide precursor was coupled with TMAOH which resulted in a colorless clear solution without any formation of dense colloidal species. The experimental results from Ohya et al. [35] suggest that titanic acid, derived from the hydrolysis of TIP

undergoes acid - base reaction with amines to yield alkyl ammonium titanates. The reaction schemes are proposed as shown in Eq. (5.1) and Eq. (5.2).

Hydrolysis reaction:

$$Ti(OCHR_2)_4 + 3\,H_2O \rightarrow \underset{\text{(titanic acid)}}{H_2TiO_3} + 4\,CHR_2OH \qquad (5.2)$$

Acid – Base reaction:

$$H_2TiO_3 + 2\,R_4NOH \rightarrow [R_4N]_2[TiO_3] + 2\,H_2O \qquad (5.3)$$

Where R – $CH_3$

The formation of clear aqueous titanate solution was found to be merely dependant on the basicity of the solution. With a strong base like TMAOH (pH >12), neutral alkyl ammonium titanates result while for weak basic solutions, amorphous precipitates are expected to form.

**(ii) Structural characterization of Pt - $TiO_2$ NTs with SEM**

From section 5.2.3, dissolution of MGS structures in aqueous ammonia solution followed by re – precipitation with alcohol yielded uniform nanofibers with lower size distribution (Fig. 5.2 (b)). During the re - precipitation process, the addition of isopropanol similar to ethanol lead the MGS in the aqueous solution to concentrate forming building blocks (ions). These ions aggregate to form nuclei through homogenous nucleation and start to grow anisotropically due to the differences in the surface energies of their faces. The regular geometric forms displayed by the MGS fibers after solvent modification indicate its internal periodicity. MGS structures when dispersed in ammonia solution were sparingly soluble. Hence, the undissolved fraction of salt was separated and the dissolved fraction of MGS structures in solution was utilized also for the present study so as to have uniform formation of nanostructures.

Fig. 5.20 illustrates topological SEM images of formed Pt - $TiO_2$ NTs whose morphology is determined by the crystal shapes of the template complexes as shown in Fig. 5.2 (b). From the SEM images (Fig. 5. 20 (a, b)) it is evident that the tubular structures are well crystalline tubes with lengths in the broad range of 4 - 15 µm. It is also note worthy to mention that the samples possess high yield of Pt - $TiO_2$ NTs with no significant traces of impurities which is typically observed during synthesis of $TiO_2$ NTs. The particles on the tubes could have been due to the condensation of $TiO_2$ on the template fibers which cannot be avoided completely. Fig. 5.20 (c) shows that the tubes possess rectangular cross - section with the tube ends being

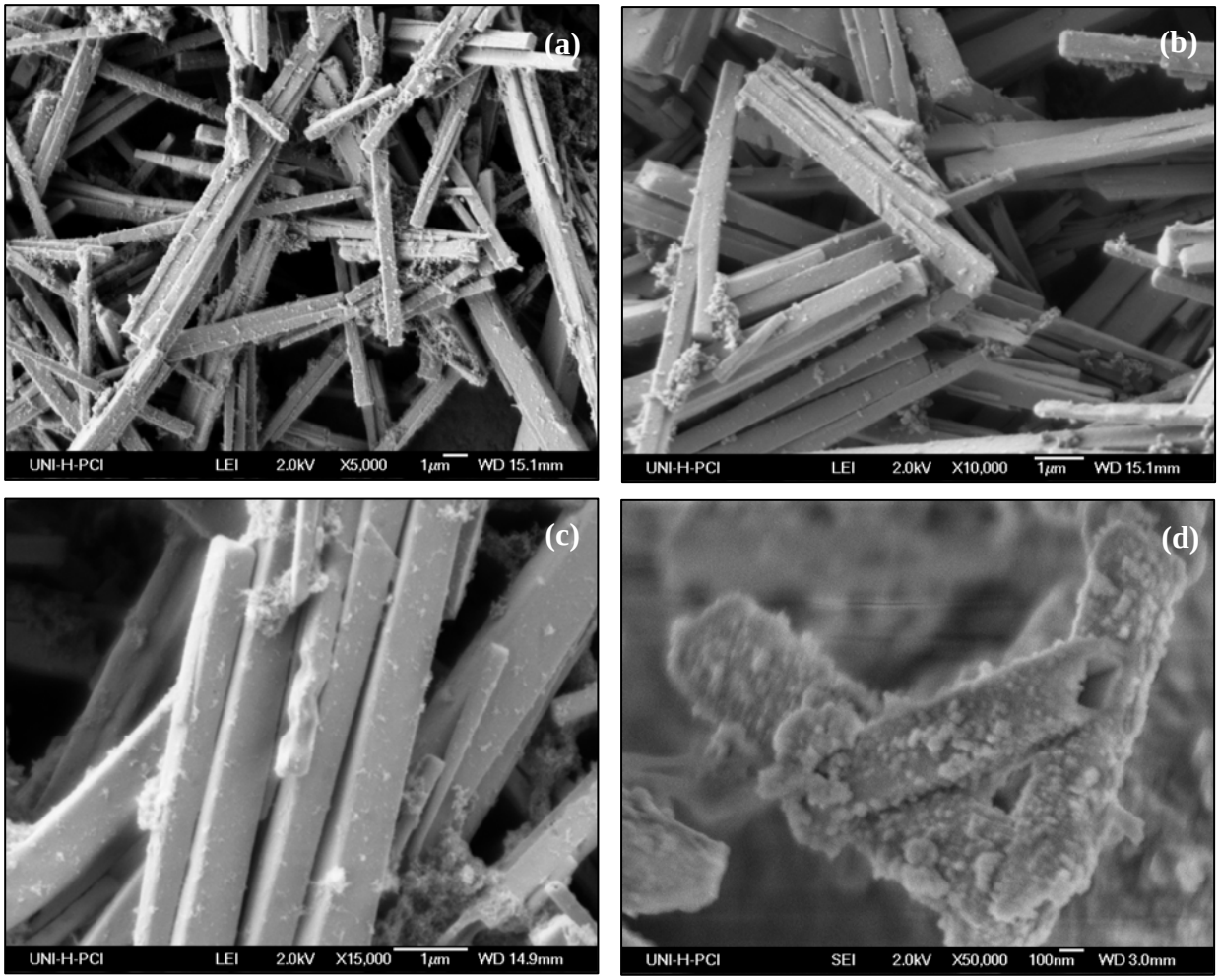


Fig. 5.20 SEM images of (a, b) Pt - $TiO_2$ NTs showing uniform tubes with diameter in the range of 300 – 700 nm at lower and higher magnification respectively (c) High magnification image depicting closed ends of tubes (d) Image depicting the thickness of the tubes (80 nm) at higher magnification

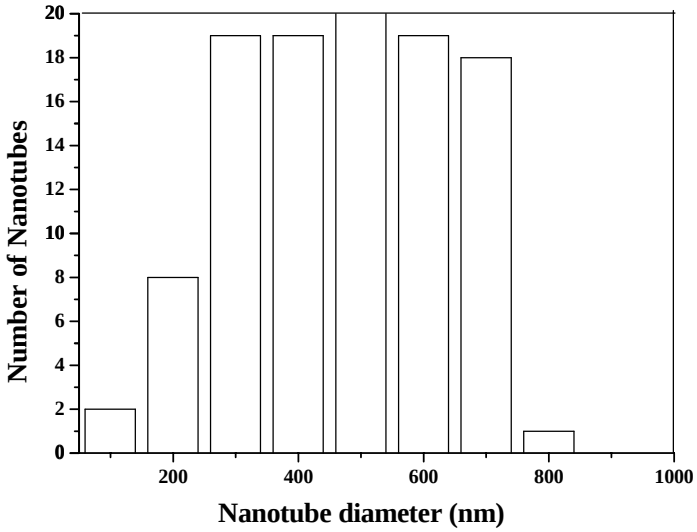


Fig. 5.21 Histogram plot of Pt - $TiO_2$ NTs with diameter of nanotubes distribution (number of nanotubes in a given diameter class versus nanotube diameter)

mostly closed. In order to study the thickness of the tubes, the as-synthesized Pt - $TiO_2$ NTs were slightly milled in a mortar and observed through scanning electron microscopy which showed that the tubes had a wall thickness of 80 nm (Fig. 5.20 (d)). The tubes were distinctlythicker than the Pt – $SiO_2$ NTs synthesized from MGS fibers as shown in section 5.3. The intense increase in the tube thickness could be attributed to the adequate coating of TIP on the tube wall after the formal coating process with TEOS. A histogram plotted with diameter of tubes over their number is shown in Fig. 5.21.

From the Fig. 5.21 it can be concluded that most of the nanotubes in a typical batch of Pt - $TiO_2$ NTs are within the diameter range of 300 - 700 nm. Following the control growth mechanism as described in section 4.2.3, capping agents were also used in the present synthesis study to hamper the aggregation of primary nanofibers resulting from aqueous solution of MGS. As reported by Caruso et al. [38] suitable coatings are likely to increase a material's thermal, mechanical, or chemical stability, increase wear protection, durability or lifetime, decrease friction or inhibit corrosion, change the overall physicochemical and biological properties of the material. Similar to the coating technique applied in case of Pt – $SiO_2$ NTs synthesized from MGS fibers, in the present study too, TEOS was used to avoid the aggregation of fibers which also promoted in anisotropic growth of the Pt – $TiO_2$ NTs. In the

present study, it was observed that TEOS not only acted as a capping agent but also served as a protective layer for the MGS nanofibers avoiding thermal and drying stresses.

As postulated earlier, in the alkaline medium, TEOS undergoes intensive hydrolysis in the ambience of ammonia solution, ethanol (isopropanol) and water giving rise to silanol monomers. The silanol monomers would be deprotonated under the basic conditions and are therefore mutually repulsive and relatively stable according to the DLVO theory explained in chapter 2. The negatively charged silicate monomers from TEOS might behave as electron donors and form hydrogen bonds with the $NH_3$ ligands of the cationic $Pt^{2+}$ complex in the MGS. Owing to such coulomb forces of attraction with the template, silanol molecules would adsorb on the surface of the template and subsequently the follow - up adsorbates (TEOS monomers) deposit on the first layer resulting in the formation of -Si-O-Si- bonds by rapid condensation. An adsorptive layer of silica species is simultaneously attached at the lateral faces perpendicular to the face at which the crystal growth proceeds. In the second step the condensation of titanium isopropoxide (TIP) on the hydrolyzed silica precursor might lead to the formation of Ti-O-Si bond according to equation (5.4) [39] consequently generating thicker walls.

$$\geq Ti - OR + HO-Si \leq \longrightarrow \geq Ti-O-Si \leq + ROH \qquad (5.4)$$

TIP undergoes rapid hydrolysis with the addition of water. Delattre et al. [40] observed in his work that the different rates of hydrolysis of silicon and titanium alkoxide can cause phase separation during sol - gel processing. Hence, TIP was modified by chelating agent such as TMAOH which makes former less reactive before reacting to pre - hydrolyzed silicon ethoxide. The alkoxy groups are then substituted by chelating ligands which are eventually removed upon hydrolysis. The group of Pickup et al. [41] noticed that such stabilized TIP forms a stronger bonding of Ti-O-Si compared to a sample without modification.

**(iii) Characterization with TEM and EDXS**

In order to further probe the influence of stabilized TIP in the synthesis approach, Pt - $TiO_2$ NTs were calcined at 280°C for 6 h at a rate of 1°C/min in air and investigated by TEM and EDXS measurements. The TEM results shown in Fig. 5.22 are consistent with the earlier SEM observations. The tube ends are rectangular in structure. The black part in the tubes was

identified to be agglomerated Pt particles by EDX analysis formed by the decomposition of MGS fibers during heat treatment. Furthermore, the wall of the tube observed was very thin with the sample collected after a hydrolysis time of 2 min as shown in Fig. 5. 22 (a). By prolonging the hydrolysis time to 20 min the walls distinctly became thicker (20 – 30 nm) as shown in Fig. 5.22 (b). Moreover, the addition of TEOS in the mixture seems to have enhanced the strength of the gel structure thereby helping in increasing resistance to the thermal stress as absence of $SiO_2$ led to the deformation of the tubes at high temperatures. Experimental results showed that the absence of TEOS led to the formation of the amorphous particles at higher temperatures.

An isolated Pt – $TiO_2$ NT from a calcined sample was investigated by EDXS. The samples without stabilizing TIP displayed no traces of titanium when compared to the samples with TIP as shown from elemental analysis in Table 5.2. EDX spectra with stabilized TIP further showed a significant peak of titanium in the EDX spectrum thus supporting the stronger bond formation of Ti-O-Si (Fig. 5.23). Further inspection on the EDX analysis from Fig. 5.23 ensures the presence of metals such as platinum and chlorine obtained from the MGS template apart from Ti and Si. Disregarding the possible existence of undetectable lighter elements such as H in the sample, the $TiO_2$ nanotubes may be concluded to be composed of mainly Ti, Si and Pt. The elemental analysis also discloses that the tube stabilized with TIP contains 44 wt. - % of Pt metal incorporated inside the $TiO_2$ NTs.

| **Spectra of single $TiO_2$ NT** | **C (wt.%)** | **O (wt.%)** | **Pt (wt.%)** | **Si (wt.%)** | **Ti (wt.%)** |
|---|---|---|---|---|---|
| **$TiO_2$ NT without TIP** | 21. 78 | 35.13 | 40.14 | 2.84 | 0.11 |
| **$TiO_2$ NT with TIP** | 18.14 | 23.99 | 44.82 | 3.16 | 9.89 |

Table 5.2 Elemental analysis of a single calcined Pt - $TiO_2$ NT obtained from EDXS

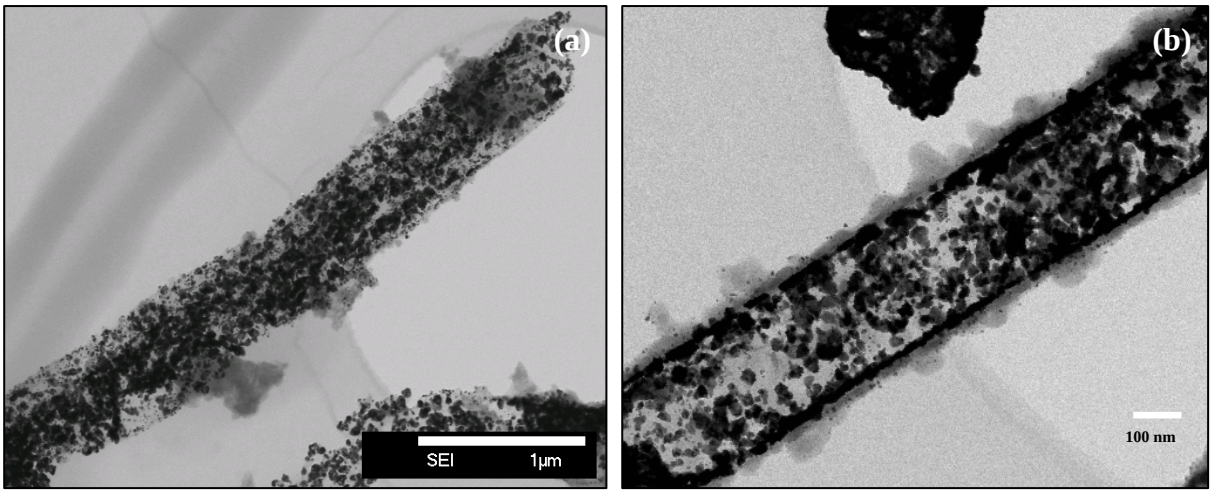


Fig. 5.22 TEM images of Pt - $TiO_2$ NTs with time of hydrolysis (a) 2 min (b) 20 min

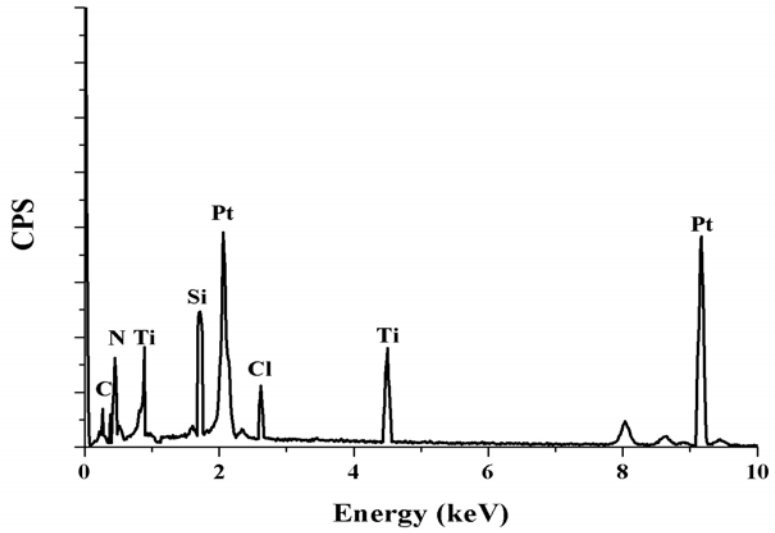


Fig. 5.23 EDX spectrum of Pt - $TiO_2$ NTs stabilized with TMAOH (Ti/Si = 0.15)

**(iv) TGA analysis**

The thermal decomposition of Pt - $TiO_2$ NTs was further analyzed by TGA as shown in Fig. 5.24. The calcination was performed at 280°C, for 6 h in air to reduce the structure directing MGS templating fibers into Pt - $TiO_2$ NTs. The heating rate was chosen to be 1°C/min to compare to the heat treatment in the actual process. During the calcination process, MGS template decomposes according to the reaction shown in Eq. 5.1.

During the heat treatment, gases such as $N_2$, $H_2$, HCl and $NH_3$ are released which escape through the porous walls of the tube. As shown in the Fig. 5.24, from the TGA curve it can be

perceived that weight loss curves are similar to the result from Pt – $SiO_2$ NTs. The weight loss occurs in two steps. The loss in mass seems to originate at 80 °C prolonging until 120°C and then becoming intense around 280 °C. After that, the weight loss became less acute without showing any significant weight loss pointing out the complete decomposition of the template. The lower weight loss until 120 °C could be from desorption of the water molecules from the micropores. The weight loss at 280 °C illustrates the complete removal of template and dehydration of hydroxyl groups. On the other hand, it can be noted that the weight loss of commercial MGS takes place in the temperature range of 270 – 300°C as portrayed in the TG curve.

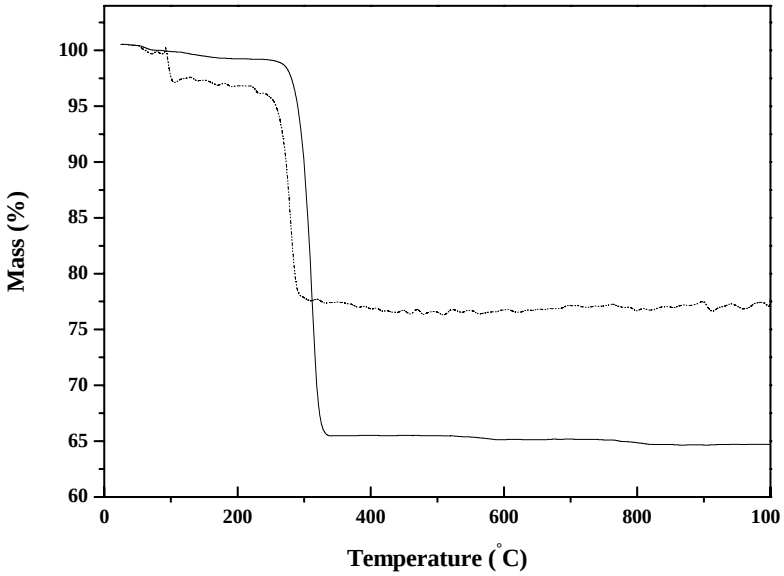


Fig. 5.24 TGA curve of MGS (-) and Pt - $TiO_2$ NTs (--)

According to the ratios in the molecular weight (2Pt: $[Pt(NH_3)_4][PtCl_4]$ = 390 : 598 g/mole) the mass of the pure MGS should decrease by about 33%. The observed mass loss (approx. 35%) from Fig. 5. 24 could be due to the presence of water molecules in the salt. In the Pt-doped $TiO_2$ NTs the weight loss is approximately 24 %. A part of this loss (about 5 mass %) is due to the dehydration of inter - tunnel water. For the sharp decrease in mass observed at 290°C, a mass loss of about 17 % can be deduced. When compared to the 35 % weight loss from pure MGS, it can be concluded that 48 wt. - % of Pt particles were encapsulated inside the tubes which is in consistent to the value from EDX analysis.

**(v) Crystallinity of Pt – $TiO_2$ NTs**

XRD measurements were performed to study the structure of the tubular Pt – $TiO_2$ materials. Fig. 5.25 (a) represents the X - ray diffraction analysis of the as - prepared Pt - $TiO_2$ NTs. The XRD pattern was similar to the MGS template and agrees to the peak positions in literature [42] as shown in our earlier work though the intensities of peaks are slightly lower. The suppression of peak intensities could be due to the mild dispersion of the Pt template into the TIP coating. Fig. 5.25 (b) is the XRD profile taken for the Pt - $TiO_2$ NTs calcined at a temperature of 280°C. The peak positions were slightly shifted probably because of the inter-tunnel water retained in as - prepared tubes. The sample exhibits a pure rutile phase (JCPDS File No**:** 4-0551) with increase in crystallinity. It can also be inferred that the mobility of Pt clusters enhanced at this temperature leading to the aggregation of Pt particles inside the tube. The diffraction patterns look similar to the layered trititanate nanotubes reported by Peng et al. [43] wherein single sheets are rolled - up into cylindrical geometry though such formation mechanism is likely to be observed in case of hydrothermal synthesis methods that involves large amount of water.

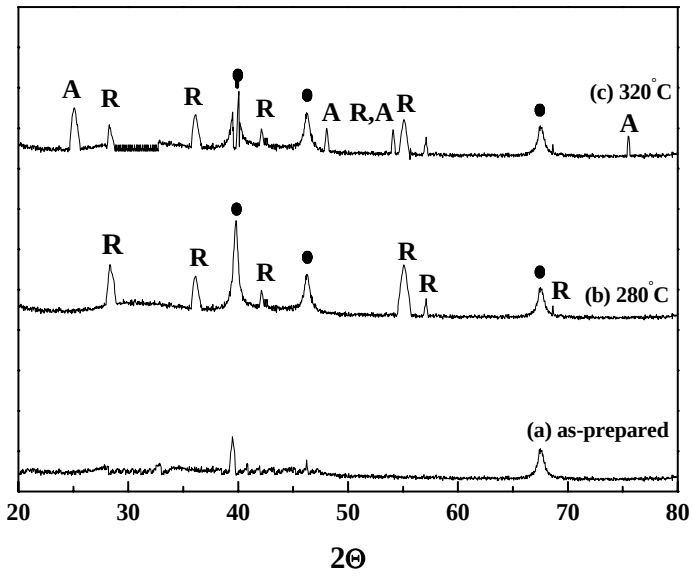


Fig. 5.25 XRD patterns of (a) as-prepared Pt - $TiO_2$ NTs (b) Pt - $TiO_2$ NTs calcined at 280°C (c) Pt - $TiO_2$ NTs calcined at 320°C. The peaks labelled A, R and **.** are anatase, rutile and Pt respectively

However when the temperature was slightly increased to 320 °C, a mixture of rutile and anatase phase (JCPDS File No: 21-1272) was observed as shown in Figure 5.25 (c) explaining the phase transition. By slightly elevating the temperature to 350°C, anatase phase ceased and the nanotubes were deformed mostly into nanoparticles indicating the loss of crystallinity at higher temperatures. $TiO_2$ materials synthesized with only TIP in absence of template molecules in an isopropanol environment resulted in anatase phase of $TiO_2$ [44]. Hence in the present scenario the rutile phase of Pt – $TiO_2$ NTs indicate that MGS template fibers play a prominent role for the formation of rutile structure during hydrolysis process. Conventional transformation of anatase phase to rutile phase is observed at a temperature around 1000°C for crystalline titania materials [45]. On the contrary the present study shows that a rutile structure was achieved at much lower temperatures.

On increasing the temperature to 320°C, the XRD pattern of Pt – $TiO_2$ NTs indicates a phase transformation and gradually forms amorphous particles indicating the loss of crystallinity. An apparent possibility could be that the templating fibers from MGS were not dispersed into the coating matrix and due to the quantum size effects evolving from the coating matrix, when the template filled tubes were subjected to heat treatment (280°C), a stable phase namely a rutile phase would have been achieved. The Pt template fibers would have been reduced to Pt metal atoms and form aggregates inside the composites. However higher temperatures led to the deformation of the template structures thereby forming amorphous particles. Hence no dispersion through the walls was noticed in TEM images (Fig. 5.22). Nevertheless the tubular morphology of the tubes attributed to the Pt particles to distribute along the walls of the tubes enhancing the surface properties. Another noteworthy conclusion that could be drawn is that the presence of TEOS in the mixture not only reduced thermal stresses but also drying stresses that result with the evaporation of solvent. S. R. Kumar et al. [35] also reported that addition of Si to TIP reduced drying stress as well as improved the surface area. They realized that the presence of less polar solvents such as ethanol forms weaker hydrogen bonds with surface hydroxyl groups thereby reducing strain on the gel structure during drying. Henceforth, the use of isopropanol which is also a less polar solvent could have helped in avoiding drying stresses in our case.

### 5.4.4 Conclusions

The experimental results show that Pt – $TiO_2$ NTs from MGS templating structures reveal diameter in the range of 300 – 700 nm while the lengths ranging from 4 - 15 μm. The tubes depicted well defined morphology with high incorporation of Pt (44 - 48 wt. - %) inside the tubes at significantly lower temperatures (280°C). Tuning of hydrolysis time led to the formation of thicker walls of the tubes (20 - 30 nm).

Rutile phase of $TiO_2$ NTs are preferred in terms of selectivity and improved kinetics in photo - catalytic reactions [46, 47], dielectric constant [48, 49] and refractive index (2.9 for rutile versus 2.4 for anatase) for photoelectronic applications [50]. A plausible explanation for the preference of rutile phase in photo - chemical reactions is that the band gap for rutile is smaller than anatase by 0.2 eV. Besides, Varghese et al. [51] in an attempt to transform anatase into rutile nanotubes by heat treatment reported that tubular morphology the collapsed with loss of structural control. Owing to all these advantages of the rutile structure of Pt - $TiO_2$ NTs at lower temperatures, the present synthesis strategy could expect distinct applications in photoelectronics and photocatalysis.

### 5.5 References

[1] J. Bremi, M. Fontana, W. Caseri, P. Smith, *Macromolecular Symposia,* **235** (2006) 80.

[2] J. Bremi, D. Brovelli, W. Caseri, G. Hähner, P. Smith, T. Tervoort, *Chemistry of Materials,* **11**(1999) 977.

[3] J. R. Miller, *Journal of Chemical Society*, (1961) 4452.

[4] W. B. Connick, R. E. Marsh, W. P. Schaefer, H. B. Gray, *Inorganic Chemistry*, **36** (1997) 913.

[5] L. V. Interrante, R. P. Messmer, *Inorganic Chemistry*, **10** (1971) 1175.

[6] S. H. Yamada, R. Tsuchida, *Bulletin of the Chemical Society of Japan*, **31** (1958) 813.

[7] J. R. Miller, *Journal of Chemical Society*, (1965) 713.

[8] B. G. Anex, M. E. Ross, M.W. Hedgcock, *Journal of Chemical Physics,* **46** (1967) 1090.

[9] P. Day, A. F. Orchard, A. J. Thomson, R. J. P. Williams, *Journal of Chemical Physics,* **42** (1965) 1973.

[10] C. N. R. Rao, S. N. Bhat, *Inorganic and Nuclear Chemical Letters*, **5** (1969) 531.

[11] R. Kubota, H. Kobayashi, I. Tsukjikawa, T. Enoki, *International Journal of Quantum Reviews*, **18** (1980) 1533.

[12] K. Honda. K. Chiba, E. Tsuchida, A. J. Frank, *Journal of Materials Science Letters*, **24** (1989) 4004.

[13] M. Fontana, *Ph. D Dissertation*, Eidgenössische Technische Hochschule, Zürich, 2003.

[14] L. Ren, 'Inorganic salt nanofibers as templates for the formation of oxide nanotubes' *Ph.D Thesis*, Leibniz University of Hannover, 2004.

[15] L. Ren, M. Wark, *Chemistry of Materials,* **17** (2005) 5928.

[16] Y. Wang, E. Merino, *Geochimica Et Cosmoschimica Acta*, **54** (1990) 1627.

[17] P. J. Heaney, D. R. Veblen, J. E. Post, *American Mineralogist*, **79** (1994) 452.

[18] G. Miehe, H. Graetsch, O.W. Flörke, *Physics and Chemistry of Minerals*, **10** (1984) 197.

[19] M. Atoji, J. W. Richardson, R. E. Rundle, *Journal of the American Chemical Society,* **79** (1957) 3017.

[20] L. Wang, S. Tomura, F. Ohashi, M. Maeda, M. Suzuki, K. Inukai, *Journal of Materials Chemistry,* **11** (2001) 1465.

[21] F. Miyaji, S. A. Davis, J. P. H. Charmant, S. Mann, *Chemistry of Materials,* **11** (1999) 3021.

[22] W. Stöber, A. Fink, E. Bohn, *Journal of Colloid and Interface Science*, **26** (1968) 62.

[23] C. J. Brinker, G. W. Scherer, *Sol – gel Science: The Physics and Chemistry of Sol – gel Processing*, Academic Press, 1st Edition, **240** (1990).

[24] Y. Sun, B. Gates, B. Mayers, Y. Xia, *Nano Letters,* **12** (2002) 165.

[25] Y. Yin, Y. Lu, Y. Sun, Y. Xia, *Nano Letters,* **2** (2002) 427.

[26] X. Peng, L. Manna, W. Yang, J. Wickham, E. Scher, A. Kadavanich, A. P. Alivisatos, *Nature,* **404** (2000) 59.

[27] V.F. Puntes, K.M. Krishnan, A.P. Alivisatos, *Science,* **291** (2001) 2115.

[28] Y. G. Sun, Y. N. Xia, *Advanced Materials,* **16** (2004) 264.

[29] W. S. Shi, H. Y. Peng, N. Wang, C. P. Li, L. Xu, C. S. Lee et al, *Journal of the American Chemical Society,* **123** (2001) 11095.

[30] P. Hartman, P. Bennema, *Journal of Crystal Growth,* **49** (1980) 145.

[31] N. Lümmen, T. Kraska, *Nanotechnology,* **16** (2005) 2870.

[32] (a) E. Brandes, G. Brook (Eds.), *Smithells Metals Reference Book*, Butterworth - Heinemann, London, 7th ed.,1992, pp. 6- 9 (b) H. S. Qian, M. Antonietti, S. H. Yu, *Advanced Functional Materials,* **17** (2007) 637.

[33] H. S. Qian, M. Antoniette, S. H. Yu, *Advanced Functional Materials*, **17** (2007) 637.

[34] M. Adachi, Y. Murata, M. Harada, *Chemistry of Letters,* **8** (2000) 942.

[35] T.Ohya, A. Nakayama, T. Ban, Y. Ohya, Y. Takahashi, *Chemistry of Materials,* **14** (2002) 3082.

[36] C. Sanchez, J. Livage, M. Henry, F. Babonneau, *Journal of Non – Crystalline Solids,* **100** (1998) 65.

[37] X. Jiang, T. Herricks, Y. Xia, *Advanced Materials,* **15** (2003) 1205.

[38] R. A. Caruso, M. Antoniette, *Chemistry of Materials,* **13** (2001) 3272.

[39] S. Rajesh Kumar, C. Suresh, A. K. Vasudevan, N. R. Suja, P. Mukundan, K. G .K. Warrier, *Materials Letters,* **38** (1999) 161.

[40] L. Delattre, F. Babonneau, *Chemistry of Materials,* **9** (1997) 2385.

[41] D. M. Pickup, G. Mountjoy, G. W. Wallidge, R. Anderson, J. M. Cole, R. J. Newport, M. E. Smith, *Journal of Materials Chemistry,* **19** (1999) 1299.

[42] M. Atoji, J. W. Richardson, R. E. Rundle, *Journal of the American Chemical Society,* **79** (1957) 3017.

[43] S. Zhang, Q. Chen, L.-M. Peng, *Physical Review B,* **71** (2005) 014104.

[44] Y. Sato, M. Koizumi, T. Miyao, S. Naito, *Catalysis Today*, **111** (2006) 164.

[45] T. Mitsuhashi, O.J. Klippa, *Journal of the American Ceramic Society,* **62** (1979) 356.

[46] O. Carp, C. L. Huisman, A. Reller, *Program (Solid State Chemistry),* **32** (2004) 33.

[47] A. R. Gandhe, J. B. Fernandes, S. Varma, N. M. Gupta, *Journal of Molecular Catalysis A : Chemical,* **238** (2005) 1 -2, 63 – 71.

[48] U. Diebold, *Surface Science Reports,* **48** (2003) 53.

[49] D. Eder, R. Kramer, *Journal of Physical Chemistry B*, **108** (2004) 14823–29.

[50] V. N. Manoharan, A. Imhof, J. D. Thorne, D. J. Pine, *Advanced Materials*, **13** (2001) 447.

[51] O.K.Varghese, D. Gong,M. Paulose, C.A.Grimes, E. C. Dickey, *Journal of Materials Research*, **18** (2003) 156.

# 6

# 6. Conclusions and Future Outlook

## 6.1 Conclusions

Nanostructures of tubular morphology provoked great interest among researchers because of their distinctive properties and wide variety of applications in catalysis [1, 2], sensing [3, 4], as gas storage materials [5] and in nanoscale electronic and optical devices such as transistors, light emitting devices [6] etc.. The dimension and the size distribution of the nanostructured materials play the key parameters in tailoring the properties for these applications. Hence a synthesis strategy for tubes with nanometer precision and monodisperse diameter together with well defined morphology remains a challenging task. Apart from synthesizing pure oxide nanotubes, filling the tubes with metals has become an intriguing part of research owing to their extensive applications proposed in catalysis, separation and in development of novel functional materials with improved properties.

In view of developing a synthesis process that facilitates both the synthesis as well as incorporating metal particles into oxide nanotubes, fibers from metal salts as templating structures was investigated as part of this thesis. Fibers from salts such as $[Pt(NH_3)_4(HCO_3)_2]$ and $[Pt(NH_3)_4][PtCl_4]$ namely MGS were examined to synthesize $SiO_2$, $TiO_2$ and $SnO_2$ nanotubes. Experimental results showed that both the Pt – salts can grow into one dimensional fibers upon re – precipitation with solvent (sections 4.2, 5.2). Moreover coating the templating fibers with metal alkoxides by sol – gel technique proved successful under optimized reaction conditions. The ensuing mechanistic investigation on capping agents provided a clear explanation of the phenomenological observations, and led to the conclusion that arresting the aggregation of the intermediate nanofibers plays a key role in synthesizing nanotubes with narrow size distribution (section 5.4.3). Furthermore, the capping agents led to increase in aspect ratios of the tubes promoting the anisotropy and also served as a protective layer for the tubes from drying and thermal stresses (section 4.5.3).

Utilizing fibers from $Pt(NH_3)_4(HCO_3)_2]$ salt, Pt - $SiO_2$, Pt - $TiO_2$ and Pt - $SnO_2$ nanotubes were synthesized in presence of tetraethylorthosilicate (TEOS) as capping agent which gave rise to monodisperse nanotubes with approximately 38 - 40 wt.- % of Pt incorporated inside the tubes. While Pt doped $SiO_2$ nanotubes (Pt – $SiO_2$ NTs) exhibited considerable yield of tubes with diameter in range of 200 – 800 nm and lengths upto 20 µm long as shown in section 4.3, Pt – $SnO_2$ NTs demonstrated short length tubes (2 – 5 µm) with diameter in broad range of 200 – 800 nm in section 4.5. On the other hand, synthesis of Pt – $TiO_2$ NTs under similar reaction conditions failed to produce tubular morphologies and resulted in particles with minute traces of titanium alkoxide from the solution (section 4.4).

Alternatively, templating fibers from $[Pt(NH_3)_4][PtCl_4]$ (MGS) under optimized synthesis conditions resulted in monodisperse and high aspect ratios of Pt - $SiO_2$ NTs (600) and Pt - $TiO_2$ NTs (500) with higher incorporation of Pt (around 48 - 51 wt %) inside the tubes at lower temperatures (280$^{\circ}$C). It is further worthy to point out that synthesis of metal filled nanotubes using MGS as templating structures was performed at lower molar ratios of salt thereby making the synthesis approach a cost effective technique comparatively. The experimental investigation demonstrated nanotubes with a diameter range of 300 – 700 nm and lengths upto 60 µm long for Pt – $SiO_2$ NTs and an average diameter of 500 nm with lengths in the wide range of 4 - 15 µm for Pt – $TiO_2$ NTs was realized from fibers of MGS (sections 5.3 and 5.4).

Pt – $SiO_2$ NTs and Pt – $TiO_2$ NTs synthesized from templating MGS fibers gave higher yield of Pt particles inside the tubes. Apart from acting as catalyst supports, Pt – $SiO_2$ NTs are expected to have their extensive applications in gas - selective adsorption, direct heterogeneous catalysis and bioseparation media while Pt – $TiO_2$ NTs with their high Pt loading are expected to dramatically influence catalytic activity, photocatalytic property and sensing performance. Pt – $SnO_2$ NTs with such high filling of Pt are expected to enhance the sensitivity to different gases and reduce the response time when compared to pure $SnO_2$ structures. Hence, apart from gas sensing, they could be explored in diverse optoelectronic devices.

**6.2 Future outlook**

(i) In the present work, much emphasis was given on the synthesis of narrow size distribution of nanotubes that could load higher amounts of metal with Pt salts such as $Pt(NH_3)_4(HCO_3)_2]$ and $[Pt(NH_3)_4][PtCl_4]$. In future the influence of electric field on coating as well as the metal oxide layer on the conductivity has to be investigated especially for Pt – $TiO_2$ and Pt – $SnO_2$ NTs. Other metal oxides such as $SnO_2$, $In_2O_3$ nanotubes embedded with Pt which are prospective for electrochemical sensing could be synthesized from templating fibers of MGS. Various metal alkoxides which could influence the growth of nanotubes can be checked and optimized in this regard. Apart from metal oxides, doping Pt with metal sulphides such as Pt – $SnS_2$ which can be expected to improve the conductivity could be explored employing fibers from MGS.

(ii) Inorganic species from suitable salts that can be grown into nanofibers by re – precipitation of solvent for the synthesis of oxide nanotubes filled with metals such as Fe, Ni to enhance the magnetic properties can be investigated. From earlier studies it can be noticed that templating structures with structural formula M $(NH_3)_x$ $(HCO_3)_y$ are likely to form fiber morphology [section 4.5.4, 7]. Ammine salts of Fe and Ni such as hexaammine ferrousdichloride $[Fe(NH_3)_6Cl_2]$ and hexaammine nickeldichloride $[Ni(NH_3)_6Cl_2]$ can be converted into the form, $M(NH_3)_6$ $HCO_3$ $CO_3$. 2 $H_2O$ (where M = Fe, Ni) by performing ion – exchange reaction with any strong base anion exchanger e.g. resins like Amberlite IRA – 402. By carefully controlling critical reaction components like pH, hydrolysis and condensation reactions as well as monitoring of the reaction with techniques discussed in this thesis could lead to high content metal incorporated inside nanotubes.

(iii) Alignment of nanotubes for fabrication of novel functional devices especially those relevant to energy storage and conversion such as nanobatteries, nanofuel cells, nanosensors etc. could be investigated. H. Shimoda et al. [8] reported the alignment of single – walled carbon nanotubes (SWCNT) by self assembly process as shown in the schematic diagram in Fig. 6.1. A hydrophilic glass slide was vertically immersed into the stable suspension of SWCNT bundles. With gradual evaporation of water at room temperature, SWNT bundles self - assembled on the glass substrate around the air/water/substrate triple line. As the triple line progressed downwards, a continuous SWCNT film was formed on the substrate. The suspension of Pt – NTs reported in this thesis could be tried for alignment on glass or Si wafer

substrates. Techniques like spin coating and dip coating could also be tried to study the alignment process.

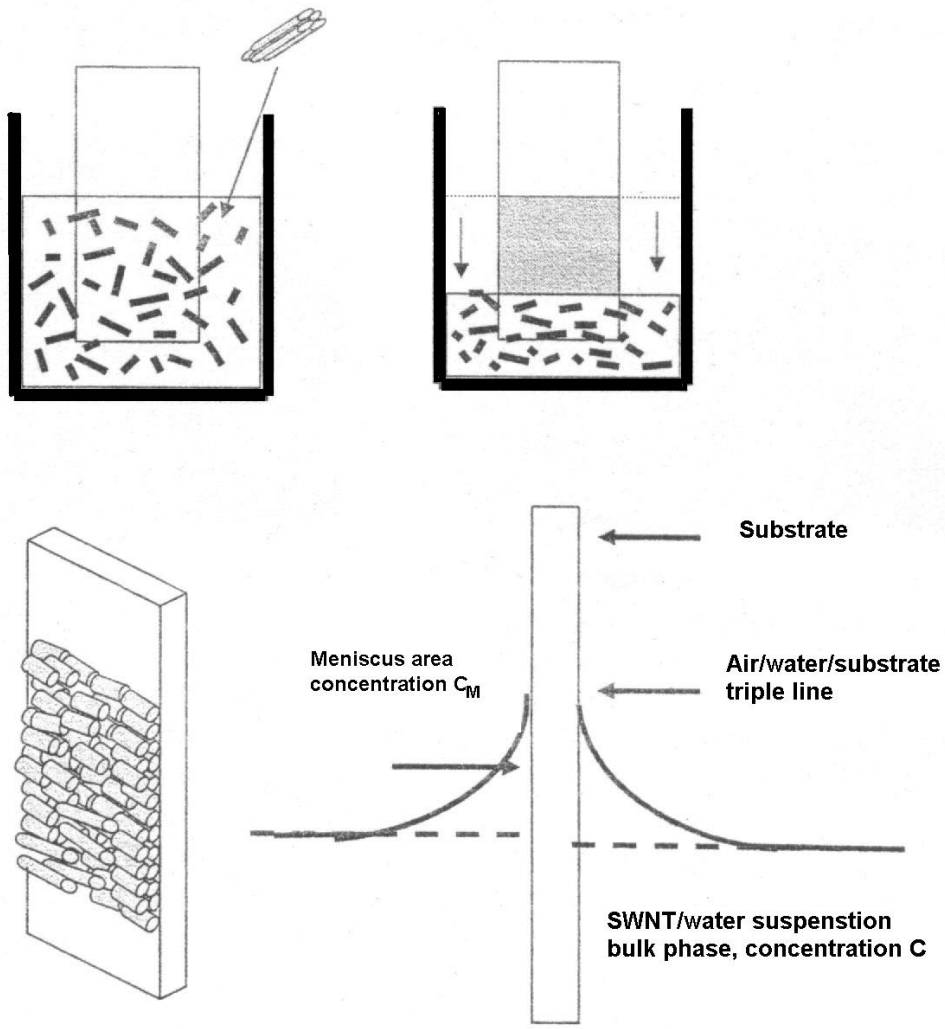


Fig.6.1 Schematic illustration of self assembly process of single – walled carbon nanotubes aligned on a glass substrate

### 6.3 References

[1] B. F. G. Johnson, *Topics in Catalysis*, **24** (2003) 147.

[2] S. Sun, K. Fujimoto, Y. Zhang, N. Tsubaki, *Catalysis Communications*, **4** (2003) 361.

[3] M. Law, H. Kind, F. Kim, B. Messer, P. Yang, *Angewandte Chemie International Edition*, **41** (2002) 2405.

[4] G. Zhang, M. Liu, *Sensors and Actuators B*, **69** (2000) 144.

[5] C. Liu, Y. Y. Fan, M. Liu, H. T. Cong, H. M. Cheng, M. S. Dresselhaus, *Science*, **286** (1999) 1127.

[6] X. F. Duan, Y. Huang, R. Agarwal, C. M. Lieber, *Nature*, **421** (2003) 241.

[7] L. Ren, L. He, C. Chen, M. Wark, C. Li, P. Che, L. Guo, *Journal of Magnetism and Magnetic Materials*, **312** (2007) 405.

[8] H. Shimoda, S. J. Oh, H. Z. Geng, R. J. Walker, X. B. Zhang, L. E. McNeil, O. Zhou, *Advanced Materials*, **14** (2002) 899.

# 7

# 7. Appendices

## 7.1 Nomenclature

| Symbol | Description |
|---|---|
| nm | nanometer ($10^{-9}$ m) |
| µm | micrometer ($10^{-6}$ m) |
| mm | millimeter ($10^{-3}$m) |
| eV | electron volts ($1.60217646 \times 10^{-19}$ Joules) |
| Pt | Platinum |
| Pd | Palladium |
| $SiO_2$ | Silicon dioxide |
| $TiO_2$ | Titanium dioxide |
| $SnO_2$ | Tin dioxide |
| TEOS | Tetraethyl-*ortho*-silicate |
| TBOT | Tetrabutyl-*ortho*-titanate |
| TIP | Tetra-*iso*-propyl-*ortho*-titanate (*Titanium isopropoxide*) |
| RT | Room temperature |
| Approx. | approximately |
| h | hours |
| $^{\circ}C$ | Degree Celsius |
| $MO_2$ | Metal dioxide |
| NTs | Nanotubes |
| NFs | Nanofibers |
| $[Pt(NH_3)_4(HCO_3)_2]$ | *Platinum tetraamine hydrocarbonate* |

| | |
|---|---|
| $[Pt(NH_3)_4][PtCl_4]$ | *Platinum tetraamine tetrachloro - Platinate* |
| CO | Carbon monoxide |
| $Al_2O_3$ | Aluminium oxide |
| H | Hydrogen |
| $Pt – SiO_2$ | Platinum incorporated Silicon dioxide |
| $Pt – TiO_2$ | Platinum incorporated Titanium dioxide |
| $Pt – SnO_2$ | Platinum incorporated Tin dioxide |
| $N_2$ | Nitrogen |
| wt.- % | weight percent |
| AlN | Aluminium nitride |
| MGS | Magnus green salt |
| PBC | Periodic bond chain |
| I | Ionic strength (dimensionless) |
| $k_B$ | Boltzmann constant ($1.38 \times 10^{23}$ $J.K^{-1}$) |
| XRD | X – ray diffraction |
| SEM | Scanning electron microscopy |
| TEM | Transmission electron microscopy |
| SAED | Selected area energy diffraction |
| DNA | Deoxyribonucleic acid |
| ALD | Atomic layer deposition |
| DLVO | Derjaguin, Landau, Verwey and Overbeek |
| TGA | Thermogravimetric analysis |
| EDXS | Energy dispersive X - ray spectrometry |
| ICP | Inductive coupled plasma |

## 7.2 Miscellaneous

### 7.2.1 Publications

**Ultra long $SiO_2$ nanotubes embedded with Pt nanoparticles**

C. Aresipathi, A. Feldhoff, M. Wark, *Journal of Materials Chemistry*, In progress.

**A facile approach for encapsulation of Pt nanoparticles in $SnO_2$ nanotubes**

C. Aresipathi, M. Wark, In process of submission.

**Template assisted synthesis of Pt embedded $TiO_2$ nanotubes**

C. Aresipathi, M. Wark, In process of submission.

### 7.2.2 Posters and Presentations

**Template based fabrication and electrical conductivity of metal doped oxide nanotubes and thin metal nanowires**

M. Wark, C. Aresipathi, I. Bannat, J. M. Becker, R. J. Haug, *DFG Semi – annual meeting*, Bad Honnef, Germany, 02/2005.

**Sol-gel method to synthesize $SiO_2$ & $TiO_2$ nanotubes using templating metal salt fibers**

C. Aresipathi**,** *DFG Semi - annual meeting*, Hirschegg, Austria, 09/2005.

**Synthesis of oxide nanotubes encapsulated with platinum metal particles**

C. Aresipathi, L. Ren, M. Wark, *8th International conference on Nanostructured materials*, IISC Bangalore, India, 08/2006.

**Platinum doped oxide nanotubes**

C. Aresipathi, M Wark, Nanoday, 09/2006, Leibniz University of Hannover, Hannover, Germany.

**Novel oxide nanotubes containing heavy metal nanoparticles**

C. Aresipathi**,** *DFG Semi - annual meeting*, Fulda, Germany, 02/2006.

**Synthesis of oxide nanotubes encapsulated with heavy metal nanoparticles**

C. Aresipathi**,** M. Wark, *Technical University of Kiel*, Kiel, Germany, 12/2006.

**Embedded platinum metal particles in oxide nanotubes**

C Aresipathi, M. Wark, *DFG Semi - annual meeting* ,Fulda, Germany 05/2007.

**Magnus salt as new template for the formation of oxide nanotube**

C. Aresipathi, M. Wark, *DFG Semi - annual meeting*, Norderney, Germany, 08/2007.

### 7.2.3 Curriculum Vitae

***Personal Details***

| | |
|---|---|
| ***Name***: | Catherine Aresipathi |
| ***Date of Birth***: | 06th April, 1978 |
| ***Place of Birth***: | Vijayawada |
| ***Nationality***: | India |

***Education***

| | |
|---|---|
| 1996 – 2000 | Bachelor of Technology (B. Tech.) in Chemical Engineering,<br>Andhra University College of Engineering, Vishakhapatnam, India |
| 2001 – 2004 | Master of Science (M. Sc.) in Chemical Engineering,<br>University of Erlangen - Nurenburg, Erlangen, Germany |
| 2005 - 2008 | Doctor of Science (Ph.D) in Nanotechnology,<br>Institute of Physical Chemistry and Electrochemistry,<br>Gottfried Leibniz University of Hannover, Hannover, Germany |

***Work experience***

| | |
|---|---|
| 03/2000 | Worked as a trainee in *Visaka Steel Plant Ltd. (VSP)*,<br>Visakhapatnam, India |
| 05/2003 – 08/2003 | Worked as an Intern in *Framatome ANP*,<br>Erlangen, Germany |
| 06/2008 – till date | Working as a Chemical Process Engineer in *RENA, GmbH*,<br>Guetenbach, Germany |